Thèse de Coralie Escande, Lille 1, 2013

Université Lille1
Sciences et Technologies

Numéro d'ordre : 41345

Doctoral School **Sciences pour l'ingénieur n° 072**

Towards Modeling of a Class of Bionic Manipulator Robots

PH. D. THESIS

Presented and defended on 12th December, 2013

In order to become
Doctor from Université des Sciences et Technologies de Lille
(Speciality Robotics)

by

Coralie ESCANDE

Committee members

Reviewers	Kamal YOUCEF-TOUMI	Professor, Massachusetts Institute of Technology
	Véronique PERDEREAU	Professor, Université Pierre et Marie Curie
Examiners	Nicolas CHAILLET	Professor, Université Franche Comté
	Taha CHETTIBI	Professor, École Polytechnique Militaire d'Alger
	Christian DURIEZ	Researcher, INRIA Nord-Europe
Invited	Reinhard PITSCHELLIS	Doctor-Engineer, Festo Didactic GmbH & Co. KG
	Dirk PENSKY	Doctor-Engineer, Festo Didactic GmbH & Co. KG
Main Supervisor	Rochdi MERZOUKI	Professor, Université de Lille 1

Laboratoire d'Automatique, Génie Informatique et Signal – UMR 8219

© 2014 Tous droits réservés.

doc.univ-lille1.fr

© 2014 Tous droits réservés.

doc.univ-lille1.fr

Thèse de Coralie Escande, Lille 1, 2013

Université Lille1
Sciences et Technologies

Numéro d'ordre : 41345

École doctorale **Sciences pour l'ingénieur n° 072**

Vers la modélisation d'une classe de robots manipulateurs bioniques

THÈSE

présentée et soutenue publiquement le 12 décembre 2013

pour l'obtention du
doctorat de l'Université des Sciences et Technologies de Lille
(Spécialité Robotique)

par

Coralie ESCANDE

Composition du jury

Rapporteurs	Kamal YOUCEF-TOUMI	Professeur, Massachusetts Institute of Technology
	Véronique PERDEREAU	Professeur, Université Pierre et Marie Curie
Examinateurs	Nicolas CHAILLET	Professeur, Université Franche Comté
	Taha CHETTIBI	Professeur, École Polytechnique Militaire d'Alger
	Christian DURIEZ	Chargé de Recherche, INRIA Nord-Europe
Invités	Reinhard PITSCHELLIS	Docteur-Ingénieur, Festo Didactic GmbH & Co. KG
	Dirk PENSKY	Docteur-Ingénieur, Festo Didactic GmbH & Co. KG
Directeur de Thèse	Rochdi MERZOUKI	Professeur, Université de Lille 1

Laboratoire d'Automatique, Génie Informatique et Signal – UMR 8219

© 2014 Tous droits réservés.

doc.univ-lille1.fr

© 2014 Tous droits réservés.

doc.univ-lille1.fr

Thèse de Coralie Escande, Lille 1, 2013

Keywords: Bionic Robotics, Kinematic Modeling, Kinematic Calibration

Mots clés : Robotique Bionique, Modélisation Cinématique, Calibration Cinématique

© 2014 Tous droits réservés.

doc.univ-lille1.fr

© 2014 Tous droits réservés.

doc.univ-lille1.fr

Thèse de Coralie Escande, Lille 1, 2013

This thesis has been prepared at

Laboratoire d'Automatique, Génie Informatique et Signal
UMR CNRS 8219
Université Lille 1 - Cité Scientifique
Bât Polytech'Lille
59655 Villeneuve d'Ascq
France

☎ 00 33 (0)3 20 33 71 88
FAX 00 33 (0)3 20 33 71 89
✉ Marcelle.Desfromont@polytech-lille.fr
Web Site http://lagis.cnrs.fr/

© 2014 Tous droits réservés.

doc.univ-lille1.fr

© 2014 Tous droits réservés.

doc.univ-lille1.fr

Je dédie ce travail à mon copain et à ma famille, mais aussi à la mémoire de mon grand-père qui m'a fait promettre d'aller le plus loin possible dans mes études.

© 2014 Tous droits réservés.

doc.univ-lille1.fr

© 2014 Tous droits réservés.

doc.univ-lille1.fr

Il n'y a pas de faits, seulement des interprétations.

Friedrich Nietzsche

God has no religion.

Mahatma Gandhi

Mehr als die Vergangenheit interessiert mich die Zukunft, denn in ihr gedenke ich zu leben.

Albert Einstein

© 2014 Tous droits réservés.

doc.univ-lille1.fr

© 2014 Tous droits réservés.

doc.univ-lille1.fr

Thèse de Coralie Escande, Lille 1, 2013

Acknowledgements

Before beginning this dissertation, I want to first acknowledge and thank the many people that have made it possible through their support in many different ways.

First of all I wish to express my sincere gratitude to my Ph.D supervisor, Professor Rochdi Merzouki for giving me the opportunity to work with him on a very interesting topic. His advices and timely guidances, allowed me to complete this work.

Secondly, I would like to thank the company Festo Didactic GmbH & Co. KG, and particularly the industrial partners, Doctor-Engineer Dirk Pensky and Doctor-Engineer Reinhard Pitschellis, for financing this Ph.D. period and for providing the necessary material.

I also have to thank the director of the research laboratory LAGIS UMR CNRS 8219, Philippe Vanheeghe, for allowing me to finish my Ph.D..

Besides, I am also very grateful to the referee and committee members for taking time of their busy schedules and providing valuable comments.

I would also like to express my deepest gratitude to the Ph.D. Associate Professor Pushparaj Mani Pathak and the Professor Taha Chettibi for their priceless help.

I am also thankful to labmates and colleagues, including, but not limited to, Vincent, Nicolas, Nizar, Mohamed, Othman, Achille, Rui, Blaise, Aziz, Beate.

My greatest thank you is for my family, and my friends, for their love and encouragements.

Lastly, but most importantly, I am forever indebted to my lovely future husband: without his love, encouragement and support, this work could not have been achieved.

© 2014 Tous droits réservés.

doc.univ-lille1.fr

Thèse de Coralie Escande, Lille 1, 2013

© 2014 Tous droits réservés.

doc.univ-lille1.fr

Thèse de Coralie Escande, Lille 1, 2013

Towards Modeling of a Class of Bionic Manipulator Robots

Abstract

This work deals with a particular class of bionic manipulator robot namely Compact Bionic Handling Assistant (CBHA), which is mounted over a mobile omnidirectional robot namely *Robotino*. The whole robot (CBHA + *Robotino*) is named RobotinoXT. We first proposed a forward kinematic model of the CBHA by using an "arc geometry" method which was validated through a test bench using a trilateration technique. To achieve this purpose, the sensors were calibrated. For the model's constant parameters calibration problem, this latter was resolved by developing an optimization algorithm which incorporates a SQP method, validated via an industrial rigid manipulator. Then, we proposed an inverse kinematic model of the CBHA by assuming that each vertebra of it is assimilated to a parallel robot. This model was validated by real measurements obtained with the industrial manipulator, allowing defining the robot workspace. Finally, we implemented a toolbox which encompasses the models developed in this work.

Keywords: Bionic Robotics, Kinematic Modeling, Kinematic Calibration

Vers la modélisation d'une classe de robots manipulateurs bioniques

Résumé

Ce travail concerne une catégorie de robot manipulateur bionique, en l'occurrence le CBHA monté sur un robot mobile omnidirectionel, nommé *Robotino*. Le robot complet (CBHA + *Robotino*) est nommé RobotinoXT. D'abord, nous avons proposé un modèle cinématique direct du CBHA en utilisant une méthode nommée « arc geometry ». Celle-ci a été validée grâce à un banc d'expérimentation en ayant recours à une technique de trilatération. Pour atteindre cet objectif, les capteurs ont été calibrés. Concernant le problème de calibration des paramètres constants du modèle, il a été résolu en développant un algorithme d'optimisation incluant une méthode nommée SQP, validée via un manipulateur industriel rigide. Puis, nous avons proposé un modèle cinématique inverse du CBHA en supposant que chaque vertèbre de celui-ci est assimilée à un robot parallèle. Ce modèle a été validé par les mesures réelles obtenues avec le manipulateur industriel, permettant la définition de l'espace de travail du robot. Enfin, nous avons implémenté une boîte à outils qui englobe les modèles développés dans ce travail.

Mots clés : Robotique Bionique, Modélisation Cinématique, Calibration Cinématique

Laboratoire d'Automatique, Génie Informatique et Signal
UMR CNRS 8219 – Université Lille 1 - Cité Scientifique – Bât Polytech'Lille – 59655 Villeneuve d'Ascq – France

© 2014 Tous droits réservés.

doc.univ-lille1.fr

Thèse de Coralie Escande, Lille 1, 2013

© 2014 Tous droits réservés.

doc.univ-lille1.fr

Thèse de Coralie Escande, Lille 1, 2013

Acronyms

A | **B** | **C** | **D** | **E** | **F** | **G** | **H** | **I** | **K** | **L** | **M** | **N** | **P** | **Q** | **R** | **S** | **T** | **U** | **V** | **X**

A

AI Artificial Intelligence. 29

B

BG Bond Graph. 1

BHA Bionic Handling Assistant. 2, 9, 39, 40, 46, 82

C

CAD Computer-Aided Design. 47

CBHA Compact Bionic Handling Assistant. xvii, xxix–xxxi, cxliv, 3, 4, 6, 29, 32, 37, 39–43, 45, 47, 49, 50, 55, 58–62, 65–73, 75, 79, 81–83, 115–118, 120, 123, 124, 126, 128–130

D

DDoF Differential Degree of Freedom. 14, 16–19

D-H Denavit-Hartemberg. xxvii, 84, 86

DoF Degree of Freedom. 13, 14, 16–19, 30, 32, 35, 41, 68, 82

E

EAPs ElectroActive Polymers. 26, 27

© 2014 Tous droits réservés.

doc.univ-lille1.fr

Thèse de Coralie Escande, Lille 1, 2013

F

FKM Forward Kinematic Model. 81

FL Fuzzy Logic. 29

G

GA Genetic Algorithms. 29

H

HRI Human-Robot Interaction. 27

I

I/O Input/Output. 72, 73

ICR Instantaneous Center of Rotation. 14, 16, 17

IKM Inverse Kinematic Model. xxiv, 81, 82

K

KKT Karuch-Kuhn-Tucker. 71

KRL Kuka Robot Language. 72

KSS Kuka System Software. 72

L

LAGIS Laboratoire d'Automatique, Génie Informatique et Signal. vii, xvii, 1, 3, 116, 144

M

MOCIS Méthodes et Outils pour la Conception Intégrée de Systèmes. xxix, 1–3

MSBT Multi-Section Backbone Tube. 24

N

NN Neural Network. 29

© 2014 Tous droits réservés.

doc.univ-lille1.fr

Thèse de Coralie Escande, Lille 1, 2013

P

PAM Pneumatic Artificial Muscle. 24, 26, 27

Q

QP Quadratic Programming. 72

R

RSI Remote Sensor Interface. 72, 73

RTI Real-Time Interface. 73

S

SMA Shape Memory Alloys. 26, 27

SoS System of Systems. 1

SQP Sequential Quadratic Programming. 71, 72

T

TCP Transmission Control Protocol. 73

U

UGV Unmanned Ground Vehicles. 10

USTL Université des Sciences et Technologies de Lille. i, iii

V

VGT Variable Geometry Truss. 21

X

XML eXtensible Markup Language. 72, 73

© 2014 Tous droits réservés.

doc.univ-lille1.fr

Thèse de Coralie Escande, Lille 1, 2013

© 2014 Tous droits réservés.

doc.univ-lille1.fr

Thèse de Coralie Escande, Lille 1, 2013

Contents

Acknowledgements **xiii**

Abstract **xvii**

Acronyms **xvii**

Contents **xxi**

List of Tables **xxv**

List of Figures **xxvii**

General Introduction **1**
Framework and context of the thesis 1
Thesis objective 3
Problematic 3
Obtained results 4
Manuscript organization 5

1 State of the Art **7**
1.1 Bionics 7
1.2 Bionic Manipulator Robots Classification 11
1.3 Forward Kinematic Modeling of Bionic Manipulator Robots 19
1.3.1 Definition of Forward Kinematic Model 20
1.3.2 Modeling Assumptions 21
1.4 Description of the Different Forward Kinematic Modeling Methods . 22
1.4.1 Arc Geometry Method 22
1.4.2 Modified Denavit-Hartemberg Method 22
1.4.3 Curve parameterization Methods 23

© 2014 Tous droits réservés.

doc.univ-lille1.fr

Thèse de Coralie Escande, Lille 1, 2013

1.4.4 Integral representation 24
1.4.5 Exponential Coordinates 25
1.5 Inverse Kinematic Modeling of Bionic Manipulator Robots 25
1.5.1 Definition of Inverse Kinematic Modeling 25
1.5.2 Description of the Different Inverse Kinematic Modeling Methods 26
1.6 Conclusion of the Chapter 28

2 Forward Kinematic Modeling **29**
2.1 Robot Description 29
2.1.1 Compact Bionic Handling Assistant Description 29
2.1.2 Frames placements and Orientations 31
2.1.3 Parameters and Variables Definitions 33
2.2 Global Modeling Method 34
2.2.1 Problem Formulation 34
2.2.2 Assumptions 35
2.2.3 Modeling Method 35
2.3 Independent Kinematic Transformation 36
2.3.1 Homogeneous Transformations 36
2.3.2 Constant Transformation Matrices 36
2.3.3 Kinematic Transformations of Bending Sections 37
2.4 Specific Kinematic Transformation 39
2.4.1 Calculation of the Specific Kinematic Transformation 39
2.4.2 Singularities 42
2.5 Orientations 43
2.6 Experiment and Validation 45
2.6.1 Description of the Test Bench 45
2.6.2 Results and Discussion 51
2.7 Conclusion of the Chapter 56

3 Kinematic Calibration **57**
3.1 Calibration Technique 57
3.2 Calibration Problem Statement 59
3.3 Experiment and Results 62
3.3.1 Description of the Test Bench 62
3.3.2 Results 65
3.3.3 Discussion 65
3.4 Conclusion of the Chapter 69

© 2014 Tous droits réservés.

doc.univ-lille1.fr

Thèse de Coralie Escande, Lille 1, 2013

4 Inverse Kinematic Modeling **71**
4.1 Workspace . . . 72
4.1.1 Workspace Identification . . . 72
4.1.2 Obtained Results . . . 74
4.1.3 Discussion . . . 76
4.2 Global Modeling Method . . . 77
4.2.1 Modeling Assumption . . . 78
4.2.2 Determination of the Vertebra Radius . . . 78
4.3 Inter-vertebrae Inverse Kinematic Model . . . 79
4.3.1 Modeling of the Inter-vertebra Based on Raghavan and Roth Method . . . 80
4.3.2 Geometrical Model Based of the Inter-vertebra (Chasles Theorem) . . . 89
4.4 Generalized Kinematic Modeling . . . 93
4.4.1 Curve Generation . . . 95
4.4.2 Optimal Placement of the Frames . . . 96
4.5 Experimental Validation . . . 96
4.5.1 Obtained Results . . . 96
4.5.2 Discussion . . . 104
4.6 Conclusion of the Chapter . . . 105

5 Toolbox Implementation **107**
5.1 Main objectives . . . 109
5.2 Main Development . . . 109
5.3 Creating the Individual SIMULINK Blocks . . . 111
5.3.1 Placing the S-Function in S-Function Block . . . 111
5.3.2 Putting Blocks in Library and Making Accessible from the SIMULINK Library Browser . . . 117
5.4 Tests and Validation . . . 119
5.4.1 Geometric and Neural Network Forward Kinematic Models . 119
5.4.2 The "*Volttopressure*" Model . . . 119
5.5 Conclusion of the Chapter . . . 120

Conclusion **123**

Bibliography **125**

A Mobile Bionic Manipulator Robots **137**
A.1 Mobility of the Bionic Mobile Manipulator Robots . . . 139
A.1.1 Degree of Mobility . . . 139
A.1.2 Degree of Steerability . . . 141

© 2014 Tous droits réservés.

doc.univ-lille1.fr

Thèse de Coralie Escande, Lille 1, 2013

A.1.3 Degree of Maneuverability 142
A.1.4 Holonomy and Omnidirectionality 142
A.2 Conclusion of the Appendix 147

© 2014 Tous droits réservés.

doc.univ-lille1.fr

Thèse de Coralie Escande, Lille 1, 2013

List of Tables

1.1 Examples of spatial bionic manipulator robots 13
1.2 Examples of bionic mobile manipulator robots 14

2.1 Potentiometer Calibration Table 48
2.2 Constant parameters Values 51

3.1 Calibrated constant parameters 66

4.1 Extremal posture for a CBHA's section 73
4.2 Denavit-Hartemberg (D-H) parameters table 82
4.3 Extremal values of the lengths of each inter-vertebra in millimeter for the case of CBHA 96

A.1 Progress comparison 138
A.2 Comparison of several terrestrial mobile robots 144
A.3 Classification of the terrestrial mobile robots 146

© 2014 Tous droits réservés.

doc.univ-lille1.fr

Thèse de Coralie Escande, Lille 1, 2013

© 2014 Tous droits réservés.

doc.univ-lille1.fr

Thèse de Coralie Escande, Lille 1, 2013

List of Figures

1 Organization of the work developed within the group Méthodes et Outils pour la Conception Intégrée de Systèmes (MOCIS) 2

1.1 Architecture of bionic grasping system design 8
1.2 *Festo*'s Bionic systems 9
1.3 Hibot's robots (HiBot 2013) 10
1.4 Examples of commercialized mobile manipulator robots 11
1.5 Serpentine robots 12
1.6 Hybrid robots 15
1.7 Classification of the bionic manipulator robots 16
1.8 Surgery robots 16
1.9 OctArm robot (I. D. Walker 2013b) 18
1.10 Elastomeric Robots 18
1.11 Classification of the numerical methods 27

2.1 *Festo*'s Bionic manipulator robots 30
2.2 Actuators and sensors of the CBHA 30
2.3 Global View of the CBHA and the associated Frames 31
2.4 Orientation of Bishop Frames along a curve 32
2.5 Geometrical representation of the j^{th} bending section of the CBHA 33
2.6 Definition of the tubes and sections numbering 34
2.7 Global View of Modeling 36
2.8 The two constant transformations 37
2.9 Top view of the j^{th} bending section 39
2.10 Definition of the radius d_1 and d_2 40
2.11 View of the different curvature radius for one bending section ($\phi_j = 0$) 41
2.12 Overview of the trilateration test bench 46
2.13 Overview of the trilateration test bench architecture 47

© 2014 Tous droits réservés.

doc.univ-lille1.fr

Thèse de Coralie Escande, Lille 1, 2013

2.14 Side view of the possible configurations of the external potentiometers 51
2.15 Trajectory 1: only the first bending section is moving 52
2.16 Euclidian error of the trajectory 1 53
2.17 Trajectory 2: only the second bending section is moving 53
2.18 Euclidian error of the trajectory 2 54
2.19 Trajectory 3: both bending sections are moving 54
2.20 Euclidean error of trajectory 3 55

3.1 Zoom on the link between the industrial manipulator and the CBHA. 60
3.2 Overview of the industrial manipulator 63
3.3 Overview of the calibration experiment architecture 64
3.4 Overview of the position of the Frames 66
3.5 3D Trajectories of measured and estimated positions 67
3.6 Euclidean error of the trajectory executed with industrial manipulator 67
3.7 Euler angle of the trajectory executed with industrial manipulator . 68
3.8 Error on the Euler angle of the trajectory executed with industrial manipulator 68

4.1 Workspace identification process 72
4.2 Several points of view of the experimental workspace of CBHA . . 75
4.3 Several points of view of the simulated workspace of CBHA 76
4.4 Achitecture of backbone represented by a parallel robot 3UPS-1UP 77
4.5 Determination of the vertebrae radius 79
4.6 Frames placement of a kinematic chain UPS 81
4.7 Definition of the different transformations 85
4.8 Top view of the k^{th}. vertebra 86
4.9 Definition of attachment points 90
4.10 Inverse Kinematic Model (IKM) Steps Calculation 94
4.11 Placement of Bishop Frames on the CBHA's central curve 95
4.12 Architecture of the experimental validation 97
4.13 Simulated representation of posture of CBHA 98
4.14 Definition of lengths l_i 98
4.15 Trajectories of measured positions and of estimated positions from optimized IKM and CBHA Forward Kinematic Model (FKM) . . 99
4.16 Error in lengths l_1, l_4 and l_{1+4} 99
4.17 Error in lengths l_2, l_5 and l_{2+5} 100
4.18 Error in lengths l_3, l_6 and l_{3+6} 100
4.19 Linear error in estimated position (X^*, Y^*, Z^*) 101
4.20 Linear error in estimated position $(X_{cbha}, Y_{cbha}, Z_{cbha})$ 101
4.21 Euclidian optimized error (IKM) 102
4.22 Euclidian estimated error (CBHA) 102

© 2014 Tous droits réservés.

doc.univ-lille1.fr

Thèse de Coralie Escande, Lille 1, 2013

4.23 Several points of view of the simulated workspace with the assumption of uniform curvature . . . 103
4.24 Measured and estimated position associated with workspace assuming uniform curvature . . . 104

5.1 Imaged representation of the scope . . . 108
5.2 Major steps of the development of the CBHA modelling toolbox . . 110
5.3 Alternatives to creating custom SIMULINK blocks . . . 110
5.4 Inserting a Level-2 M-file S-Function block in a model . . . 112
5.5 Putting the S-function into the Level-2 M-file S-function block . . . 113
5.6 Appearance of the block after putting the S-function . . . 114
5.7 Dialogue box of mask editor . . . 115
5.8 Masking dialogue box . . . 115
5.9 Example of help for the CBHA forward kinematic model . . . 116
5.10 The opened help file . . . 116
5.11 RobotinoXT library . . . 117
5.12 RobotinoXT bionic trunk toolbox in the SIMULINK Library Browser 118
5.13 Setup of Forward Kinematic example . . . 120
5.14 Setup of Conversion example . . . 121

A.1 Mobile-manipulator platforms in robotics fields . . . 137

© 2014 Tous droits réservés.

doc.univ-lille1.fr

Thèse de Coralie Escande, Lille 1, 2013

© 2014 Tous droits réservés.

doc.univ-lille1.fr

Thèse de Coralie Escande, Lille 1, 2013

General Introduction

Framework and context of the thesis

This Ph.D. thesis was prepared within the research group "Méthodes et Outils pour la Conception Intégrée de Systèmes MOCIS"[1], of the "Laboratoire d'Automatique, Génie Informatique et Signal (LAGIS) (UMR CNRS 8219)"[2]. It is included in the framework of industrial research project (Festo 2013h), and funded by FESTO-DIDACTIC. The project consists in developing a kinematic model of the bionic arm, called CBHA belonging to an omni-drive mobile-manipulator robot called "RobotinoXT". This model is used to elaborate a strategy of autonomous control of the robot, based on the principles of intelligent autonomous vehicles, allowing handling and transporting adaptive loads for in-door applications. This work was developed under the supervision of Mr. R. Merzouki, Professor at Ecole Polytechnique Universitaire de Lille 1.

The research group MOCIS has an extensive experience with integrated design of systems, about modeling, structural analysis, control and diagnosis through the use of a unifying tool, called Bond Graph (BG). Figure 1 shows the topological organization of this group. This integrated design can focus on the microscopic system, example of an elementary robot as a physical system, or to the high level macroscopic system, including other robots, environment, communication between robot to robot or robot to environment. Such class of systems is conceptualized with architecture of System of Systems (SoS).

In this context, several research works have been published over the last 10 years. For example, in the field of modeling SoS (framework of this thesis) and cooperation control analysis, the work of the group is summarized as follows:

1. Organizational and Behavioral modeling of SoS (Khalil, Merzouki, et al. 2012);

2. SoS multi-levels supervision (Kumar et al. 2013);

[1] http://www.mocis-lagis.fr/
[2] lagis.ec-lille.fr

© 2014 Tous droits réservés.
doc.univ-lille1.fr

Thèse de Coralie Escande, Lille 1, 2013

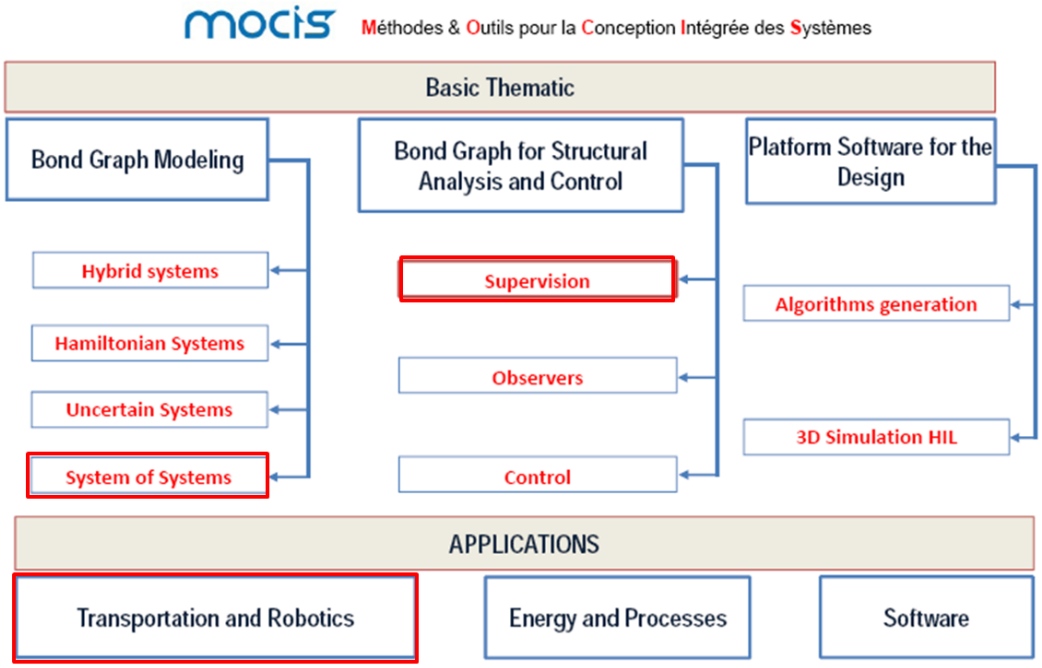

Figure 1: Organization of the work developed within the group MOCIS

3. Application to intelligent autonomous vehicles (Gelareh et al. 2013; Merzouki, Conrard, et al. 2013).

FESTO-DIDACTIC (Festo 2013h) is a leading provider in the field of industrial training and education. The company has brought together a comprehensive range of learning systems for basic and further training in industrial areas. One of its development challenges for the next years is the integration of mobile robotics in industrial and extra-industrial environment. Indeed the field of mobile robotic is a new way of learning because it creates a high fascination of young students to get involved in technology. Mobile robots provide a great platform to get involved in numerous learning objectives as mechanics, automation, mechatronics, image processing, and information technology. Moreover, it represents a great investment in the future due to the fact that mobile robotics will become one of the most important technologies of the 21st century. The well-known educational robot of this company is the omni-drive mobile robot "*Robotino*". To enhance their expertise in the field of pneumatic actuation, FESTO-DIDACTIC adopted the strategy of bionic sciences, by developing advanced technologies inspired from the nature. One of the resulting robots is the robot named Bionic Handling Assistant (BHA), representing a trunk of elephant. The small version of this robot has been assembled to the *Robotino* mobile platform, in order to build a version of

© 2014 Tous droits réservés.

doc.univ-lille1.fr

Thèse de Coralie Escande, Lille 1, 2013

mobile-bionic manipulator robot called "RobotinoXT". This robot is used only for research applications, where twelve laboratories all over the world develop different research topics in the field of modeling, control and navigation of the RobotinoXT. The main cooperation with FESTO-DIDACTIC and LAGIS was focused on modeling since 2010.

Thesis objective

The present work proposes a novel thematic within the MOCIS group. It concerns the integrated design of a class of bionic robots, interacting with hard or soft environments, according to the application. These robots can cooperate with biological environment (Medical exploration or treatment applications) or technological environment (Transport and handling applications).

Thus, the main goal of this Ph.D. work is related to the development of kinematic models (forward and inverse) of the Compact Bionic Handling Assistant (CBHA) with an appropriate kinematic calibration.

The modeling approaches can be generalized to other type of continuum and hyper-redundant robots. Even if in this work, the robot will not be designed, it is an industrial product which is not commercialized. The main objective of this modeling is to propose in the future, methods for the autonomous control of such class of hyper-redundant and continuum robots described in our case by the CBHA.

Problematic

Today, there are many mobile robot systems under development or in use. One very important goal is to use mobile robots at home or in industry. For many applications, a robot arm is necessary (e.g. supply elder people with food, drinks etc.). But today there are only two types of robot arms available[3]:

- Professional and rigid arms with high speed, high accuracy and high price;
- Toys with very limited performance.

Nowadays, what is missing in these classes of robot arms is an arm with medium performances concerning speed and accuracy, but with reasonable price, especially designed for mobile applications. In the education market there is a big demand for such kind of robot, but the market potential for home use applications is much

[3]Dr. Reinhard Pittschellis, "Lightwight Robot Arm for mobile robots based on rapid manufacturing and bionic principles", ECHORD project proposal, Festo Didactic GmbH & Co KG

© 2014 Tous droits réservés.

doc.univ-lille1.fr

Thèse de Coralie Escande, Lille 1, 2013

bigger. The design of lightweight robot arms is mainly focused on structures made of carbon fibers, and high end servo drives and industrial control systems with high energy density. This approach leads to an expensive design for professional use, which can't be sold in education and home use. The development of lightweight and cost-effective robot arm is an integrated design as follows:

- Mechanical structure made by rapid manufacturing;
- Low cost use of polymer harmonic drive gear boxes, DC-motors and potentiometer feedback;
- Bionic gripper use with ultra-flexible gripping jaws;
- Control system using a specific Human Machine Interface.

Flexible manipulator robots are increasingly used in scientific research this last decade (I. D. Walker 2013a), and in various applications: medical (Bai et al. 2012), military (BionicPower 2013), handling (Mori et al. 2010), ... Due to the flexible structure of these robots, it is suited to find a compromise of their obtained performances in terms of stability, accuracy and rapidity. To improve the closed loop control of these manipulators, it is important to develop accurate models, starting from the kinematic models and converging to the dynamic models. Kinematic modeling of bionic arms can be classified in two approaches: quantitative and qualitative, according to forward or inverse models. The forward model (Webster et al. 2010) can be obtained using several geometrical methods allowing the determination of the frame transformation matrices, describing the cartesian coordinates of the arm tip according to the joint positions. Generally, the forward kinematic model is used to impose a specific posture to the robot according to known joint positions. **Our contribution in this part is the development of a model calibration allowing the accuracy improvement.** Unfortunately, this model is not exploited for trajectory planning, where the inverse kinematic model is needed. In this case, qualitative methods for modeling are used, based on data-learning, to estimate the joint positions for imposed targets of the arm tip. Other quantitative methods exist in the case of hyper-redundant robots assimilated to the continuum robots. **In this case, our main contribution through this Ph.D. work was the development using non-linear optimization methods for the inverse kinematic model of the CBHA.** This is based on the whole optimization of the placement and the inter-distance of rigid parallel-serial platforms, along the central axis of the robot.

Obtained results

The obtained results have made the topic of the following publications:

© 2014 Tous droits réservés.

doc.univ-lille1.fr

Thèse de Coralie Escande, Lille 1, 2013

- **Journal**

  1. Coralie Escande, Taha Chettibi, Rochdi Merzouki, Vincent Coelen, Pushpraj Mani Pathak, "Kinematic Calibration of a Multi-section Bionic Manipulator", IEEE-Transaction on Mechatronics, Final review acceptance, 2013;

- **International Conference**

  1. Coralie Escande, Rochdi Merzouki, Vincent Coelen and Pushpraj Mani Pathak, "Geometric Modelling of Multisection Bionic Manipulator: Experimental validation on RobotinoXT", IEEE International Conference on Robotics and Biomimetics, Pages: 2006 - 2011 Guangzhou, China, (ROBIO 2012);
  2. Sonam Behl, Coralie Escande, Pushpraj Mani Pathak, Rochdi Merzouki, Bhanu Mishra, "Dynamic Modelling of Multi Section Bionic Manipulator: Application To Robotino-XT, The 6th International Conference on Integrated Modeling and Analysis", Applied Control and Automation, Part of I3M'2012, The 9th International Multidisciplinary Modeling & Simulation Multiconference, Wien, Austria , September 19-21, 2012, pp.247-252;
  3. Coralie Escande, Pushpraj Mani Pathak, Rochdi Merzouki, and Vincent Coelen, "Modelling of Multisection Bionic Manipulator: application to RobotinoXT", IEEE International Conference on Robotics and Biomimetics, Pages: 92 – 97, Phuket, Thailand, (ROBIO 2011).

Manuscript organization

The document is organized in 5 chapters as following:

- The first chapter concerns the state of the art developed to classify mobile-manipulator robots, and techniques for kinematic modeling of continuum and hyper-redundant robots. This chapter allows making the orientation of our work comparing to existing literature in modeling continuum and hyper-redundant robots.

- The second chapter presents the forward kinematic model of the CBHA. Based on arc geometry method, two types of experimental validation have been considered to validate the model accuracy.

© 2014 Tous droits réservés.

doc.univ-lille1.fr

Thèse de Coralie Escande, Lille 1, 2013

- The third chapter presents a kinematic calibration method for the proposed forward kinematic model of the CBHA. This method allows improving the model accuracy by identifying certain of the parameters and modeling uncertainties, using parametric optimization.
- The fourth chapter deals with the inverse forward kinematic model the CBHA. For this purpose, the CBHA's is assimilated structurally to a concatenation of rigid backbone platforms. The aim is to produce an optimal placement of the platforms along the central axis of the robot, allowing reproducing the best posture inside its workspace.
- The fifth chapter concerns the development of Matlab-Toolbox for forward kinematic model integration of the CBHA.
- Finally, the document is ended with a conclusion, summarizing the main contributions of this Ph.D. and discussing future derived works.

© 2014 Tous droits réservés.

doc.univ-lille1.fr

Thèse de Coralie Escande, Lille 1, 2013

Chapter 1

State of the Art

The bionic manipulator robots show a rapidly growing research field. Various research works have been carried out in this area in order to overcome the limitations of the existing modeling methods related to the classical robots. Basically, the new bionic robots reflect interests in developing autonomous robots inspired from humans and animals, namely elephant, snakes, fish and so on. This chapter is devoted to providing an overview about the different ways to design and to model such robots, by presenting the most advanced results in the subject, both theoretical and technological. Indeed, this literature review is quite important in order to make the difference with the standard manipulator robots and hence to highlight the main difficulties faced when dealing with bionic manipulator robots. To reach this objective, we first present a classification of the bionic manipulator robots. Then a comparison of strengths and weaknesses of the existing modeling methods is carried out.

1.1 Bionics

Bionics is a terminology associated with the transferability of biological solutions found in nature, towards engineering systems and modern technology. It is the abstraction of general principles in biological paragons (Mämpel et al. 2009), as shown in the example of Figure 1.1. In this case, we are interested in the red itinerary, starting from the biology level to the engineering level. Very interesting performances can be found in nature such as maneuverability, accuracy, speed, energy optimization, time response characteristics, adaptation and learning capacity. Historically, "Leonardo Da Vinci" was the first researcher in bionic field, where he tried to create a bio-inspired flying robot[4].

[4]as mentioned in the "Codex on the Flight of Birds" written in 1505

© 2014 Tous droits réservés.

doc.univ-lille1.fr

Thèse de Coralie Escande, Lille 1, 2013

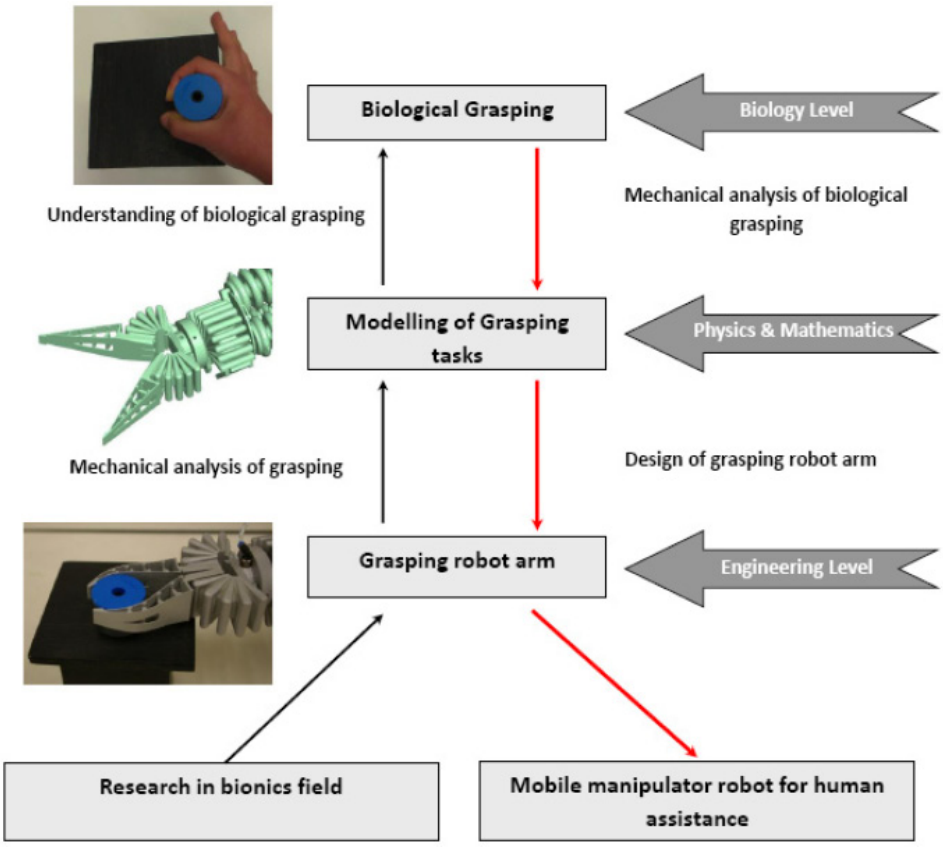

Figure 1.1: Architecture of bionic grasping system design

© 2014 Tous droits réservés.

doc.univ-lille1.fr

Thèse de Coralie Escande, Lille 1, 2013

Thanks to bionics, many mechatronic systems and devices in the robotics field have been considerably enhanced by exploiting various bio-inspired ideas (Pfeifer et al. 2012). So, the bionic research field covers many activities, and particularly the field of robotic research dealing with the development of bio-inspired morphologies, materials, sensors, actuators, structures, locomotion and control architectures (Guillot et al. 2008; Siciliano et al. 2009). The efforts of the researchers were led this last decades to the development of various non-classical robots, such as: humanoids, animal-like robots, toys robots, artistic robots, home robots, rescue robots, robots exploring unknown planets, robots specialized in hazardous tasks in hostile environment such as nuclear plants, robots for medical applications, exoskeletons etc. As a summary, the bionic robots can be classified in three categories: the aerial robots, the aquatic robots, and the terrestrial robots. The aerial class includes all the flying robots such as the drones (Krajník et al. 2011), or the animal-like robots (birds (Festo 2013f), insects (Festo 2013e), ...). The aquatic class includes the floating boats as well as the underwater robots (Roper et al. 2011), like the submarines or the animal-like robots (snake (Liljebäck et al. 2012), star-fish (Mao et al. 2013), fish (Gu et al. 2013), ...). In the literature, the terms "biomimetic robots" or "bio-inspired robots" are sometimes used in place of "bionic robots".

Concerning the industrial production around the bionic robots, many companies have started working in this area. Their main interest was the weight optimization of the robots with low costs, compared to conventional robots. These new products are often exploited for education or specific industrial use. Among these companies, *Festo* has realized many projects inspired by nature (Festo 2013a) such as Airics Arm, an anthropomorphic robot arm with fluidic muscles (Figure 1.2(a), 2007), Air Jelly and Aqua Jelly, which mimic the movement of the jellies, the Fingripper (Figure 1.2(b), 2009) and other robots (Festo 2013b), including the Bionic Handling Assistant (BHA) robot, imitating an elephant trunk.

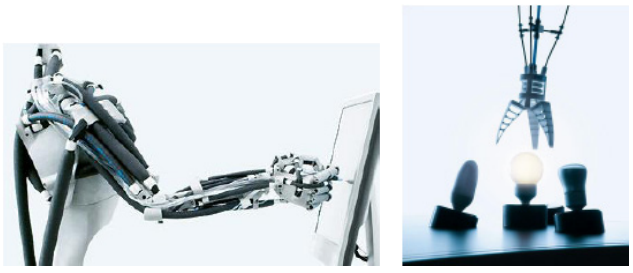

(a) (b)

Figure 1.2: *Festo*'s Bionic systems: (a) Airics Arm: antropomorphic arm with fluidic muscle, (b) Gripper with finray-gripping jaws

© 2014 Tous droits réservés.

doc.univ-lille1.fr

Thèse de Coralie Escande, Lille 1, 2013

In all those devices, the common idea is to imitate behaviors from nature, which can be reproduced by robotic systems. Many of these bionic projects were realized by using rapid manufacturing techniques. Bionic robots are also used in the medical domain such as: exoskeleton helps disabled patients find some mobility, and prosthesis replaces the loss of members. Among companies specializing in the design of exoskeleton robots, one can cite *Ekso Bionics* (EksoBionics 2013), a pioneer company specialized in exoskeletons since 2005. *Touch Bionics* (TouchBionics 2013) is a world-wide provider of hand and finger prostheses. *Otto Bock* (Ottobock 2013) is a German innovating company created in 1919, aiming to supply different sort of prosthesis to persons injured during the war. Their prostheses have evolved with scientific progress to obtain equipment for disabled sport competitions such as the *Paralympics*. In the military field, the exoskeletons are used to improve human capacity. *BionicPower* (BionicPower 2013) is a young company working on this field and its research are focused on smaller and lighter batteries which can recharge themselves, thanks to the mechanical movements of the human legs. However, bionic robots are more commonly assimilated to animal-like robots and mobile manipulator robots. The company *Hibot* (HiBot 2013) develops several types of robots including bionic robots such as mobile manipulator robots or snake-like robots shown in Figure 1.3.

(a) (b)

Figure 1.3: Hibot's robots (HiBot 2013): (a) ACM-R5, amphibious snake-like robot, (b) Helios 9, mobile manipulator robot

ASIMOV Robotics (ASIMOV 2013b) is an Indian company providing several types of robots with associated services as customized solutions for specific problems in various environments. Among these robots, one can find the mobile manipulator robot named "Landshark Arm" (shown in Figure 1.4(a)) (ASIMOV 2013a) which can be classified among the Unmanned Ground Vehicles (UGV). *OCRobotic* company (OCRobotics 2013) combines also the quality of mobile manipulator robot and bionic robot in one mobile bionic manipulator robot as shown in Figure 1.4(b). Such robot is useful in hazardous and confined spaces, e.g. a nuclear plant.

The next section describes bionic manipulator robots and their classification.

© 2014 Tous droits réservés.

doc.univ-lille1.fr

Thèse de Coralie Escande, Lille 1, 2013

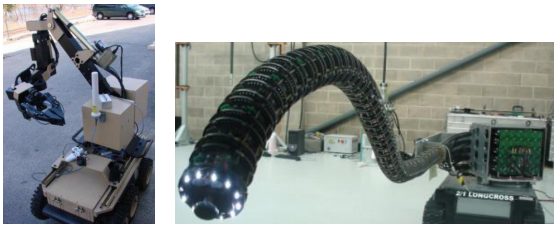

(a) (b)

Figure 1.4: Examples of commercialized mobile manipulator robots: (a) "Landshark Arm", mobile manipulator robot (ASIMOV 2013a), (b) Snake Arm deployed on Tracked Vehicle (OCRobotics 2013)

1.2 Bionic Manipulator Robots Classification

Manipulation is an important functionality in the robotics field as it characterizes the reachable workspace, accuracy and stability of the motion. According to these properties, the design of a manipulation system is considered. With advances in robotics in this last decade, improvements have been made in: structure, operation, rigidity, weight, control, power, etc. This has allowed seeing the technological transition from conventional manipulator robots to redundant, and to hyper-redundant robots. These robots, assimilated to continuous robots can also be designed with rigid or flexible structures.

Conventional robots [5] and Serpentine robots are defined as discrete robots and are described as a serial of rigid links (Robinson et al. 1999). Comparing to conventional robots, the main difference resides in the fact that these conventional robots have a finite number of rigid links, while the serpentine robots have short length rigid links and an important joint number. Serpentine robots are also named Variable Geometry Truss (VGT) structures, which describe a cascade structure of parallel and serial platforms (Chirikjian et al. 1994). It has been observed that serpentine robots with an important number of small backbones can be assimilated to continuum robots. Examples of serpentine robots are illustrated in Figure 1.5, where the first robot (Figure 1.5(a)) is a concatenation of rigid backbones linked by spherical joints and is cable-driven. The robot BROMMI of Figure 1.5(b) represents an example of continuum robots with an assembly of parallel-serial platforms.

In general, continuum robots are made using deformable material, allowing to realize a particular bended shape. Such class of robots (Hannan and I. D. Walker 2003) have a continuous shape with soft links, less actuated joints and more passive

[5] Conventional robots are commercialized robots used generally in industry, called also industrial robots

© 2014 Tous droits réservés.

doc.univ-lille1.fr

Thèse de Coralie Escande, Lille 1, 2013

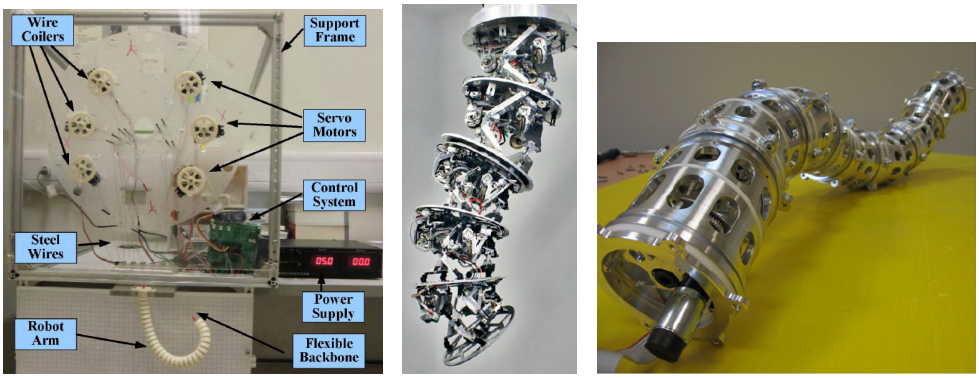

(a) (b) (c)

Figure 1.5: Serpentine robots: (a) Cable-driven serpentine robot (Z. Li et al. 2013), (b) BROMMI (Bionische Ruesselkinematik für sichere RoboterAnwendungen in der Mensch-Maschine-Interaktion) (Behrens et al. 2012), (c) Inclined Links Hyperredundant Elephant Trunk-like Robot (Salomon et al. 2012)

joints, e.g. OctArm (Jones and I. D. Walker 2006b), RobotinoXT (Festo 2013d), ...

Table 1.1 and Table 1.2 show examples of spatial bionic manipulator robots and bionic mobile manipulator robots.

Bionic manipulator robots are supposed to belong to the class of continuum robots, namely animal-like robots or zoomorphic robots, in order to reproduce particular bionic behaviors of: elephant trunk, snake, worm, octopus, ... Combining several bionic manipulator robots can lead to anthropomorphic robots such as hand robots, leg robots, shoulders robots, etc or simply humanoids.

Bionic manipulator robots have an advantage compared to rigid ones on their reachable workspace and their light weight structure. Unfortunately, their main disadvantage resides in their complicated control strategy elaboration for position and velocity, due to their hyper-redundancy and to their over-actuated joints.

They can be used to imitate the biological behavior of grasping tasks, e.g. elephant trunk. Often, this bio-inspired grasping is compliant to the targeted object, allowing to minimize the contact damages with the environment and correcting the inaccurate position of the gripper (Robinson et al. 1999). This property allows also grasping fragile objects with various shapes (Giri et al. 2010). An example is provided in (Sabetian et al. 2011), where a three-finger hand robot shows a great dexterity in grasping non-symmetrical objects. The compliance is suited for delicate grasping applications in medical area as fingers of hand prosthesis robot (Mattar 2013; Mori et al. 2010) or surgical catheter robots (Bailly et al. 2011; Kesner et al. 2011).

© 2014 Tous droits réservés.

doc.univ-lille1.fr

Thèse de Coralie Escande, Lille 1, 2013

Table 1.1: Examples of spatial bionic manipulator robots

Spatial Manipulator Robots		Shape	Struct.	Actuation	DoF/ Section	Num./ Section	Application
Elephant Trunk (Hanna et al. 2003)		continuous	hard	Hybrid: Cable-driven and pneumatic	2	4	Grasping
AirOctor robot (B. A. Jones at al. 2006b)		continuous	hard	Hybrid: Cable-driven and pneumatic	3	2	Research
Concentric Tube (Bai et al. 2012)		continuous	soft	SMA actuator	2	3	Surgery
Colobot robot (G. Chen et al. 2009)		continuous	soft	pneumatic	3	1	Surgery
Octopus (M. Sfakiotakis et al. 2013)		continuous	soft	SMA actuator	3	10	Underwater robot
BROMMI (Behrens et al. 2012)		discrete	hard	electrical	5	3	Research
Wire-Driven Serpentine (Z. li et al. 2013)		discrete	hard	electrical	4	16	Research

© 2014 Tous droits réservés.

doc.univ-lille1.fr

Thèse de Coralie Escande, Lille 1, 2013

Table 1.2: Examples of bionic mobile manipulator robots

Spatial Mobile-Manipulator Robots		Shape	Structure	Actuation	DoF/ Section	Number of Section	Application
OctArm robot (I. D. Walker 2013)		Continuous	Soft	Intrinsic (Pneumatic)	3	3	Grasping
CBHA, RobotinoXT (Festo 2013c)		Continuous	Soft	Pneumatic	3	2	Grasping
OCRobotic (OCRobotics 2013)		Discrete	Hard	Cable-Driven	2	>10	Exploration
Elephant Trunk-Like Robot (Salomon et al. 2012)		Discrete	Hard	Intrinsic (Electrical)	4	16	Research

The continuum robots are particularly adapted to constrained environments example of inspection in a pipe-line using worm-like or snake-like locomotion (Chirikjian et al. 1994). For space applications, cable-driven based continuum robots are used for exploration and inspection (I. D. Walker 2013a), where the category of string-like robot is defined as long and thin continuum robots. Underwater applications use also specific continuum robots like the Octopus robot (Sfakiotakis et al. 2013).

In the literature, various classifications of bionic continuum robots exist. In (Trivedi et al. 2008), two classes of continuum robots have been defined. The first class concerns the *soft robots* such as Pneumatic Artificial Muscle (PAM) robots, and the second class concerns the *hard robots with soft capabilities* such as Multi-Section Backbone Tube (MSBT) robots. *Soft robots* refer to invertebrate-like flexible-link manipulators, while *hard robots with soft capabilities* refer to vertebrate-like rigid-link manipulators. The main difference between these two categories of continuum robots is the type of actuation. *Soft robots* have an intrinsic actuation, that means that actuators represent a part of the backbones like pneumatic or hydraulic artificial muscles distributed over the robot's length. *Hard robots with soft capabilities* have either an extrinsic actuation or a hybrid actuation combining intrinsic and extrinsic actuations. Extrinsic actuators are separated from the backbone structure like in the cable-driven robots, where springs are installed between each backbone. Hybrid actuated robots are composed of one pneumatic or hydraulic central bellow controlling the extension, and of a tendon

© 2014 Tous droits réservés.

doc.univ-lille1.fr

Thèse de Coralie Escande, Lille 1, 2013

set controlling the orientation. Examples of hybrid robots are illustrated in Figure 1.6.

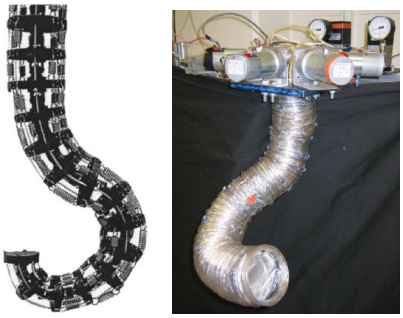

(a) (b)

Figure 1.6: Hybrid robots: (a) Elephant's trunk prototype (Hannan and I. D. Walker 2003), (b) AirOctor robot (Jones and I. D. Walker 2006b)

Figure 1.7 synthesizes this classification of the bionic manipulator robots according to the shape type, structure and actuation.

The design of continuum robots was compared with the biological performances of animals in order to improve:

1. Balance and Stability;
2. Exploration, Sensing and Manipulation;
3. Obstacle Avoidance and Grasping.

In (Cowan et al. 2012), the tail of kangaroos, geckos and monkeys are used to study the robot balance. Sensing quality can be observed on brittle stars and basket stars as well as on vine tendril or animal whiskers. Manipulation dexterity is illustrated in the octopus's arm. The main conclusion of this continuum robot design is that the combination of continuous and discrete elements is the key to accuracy, in terms of mechanics as well as in terms of control strategy elaboration.

Among existing hard robots with soft capabilities, one can cite the robots with rigid body and cable-tendons based actuation. For example, the company *OC-Robotic* developed mobile platforms with snake arm, used for exploration in nuclear plants (Anscombe, Buckingham, et al. 2006) or in aircraft industry (Anscombe, Bryant, et al. 2006).

In recent years, there has been an increasing interest in soft robotics (Iida et al. 2011; Kim et al. 2013) because their flexibility allows several possible morphologies, example of a class of soft robots can be reconfigured from a snake-like robot to a legged robot.

© 2014 Tous droits réservés.

doc.univ-lille1.fr

Thèse de Coralie Escande, Lille 1, 2013

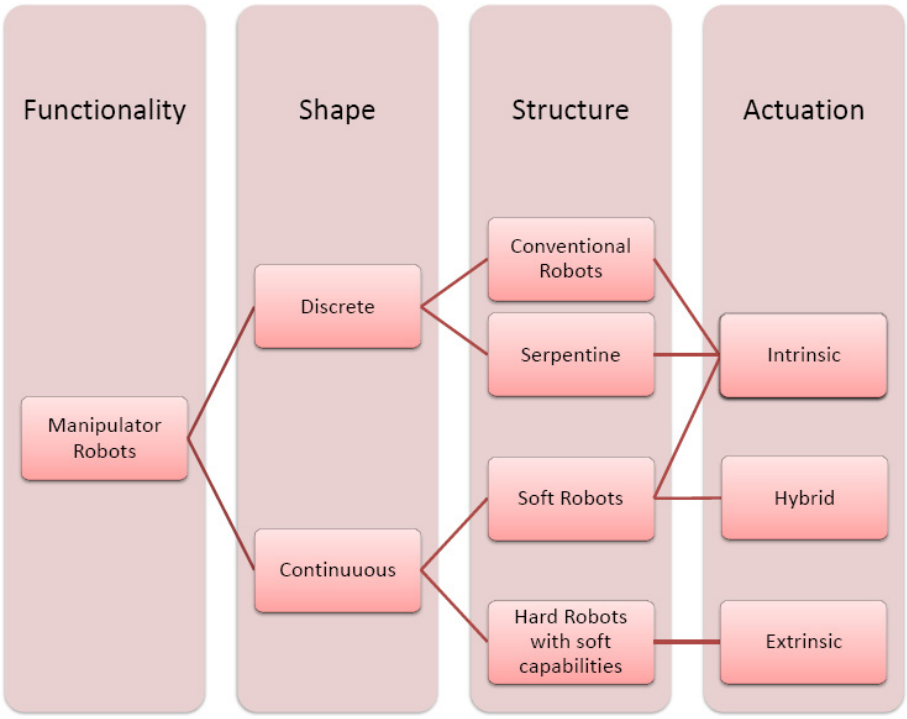

Figure 1.7: Classification of the bionic manipulator robots

Among existing *soft robots*, there are concentric tube based robots, the ElectroActive Polymers (EAPs) robots, the Shape Memory Alloys (SMA) actuators-based robots and the PAM robots.

The concentric tubes robots, also named active canulas robots, are used in medical applications because of their small diameter. The bending is generated by telescopic precurved elastic tubes having different stiffnesses. The class of concentric robots is often used in medical applications such as surgery, as illustrated in Figure 1.8.

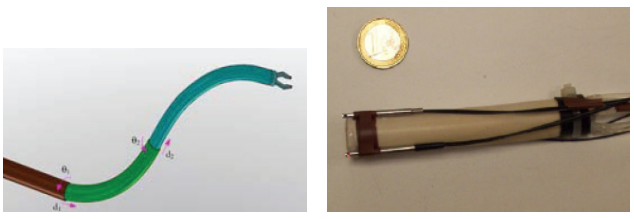

(a) (b)

Figure 1.8: Surgery robots: (a) Concentric tube (Bai et al. 2012), (b) ColoBot robot (Chen et al. 2009a)

© 2014 Tous droits réservés.

doc.univ-lille1.fr

Thèse de Coralie Escande, Lille 1, 2013

The EAPs robots are gel-like robots which are deformed when an electrical impulse is applied to the material. Such robot can be used in underwater or aerial environments. The flexibility of such robot is a great potential for designing robotic hands (Mattar 2013). In (Laschi et al. 2009), an octopus robot is proposed based on hydrostatic artificial muscles, having elongation and shortening capability.

The SMA actuator-based robots bend under the effect of temperature changes. Most of the SMA actuators are thus heated by electrical current in order to change the stiffness (C. Ma et al. 2012). The SMA actuators are often used for medical applications, such as active bending catheter and endoscope (Haga et al. 2010). In these applications, the external part of the robots are made by silicone rubber. The SMA actuators are also used for underwater applications, like the octopus-inspired robotic arm (Vavourakis et al. 2012).

Finally, the PAM robots are represented by the well-known *McKibben* robots. An example is used in (Takuma et al. 2008) for a multi-modal locomotion of a bipedal robot, where the compliance of flexible joints allows to tune the leg postures. Another example is given in (Mori et al. 2010), presenting a power hand robot, where the muscles are hydraulically actuated, allowing the hand robot to carry heavy payloads. Such *McKibben*-based muscles are also used by FESTO (Festo 2013g) as actuators of a 4-axis manipulator (Eichhorn et al. 2009). A very recent example is given in (Bartow et al. 2013), where the controlled muscles are contracting, unlike most of the muscle-based continuum robots whose muscles are extending.

This class of soft robots includes also soft links which are actuated pneumatically (Jones, McMahan, et al. 2004) or hydraulically, like the backbone tubes used in (Simaan 2005). Backbone tubes seem to be the most adapted for a medical miniature robot. An example of a soft robot is illustrated in Figure 1.9 representing the OctArm robot (I. D. Walker 2013b). In addition, recent research has been developed to create a new kind of PAM robots for manipulating soft and fragile objects, operating in confined and hazardous spaces, and performing complex motions. These new robots are pneumatically actuated, and are based on elastomeric materials, where some examples are given in Figure 1.10.

It is noticed that the continuum robot is designed with high accuracy performance similar to a rigid-link robot, instead its flexibility gives more maneuverability, particularly for obstacle avoidance. Indeed, the hyper-redundancy phenomenon, which is present, allows reaching the same target by using several postures. Moreover, if better accuracy is really necessary, example of surgery applications, several types of sensors (distance, or force) can be installed for an adaptive control. Another advantage of the continuum robot is the safe Human-Robot Interaction (HRI) based on its soft material design (Sanan et al. 2011).

Continuum robots are considered as a particular case of hyper-redundant robots

© 2014 Tous droits réservés.

doc.univ-lille1.fr

Thèse de Coralie Escande, Lille 1, 2013

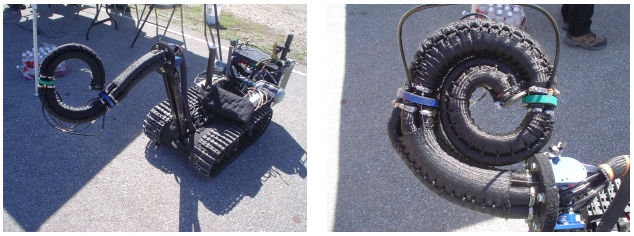

(a) (b)

Figure 1.9: OctArm robot (I. D. Walker 2013b): (a) mobile part of the OctArm robot, (b) trunk part of the OctArm robot

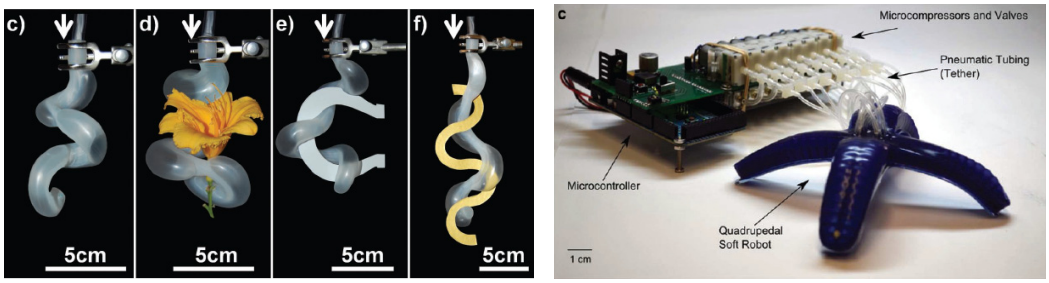

(a) (b)

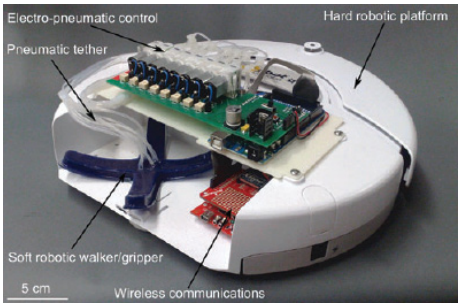

(c)

Figure 1.10: Elastomeric Robots: (a) Pneumatically actuated tentacles based on composite elastomeric structures (R. V. Martinez et al. 2013), (b) Starfish robot based on elastomeric flexible material (Stokes et al. 2013), (c) Combination of a mobile robot from the company Icreat and a starfish robot based on elastomeric flexible material (Stokes et al. 2013)

© 2014 Tous droits réservés.

doc.univ-lille1.fr

Thèse de Coralie Escande, Lille 1, 2013

because the joint space dimension tends toward infinity while link lengths tend toward zero. So, the continuum manipulator robots exhibit better maneuvrability and more possible motions in their workspace than the rigid-link manipulator robots, due to much larger degree of redundancy. For the extensible robots, the bending is combined with the extension of the continuum robot, to increase the workspace (I. D. Walker et al. 2006).

Therefore, continuum robots are hyper-redundant with often, under-actuated joints. These qualities provide to the robot the ability to reach a huge volume of the workspace, with an infinity of configurations. This workspace is also dependent on the extensibility of the robot's arm.

This general review of the continuum robots describes the performances in terms of design, maneuverability and reachability, illustrating a new perspective for the future manipulator robotics. The integrated design of a continuum robot imposes the necessity to integrate control strategies, allowing to track with high accuracy the trajectory of the arm's tip, like in the case of rigid manipulator robots. For this reason, developing kinematic models of such class of robots becomes a real challenge, according to the parameter and robot structure behavior uncertainties.

In the following section, we present a review study of kinematic modeling approaches for continuum robots, which are used for the statement of our contributions in modeling the CBHA.

1.3 Forward Kinematic Modeling of Bionic Manipulator Robots

The terminology of "kinematic modeling" is used to describe the robot pose[6] and its successive derivatives. Thus, "kinematic" encompasses both description of Cartesian coordinates, joint positions and velocities of the bionic arm. In (Khalil and Dombre 1999), the description of the Cartesian pose associated with the joints state is also called "geometric model", while the description of their velocities is also called "differential kinematic".

Kinematic modeling methods can be distinguished by two approaches: qualitative and quantitative. The qualitative approach consists in dividing the parameter space into several classes according to the known modes of operation and then determine by learning the mathematical relationship approximations, between the effects (observations of experts, sensor measurements and statistical data), and causes (inputs, trajectories, posture, ...). This approach is based mainly on Artificial Intelligence (AI) methods, such as, Neural Network (NN), Fuzzy Logic (FL), as well as Genetic Algorithms (GA), to optimize the choice of the effect-

[6]pose = position + orientation

© 2014 Tous droits réservés.

doc.univ-lille1.fr

Thèse de Coralie Escande, Lille 1, 2013

cause model' parameters. For quantitative approaches, also known as model-based methods, it consists of establishing a mathematical relationship between the causes and effects, based on fundamental kinematic relations. The quantitative methods depend mainly on the good knowledge of the kinematic parameters used to define the mathematical model.

For quantitative methods, a review of kinematic modeling methods of continuum robots for both single and multiple section manipulators is developed in (Webster et al. 2010). This review compares numerous methods of modeling based on constant curvature characteristic, namely: arc geometry, Denavit-Hartemberg parameters, Frenet-Serret Frames, integral representation, and exponential coordinates. It concludes from the given results that all these methods lead to the same closed-form solution[7], in the case where the local Frames are positioned in the same direction and the same assumptions are adopted. These methods of modeling differ from each other in notations and mathematical representations. Closed-form model allows for improving accuracy and dexterity. These two characteristics, are particularly important for surgical applications.

In this section, the most used quantitative methods in the literature for forward kinematic modeling of continuum robots are developed.

1.3.1 Definition of Forward Kinematic Model

The forward Kinematic model is a mathematical representation of the robot pose in terms of the joints positions. Mathematicaly, it is represented as follows (Rolf 2012):

$$f : \mathbf{Q} \rightarrow \mathbf{X}, f(q) = x \tag{1.1}$$

, where $q \in \mathbf{Q}$ is the action, $\mathbf{Q} \subseteq \mathbb{R}^m$ is the action space, $x \in \mathbf{X}$ is the outcome, and $\mathbf{X} \subseteq \mathbb{R}^n$ is the observation space. The dimensions m and n correspond respectively to the number of Degree of Freedom (DoF), and to the dimension of the task space. The function f is defined as a continuous and surjective function, described as follows:

$$\forall x \in \mathbf{X}, \exists q \in \mathbf{Q}, x = f(q) \tag{1.2}$$

The standard representation of a forward kinematic model is a homogeneous matrix $\mathbf{M}$ given by equation (1.3), where $\mathbf{R}$ is the rotation matrix, r_{ij} is an element of the matrix $\mathbf{R}$ located at the intersection of the i_{th} row and the j_{th} column, and $\mathbf{P}$ is the position vector. The elements of the rotation matrix are named direction

[7]Closed-form solution = Deterministic equation including a finite number of known functions and parameters

© 2014 Tous droits réservés.

doc.univ-lille1.fr

Thèse de Coralie Escande, Lille 1, 2013

cosines and are used to calculate the orientation.

$$\mathbf{M} = \left[\begin{array}{c|c} \mathbf{R} & \mathbf{P} \\ \hline 0 & 1 \end{array}\right] = \left[\begin{array}{ccc|c} r_{11} & r_{12} & r_{13} & x \\ r_{21} & r_{22} & r_{23} & y \\ r_{31} & r_{32} & r_{33} & z \\ \hline 0 & 0 & 0 & 1 \end{array}\right] \tag{1.3}$$

1.3.2 Modeling Assumptions

Kinematics of bending sections of continuum manipulator robots are widely developed under the constant curvature assumption (Webster et al. 2010), i.e. the shape of a bending section is assumed to be a perfect arc of circle. Indeed, on the basis of this assumption, successful results are reported in many references such as (Chen et al. 2009b; Iqbal et al. 2009; Webster et al. 2010). This approximation has the advantage to simplify the model of some continuum robots and allows to use Frame matrix transformations. In (Webster et al. 2010), several arguments are presented to explain the use of the constant curvature assumption according to the structure of the robot. The main arguments are:

- When gravity and loading charges are neglected, the continuum robot is assimilated to a mechanical beam since the input pressure inside the tubes distributes equally the forces along the trunk;
- When the continuum robot is bending, the global shape looks like a concatenation of an arc of circle;
- Previous research on continuum robots using this assumption has given accurate results under this assumption.

However, in some cases, gravity and external loading generate deformation in the curve shape of the continuum robots, making the constant curvature a hard assumption. It is the case of robots used in medical application such as surgery, where concentric tube-based robots or cable-driven robots are used. To solve this problem, two modeling methods can be used: curve parametrization or exponential coordinates. These methods allow modeling the curve with a varying bending shape. It can also be resolved using differential kinematic modeling, with the mechanics of rods, also named beam theory. For that, the classic equilibrium equations of a cosserat rods are considered (Rucker 2011). Finally, it is also possible to use, in some cases, an adaptive controller to compensate for the non-linear deflection of the bending section

A recent work proposed a modeling method with variable curvature assumption to describe the manipulator's deflection (Mahl, Mayer, et al. 2013). It consists in

© 2014 Tous droits réservés.

doc.univ-lille1.fr

Thèse de Coralie Escande, Lille 1, 2013

subdividing each sections of the continuum manipulator in a finite number of virtual units, having a constant curvature.

1.4 Description of the Different Forward Kinematic Modeling Methods

1.4.1 Arc Geometry Method

For continuum robots, the most widely used modeling method is the arc geometry under the assumption of constant curvature. This is presented as a general method by (Webster et al. 2010) and it is used to model several continuum robots (Jones and I. D. Walker 2006a,c; Neppalli et al. 2009). This method is based on a mathematical formulation of an arc of circle.

The arc geometry method was tested by (Hannan and I. Walker 2001), where a real-time implementation of the kinematic control is realized. (Jones and I. D. Walker 2007) studied the singularity issues for a particular trunk robot arm in a straight posture. The length limits constraints and the reachable workspace are also studied. The proposed kinematic model is applied to concentric tube-based robot (Rucker et al. 2010), also called "active cannulas", actuated by the rotation and the translation of three telescoping tubes. The modeling method is used to model a micro-robot placed at the tip of a catheter (Iqbal et al. 2009).

The main advantage of the arc geometry modeling method is its easy determination and implementation, when all the geometric parameters involved in the establishment of the model are well-known. The disadvantage comes from the assumption of perfect curvature of the bending section, which is not the case for all continuum robots, and adds uncertainty and inaccuracy for the model validation.

1.4.2 Modified Denavit-Hartemberg Method

Kinematic modeling of bionic continuum robots is developed using modified Denavit-Hartemberg convention (Hartenberg et al. 1955), and integrating the constant curvature assumption (Hannan and I. Walker 2001). The validation of the model has been done with a robot called "*elephant trunk*" robot and designed with segmented backbones. The main difference with the classical Denavit-Hartemberg methods lies in the fact that the transformation matrix is written in terms of configuration space variables and not in terms of joint space variables. This method needs an accurate Frame placement to deduce the kinematic parameters. Depending on a high number of DoF in continuum robots, the calculation of transformation matrices and their product supposes the use of modern tools for numerical analysis

© 2014 Tous droits réservés.

doc.univ-lille1.fr

Thèse de Coralie Escande, Lille 1, 2013

and appropriate hardware for real-time implementation. The limit of this method lies in the fact that the frames have to be placed with a particular convention.

This method has been developed for a multi-section continuum robot in terms of pose and velocities, where the results are validated in a real-time simulation combining several simulation tools (Jones and I. D. Walker 2005).

1.4.3 Curve parameterization Methods

Two curve parametrization methods are reported:

1. The Frenet-Serret Frames method;
2. The Parallel Transport Frames (or Bishop's Frame) method.

The main inconvenient of the curve parameterization methods is that it is not compatible with real-time implementation due to the fact that a numerical computation need to integrate a differential equations system in order to solve this equations system.

1.4.3.1 Frenet-Serret Frames method

Frenet-Serret method is probably the most well-known method of curve parametrization. This method is based on local Frenet-Serret Frame which introduces the principle of differential parametric equations. It describes how a local coordinate Frame is placed along the curve in euclidian space ($\mathbb{R}^3$), depending on two parameters: the curvature $\kappa(L)$ and the torsion $\tau(L)$ (or twisting), which are dependent on the curve length L. Standard form of the equations is given in (1.4), where $\mathbf{T}$ is the tangent vector of the curve, $\mathbf{N}$ is the normal vector of the curve and $\mathbf{B}$ is the binormal vector to obtain a unit direct Frame[8]. The variables $\mathbf{T}'(L)$, $\mathbf{N}'(L)$, and $\mathbf{B}'(L)$ are respectively the vectors derivative, according to the arc length L. In the case of constant curvature assumption, the variable $\kappa(L)$ is taken as a constant.

$$\begin{pmatrix} \mathbf{T}'(L) \\ \mathbf{N}'(L) \\ \mathbf{B}'(L) \end{pmatrix} = \begin{pmatrix} 0 & \kappa(L) & 0 \\ -\kappa(L) & 0 & \tau(L) \\ 0 & -\tau(L) & 0 \end{pmatrix} \begin{pmatrix} \mathbf{T}(L) \\ \mathbf{N}(L) \\ \mathbf{B}(L) \end{pmatrix} \tag{1.4}$$

For many continuum robots design excluding the cable-driven robots, the variable $\tau(L)$ is considered constant, or neglected. In this case, the curve is bending in the plane containing normal and tangent vectors. Frenet-Serret method has been used to model a planar continuum robot in (Hannan and I. D. Walker 2003), representing a 2-cable actuated robot. A three-dimensional model has been developed

[8] right-handed orthonormal basis

© 2014 Tous droits réservés.

doc.univ-lille1.fr

Thèse de Coralie Escande, Lille 1, 2013

in (Webster et al. 2010), using appropriate numerous calculation for differentiation, substitution and integration in order to solve the differential equations of the system. However, this method can be applied only on non-degenerate curves, that means there is a singularity which appears when the curve is straightforward (i.e. $\kappa(L) = 0$).

This method has been used in (C. Li et al. 2002) for a cable-driven robot in order to take into account the effect of the stiffness of the bending shape.

This method is particularly adapted to the continuum robots having extension and torsion capacity, such as the concentric-tubes robots, e.g. the active catheters used in surgery.

1.4.3.2 Parallel Transport Frames method

The Parallel Transport Frames method is also called Bishop's Frame method, and seems to be particularly adapted to continuum robots (Bishop 1975; Karacan et al. 2010) because of the non-torsion property. The Bishop's Frame equation is given in (1.5), where $\mathbf{N_1}(L)$ and $\mathbf{N_2}(L)$ are the normal and binormal vectors under the constraint of parallel transport along the curve. The variable $\kappa_1(L)$ and $\kappa_2(L)$ are functions of the polar coordinates $\kappa(L)$ and $\tau(L)$.

$$\begin{pmatrix} \mathbf{T}'(L) \\ \mathbf{N_1}'(L) \\ \mathbf{N_2}'(L) \end{pmatrix} = \begin{pmatrix} 0 & \kappa_1(L) & \kappa_2(L) \\ -\kappa_1(L) & 0 & 0 \\ -\kappa_2(L) & 0 & 0 \end{pmatrix} \begin{pmatrix} \mathbf{T}(L) \\ \mathbf{N_1}(L) \\ \mathbf{N_2}(L) \end{pmatrix} \tag{1.5}$$

Other elegant description for tubes and ribbons curves are detailed in (Hanson 1998) using quaternion Frenet-Serret Frames. This method is useful for computer-based graphics design.

1.4.4 Integral representation

The curves parametrization belongs to the class of differential geometry. However it is also possible to use integral geometry. Indeed, the method of integral representation is an alternative of Frenet-Serret Frames methods and uses the spherical coordinates (Chirikjian et al. 1994). The advantages of this method are:

- Absence of singularity case when the curve is straight;
- Unlike the differential representation methods such as Frenet-Serret Frame or Bishop Frame methods, numerical solution computation of a differential equations system is not required;
- This representation takes into account the tightening and the extension of the curve.

© 2014 Tous droits réservés.

doc.univ-lille1.fr

Thèse de Coralie Escande, Lille 1, 2013

This last advantage is however not useful for the non-extensible robots.

It is noticed, that continuum manipulator robots can be described as several concatenated curves associated to each section. So a multi-section continuum manipulator robot needs as many sets of multi-curve parametrization as number of sections.

1.4.5 Exponential Coordinates

This method is based on the Lie Group Theory and consists in calculating the exponential of the matrix to represent transformations. For multisection cases, the exponentials of the matrices are multiplied like the case of homogeneous transformation.

This method has been developed in (Zhao et al. 2010) in terms of pose and velocities, where the model validation has been done using numerical simulation of one section bionic arm, taking the dimensions of a real cable-driven continuum robot. It is demonstrated that all other types of modeling methods yields the same model.

1.5 Inverse Kinematic Modeling of Bionic Manipulator Robots

1.5.1 Definition of Inverse Kinematic Modeling

Based on the mathematical definition of the forward kinematic model previously given in equation (1.1), the inverse kinematic modeling formalism is given by equation (1.6) and it is defined as follows: how to find the action q which is necessary to reach the outcome x ?

$$f : \mathbf{X} \rightarrow \mathbf{Q}, q = f^{-1}(x) \tag{1.6}$$

When $n = m$, there exists a finite number of solutions to the inverse kinematic model. When $n < m$, there exists an infinite number of solutions to the inverse kinematic model because it corresponds to the case of redundant robots. In (Rolf 2012), the redundancy is mathematically defined as in equation (1.7). When m value is very large, the system is considered as hyper-redundant.

$$\exists q_1 \neq q_2 \in \mathbf{Q}, f(q_1) \neq f(q_2) \tag{1.7}$$

© 2014 Tous droits réservés.

doc.univ-lille1.fr

Thèse de Coralie Escande, Lille 1, 2013

1.5.2 Description of the Different Inverse Kinematic Modeling Methods

The classic analytical resolution method consists in differentiating the forward kinematic model to obtain the Jacobian matrix, and then to calculate the inverse matrix of this Jacobian matrix.

If a solution exists, the algebraic and geometric methods are used to find a closed-form inverse kinematic model (Lee et al. 1984). Otherwise the numerical methods can be used because they are independent from the robot type. For redundant robots, the main resolution methods are based on the Jacobian pseudo-inverse, the extended Jacobian inverse and the augmented Jacobian inverse. Unfortunately, these methods are not suitable for most hyper-redundant robots because their very high number of DoF involves a very large number of equations and infinite number of solutions. This hyper-redundancy implies that multiple solutions co-exist (finite or infinite number of solutions). In this case, numerical methods are the most used because they are not dependent on the robot's degree of redundancy. The limitation of numerical methods is that more computing power is needed and that for most of them, the given result is only one possible solution. The numerical methods can be classified in two classes (Durand et al. 2000) : the symbolic elimination methods and the iterative methods, where Figure 1.11 gives the most used methods.

Inverse kinematic model of hyperredundant robot can be found thanks to modal shape function method (Chirikjian et al. 1994). The interval analysis methods are said to be the most promising because they converge quickly and all possible solutions can be found. The damped least squares approaches are used for the complex mechanisms.

An inverse kinematic model based on one bending section with spacial configuration has been proposed in (Jones and I. D. Walker 2006a). For the validation, the model calculation has been done using a specific symbolic software to describe the kinematic behavior of the two-section Air-Octor and the OctArm manipulators. The workspace and the configuration space has been studied by describing the relative constraints to the lengths limits of the robots (Jones and I. D. Walker 2006b). The knowledge of the robots allows keeping the bio-inspired robot in safe postures and facilitates the selection of lengths and curvature directions. To improve the control of continuum robots, a multi-interval analysis (I. D. Walker et al. 2006) can be used, taking into account not only the bending aspect but also the extension of the robot.

Other deduction of kinematic model of continuum robots is proposed in (Neppalli et al. 2009), where it is considered as a multisection case, and the extreme points of each section are expected to be known. These positions can be chosen by resolving a system of inequalities. For this case, the model has been validated by

© 2014 Tous droits réservés.

doc.univ-lille1.fr

Thèse de Coralie Escande, Lille 1, 2013

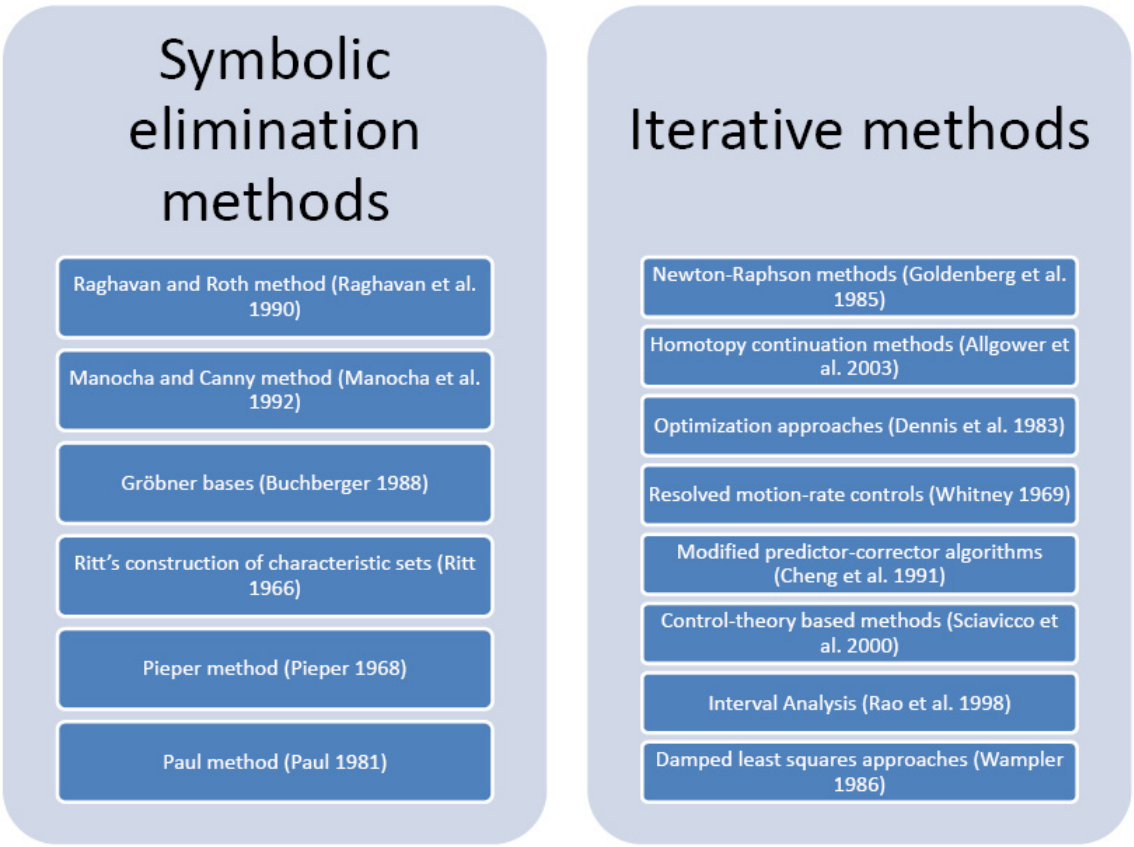

Figure 1.11: Classification of the numerical methods

© 2014 Tous droits réservés.

doc.univ-lille1.fr

Thèse de Coralie Escande, Lille 1, 2013

simulating the overall behavior using appropriate software. Other enhancements have been done in (Iqbal et al. 2009) by presenting a complete inverse kinematic model based on (Jones and I. D. Walker 2006a) for one bending section not only with spatial configuration but with workspace configuration. The validation of this model is done on a micro-robot in the form of active catheter used in surgery operation and has shown that the model is not robust against uncertainties of environment and inaccuracies of materials. The model has been calculated using the interval analysis principle as an optimization issue with a cost function and constraints.

1.6 Conclusion of the Chapter

This chapter reviewed the literature on the mobile bionic manipulator robots classifying the mobile robots in terms of their mobility, steerability, maneuverability and holonomy; and classifying the bionic manipulators according to their hyper-redundancy, shape, structure, and actuation. This chapter compared the different modeling methods of continuum robots by classifying them in two approaches: qualitative and quantitative.

It is the basic work of our investigation to model the 2-section bionic manipulator CBHA, which is classified as a continuously bending robot, having a non-extensible soft structure and an intrinsic actuation (pneumatic). Due to these characteristics, the CBHA is considered as hyper-redundant and under-actuated manipulator robot.

This review enabled us to position our work according to the research stream on kinematic modeling of continuum and hyper-redundant robot. Thus, our developed models are model-based methods, defined as a quantitative approach.

In this PhD thesis, we employ an arc geometry based-method to establish the forward kinematic model of the CBHA. This method has been chosen for several reasons: it is mathematically easy to develop for continuum robots without extension and torsion capacity, and the computation allows a real-time implementation.

The forward kinematic modeling is inspired from the existing methods of arc-geometry described in this chapter, where the innovation is located at the kinematic calibration method proposed to improve the model accuracy.

Concerning the inverse kinematic model development, we exploited the principle of the hyper-redundancy to assimilate the flexible bionic arm of the CBHA to a concatenation of multiple rigid backbone (vertebra) platforms with flexible inter-vertebrae. The inverse kinematic model of each vertebra is well-known, and then an optimal placement of these platforms is proposed to obtain the best posture of the bionic arm.

© 2014 Tous droits réservés.

doc.univ-lille1.fr

Thèse de Coralie Escande, Lille 1, 2013

Chapter 2

Forward Kinematic Modeling

This chapter describes the FKM of the CBHA. After a general description on the CBHA, the placement of the different Frames is outlined, the assumptions are presented and the parameters and variables are defined. Then, the forward kinematic modeling problem is formulated and the modeling method is explained. In addition, the FKM of the CBHA is developed in 3 different sections: Independent Kinematic Transformation, Specific Kinematic Transformation, and Orientations. Finally, an appropriate experimental test bench using trilateration technique is described and the model validation is discussed based on the experimental results.

2.1 Robot Description

In this section, the Compact Bionic Handling Assistant (CBHA) is illustrated and its actuators and sensors are enumerated. The different Frames placement is described, then the parameters and variables are defined.

2.1.1 Compact Bionic Handling Assistant Description

Compact Bionic Handling Assistant (CBHA) is the manipulator part of the mobile robot RobotinoXT, shown in Figure 2.1(a). The CBHA is a smaller version of the BHA, shown in Figure 2.1(b). Both bionic manipulators are bio-inspired from a trunk of elephant.

The mobile platform of this robot can be classified in the class of omnidirectional and holonomic robots, thanks to its three omnidirectional wheels. These wheels are independently actuated using three DC-motors with gear transmission system. The mobile platform is equipped with different types of sensors: collision rubber detector, distance sensors, optical detectors, inductive sensors, encoders and gyroscope.

© 2014 Tous droits réservés.

doc.univ-lille1.fr

Thèse de Coralie Escande, Lille 1, 2013

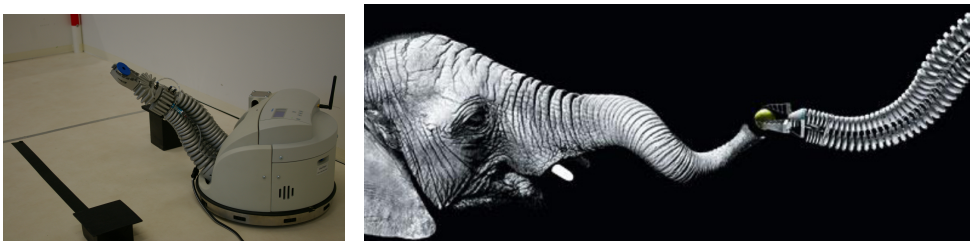

(a) (b)

Figure 2.1: *Festo*'s Bionic manipulator robots: (a) RobotinoXT (= Robotino + CBHA), (b) BHA (Festo 2013c)

The manipulator CBHA, shown in Figure 2.2, is a bionic manipulator arm inspired from an elephant trunk. It is a continuum robot, and can be classified as a soft robot with intrinsic actuation. The flexibility of the CBHA is provided first by the *Polyamide* material manufactured through rapid prototyping process, and secondly from the high number of interconnected bionic backbones, which provide it an important maneuverability. Thanks to its flexible material, the CBHA is lightweight (1060 g) and can carry out a maximal payload of 600 g.

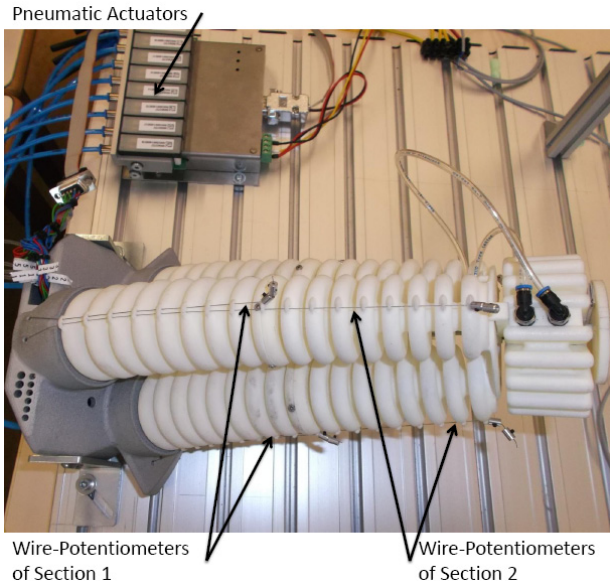

Figure 2.2: Actuators and sensors of the CBHA

From a macrocopic level, the CBHA is composed of: two bending sections, one rotation part, and one compliant gripper. Each bending section is composed of three continuous flexible backbone tubes. From a microscopic level, each tube

© 2014 Tous droits réservés.

doc.univ-lille1.fr

Thèse de Coralie Escande, Lille 1, 2013

is composed of bionic backbones. The bionic manipulator is actuated using nine electro-pneumatic valves[9]: three per bending section[10], two for the rotation part and one for the gripper. Seven sensors are used to estimate the trunk posture: six wire-potentiometers measure the instantaneous lengths l_i of each tubes, giving proportional voltages of the cable length, and one orientation-potentiometer, which measures the posture of the rotative part. The position and the orientation of each section is controlled by varying the input air pressure from the electropneumatic valves.

An inextensible central rod limits the maximal length extension of the CBHA, without affecting the variation of the length of each section[11]. This aspect constrains the workspace achieved by the robot.

The CBHA is characterized by its hyper-redundancy with a high number of DoF and by its underactuation.

2.1.2 Frames placements and Orientations

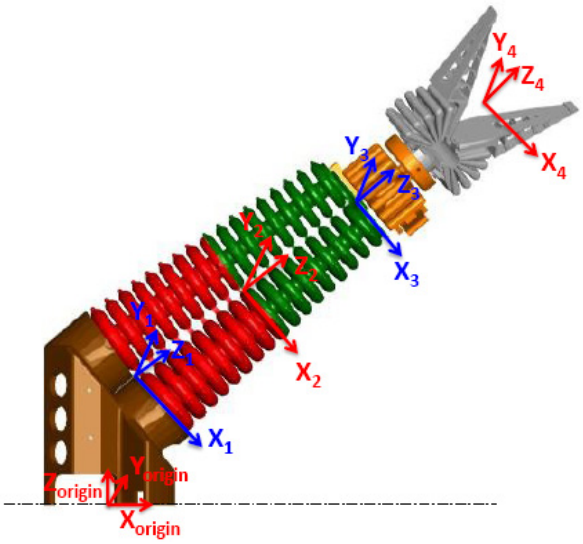

Figure 2.3: Global View of the CBHA and the associated Frames

First, let us introduce the Frames used to describe the kinematics of the CBHA, as shown in Figure 2.3.

[9] proportional and piezoelectric

[10] one for each tube

[11] The first section can be extended while the second section is compressed maintaining the total length of the trunk constant, which is about 330 mm by including the rotation part and gripper size.

© 2014 Tous droits réservés.

doc.univ-lille1.fr

Thèse de Coralie Escande, Lille 1, 2013

1. The first Frame $\{\mathbf{x}_{\text{origin}}, \mathbf{y}_{\text{origin}}, \mathbf{z}_{\text{origin}}\}$ is attached to the mobile platform at the basis of the CBHA;
2. The second Frame $\{\mathbf{x}_1, \mathbf{y}_1, \mathbf{z}_1\}$ is attached to the basis of the first bending section;
3. The third Frame $\{\mathbf{x}_2, \mathbf{y}_2, \mathbf{z}_2\}$ is attached to the basis of the second bending section;
4. The fourth Frame $\{\mathbf{x}_3, \mathbf{y}_3, \mathbf{z}_3\}$ is attached to the basis of the rotative part;
5. The fifth Frame $\{\mathbf{x}_4, \mathbf{y}_4, \mathbf{z}_4\}$ is attached to the center of the end-effector.

The Frames are oriented along the center curve of the CBHA as Bishop Frames (see Figure 2.4), also named Parallel Transport Frames (Bishop 1975), which is an alternative to the Frenet-Serret Frames, where the torsion is constant. The Bishop Frames are oriented as a parallel vector field, where normal and binormal vectors are parallel transported along the curve, according to the tangent vector. In this configuration, given the first right-handed orthonormal Frame, all other Frames can be defined along the curve. Indeed, by definition, the z-axis is always tangential to the curve. The x- and y-axis are thus "parallel transported" in the plane perpendicular to the z-axis, so that there is no torsion.

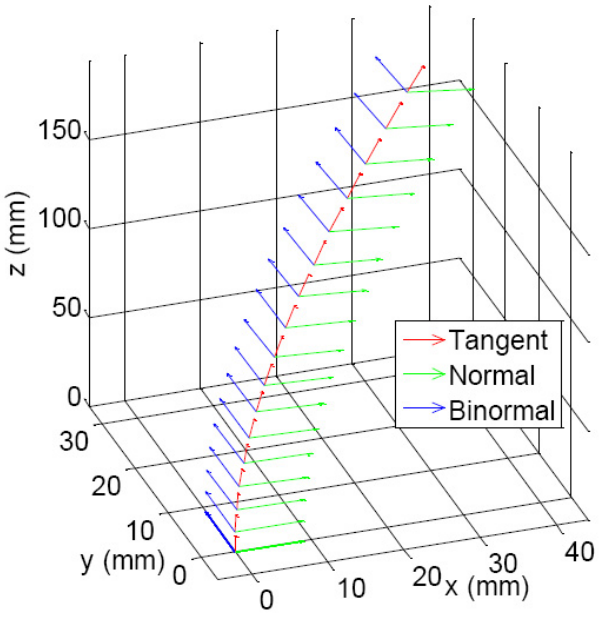

Figure 2.4: Orientation of Bishop Frames along a curve

It is noticed that, when the CBHA posture is straight, then all Frames are parallel to each others except for the Frame $\{\mathbf{x}_{\text{origin}}, \mathbf{y}_{\text{origin}}, \mathbf{z}_{\text{origin}}\}$.

© 2014 Tous droits réservés.

doc.univ-lille1.fr

Thèse de Coralie Escande, Lille 1, 2013

2.1.3 Parameters and Variables Definitions

In order to develop the kinematics of bending sections for the CBHA, the geometrical parameters and variables are introduced in this subsection and are indicated through Figure 2.5 for each j^{th} bending section in planar and spacial configurations ($\phi_j = 0$ and $\phi_j \neq 0$).

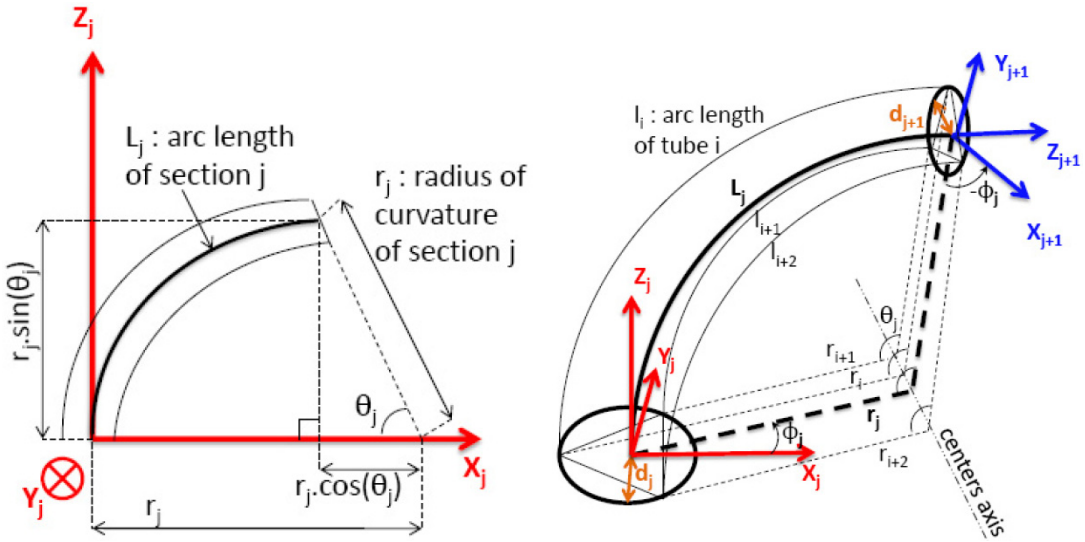

Figure 2.5: Geometrical representation of the j^{th} bending section of the CBHA: (a) Planar configuration with $\phi_j = 0$, (b) Spacial configuration with $\phi_j \neq 0$

- i refers to the tube number (see Figure 2.6);
- j refers to the section number (see Figure 2.6);
- r_j refers to the curvature radius of the j^{th} section, where the curvature K_j is defined by equation (2.1) as follows:

$$K_j = 1/r_j \tag{2.1}$$

- ϕ_j refers to the angle between x-axis and the projection of the j^{th} section in the plane $(O_j, \vec{x_j}, \vec{y_j})$;
- θ_j refers to the curvature angle of the j^{th} section;
- L_j refers to the length of the j^{th} section, and is expressed in equation (2.2) as follows:

$$\theta_j = K_j L_j \tag{2.2}$$

© 2014 Tous droits réservés.

doc.univ-lille1.fr

Thèse de Coralie Escande, Lille 1, 2013

- l_i refers to the length of the i^{th} tube, where $i = 1, .., 3$ for $j = 1$ and $i = 4, .., 6$ for $j = 2$.

Under the constant curvature assumption, the tubes describe a perfect arc of circle centered at point $[r_j; 0; 0]$ when $\phi_j = 0$.

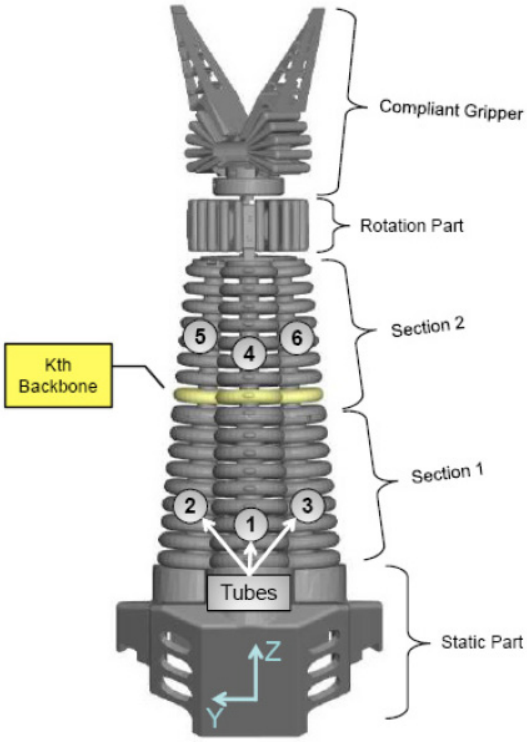

Figure 2.6: Definition of the tubes and sections numbering

2.2 Global Modeling Method

2.2.1 Problem Formulation

The forward kinematic modeling problem can be formulated as equation 2.3 and consists in finding the mathematical function, which allows calculating the pose $\{x, y, z, \Phi, \Theta, \Psi\}$ of the Frame $\{\mathbf{x}_4, \mathbf{y}_4, \mathbf{z}_4\}$ in terms of the tubes lengths $l_{i=1..6}$.

© 2014 Tous droits réservés.

doc.univ-lille1.fr

Thèse de Coralie Escande, Lille 1, 2013

$$\begin{pmatrix} x \\ y \\ z \\ \Phi \\ \Theta \\ \Psi \end{pmatrix} = f \begin{pmatrix} l_{i=1} \\ l_{i=2} \\ l_{i=3} \\ l_{i=4} \\ l_{i=5} \\ l_{i=6} \end{pmatrix} \tag{2.3}$$

2.2.2 Assumptions

Development of kinematic model for the bending sections is generally based on the constant curvature assumption which is commonly adopted for modeling continuum robots (Webster et al. 2010). Indeed, on the basis of this assumption, successful results are reported in many references such as (Chen et al. 2009b; Iqbal et al. 2009; Webster et al. 2010). This approximation has the advantage to simplify the modeling of such complex robots and allows using analytical Frames transformations. (Webster et al. 2010) presents also several arguments to explain the use of this assumption depending on the structure of the robot. Furthermore, for the sake of simplification, the conical shape of each section of the CBHA is assimilated to a cylinder, and the rotative part[12] is assumed to be static. Moreover, an inextensible central rod limiting the maximal length extension, the CBHA is considered as a non-extensible arm.

2.2.3 Modeling Method

Forward kinematic transformation refers to the set of kinematic equations allowing to determine the pose of the CBHA tip $\{x, y, z, \Phi, \Theta, \Psi\}$ provided by the tubes lengths $l_{i=1..6}$ of each bending section and by inherent geometrical parameters (see Figure 2.7). To calculate this transformation, a modular strategy has been adopted by using the configuration space representing the arc parameters of one bending section. The independent kinematic transformation expresses the pose in terms of these arc parameters. The specific kinematic transformation is then used to express the relationship between arc parameters and tube lengths. The global forward kinematic transformation can finally be calculated using simple algebraic transformation (Webster et al. 2010). For multi-section cases, these transformations have simply to be multiplied.

This modeling method associated to the aforementioned assumptions has been used successfully for the BHA (Rolf and Steil 2012).

[12]The rotative part can not move more than 45°, which is highly constraining the motion: it is then not practical to grip objects.

© 2014 Tous droits réservés.

doc.univ-lille1.fr

Thèse de Coralie Escande, Lille 1, 2013

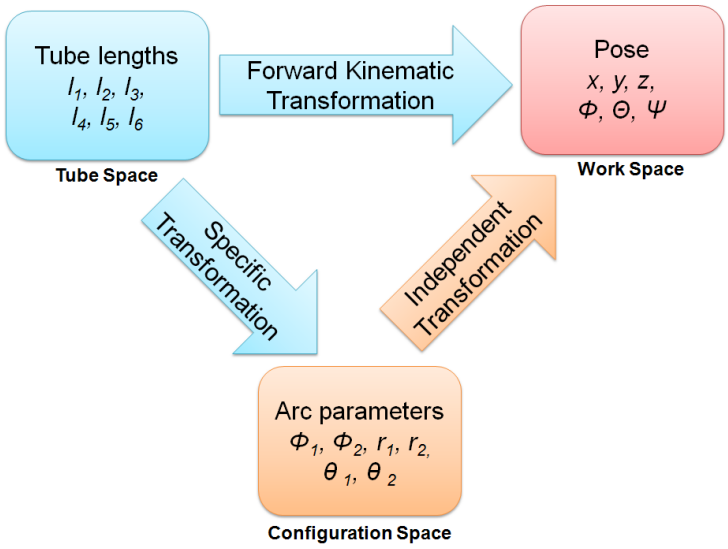

Figure 2.7: Global View of Modeling

2.3 Independent Kinematic Transformation

The purpose of the independant transformation is to calculate the pose $\{x, y, z, \Phi, \Theta, \Psi\}$ of the end-effector in function of the arc parameters $\{r_j, \phi_j, \theta_j\}$ of the j^{th} section.

2.3.1 Homogeneous Transformations

The FKM can be easily established using the homogeneous transformation matrices, given by equation (2.4).

$$ {}^{\text{origin}}_{4}\mathbf{T} = {}^{\text{origin}}_{1}\mathbf{T}\,{}^{1}_{2}\mathbf{T}\,{}^{2}_{3}\mathbf{T}\,{}^{3}_{4}\mathbf{T} \tag{2.4} $$

The transformation ${}^{\text{origin}}_{1}\mathbf{T}$ is constant and depends on the robot design only, while the transformations ${}^{1}_{2}\mathbf{T}$ and ${}^{2}_{3}\mathbf{T}$ depend respectively on the lengths of tubes $l_{i=1..3}$ and $l_{i=4..6}$. Finally ${}^{3}_{4}\mathbf{T}$ is assumed to be constant as explained in the assumptions section. In the next section, first the constant transformation matrices ${}^{\text{origin}}_{1}\mathbf{T}$ and ${}^{3}_{4}\mathbf{T}$ are described. They will be followed by a detailed explanation of the modeling development of the transformations ${}^{1}_{2}\mathbf{T}$ and ${}^{2}_{3}\mathbf{T}$.

2.3.2 Constant Transformation Matrices

The two constant transformations are illustrated in Figure 2.8.

The first constant transformation matrix ${}^{\text{origin}}_{1}\mathbf{T}$, shown in equation (2.5, corresponds to a constant translation of h_1 (in mm) along the z-axis, then a constant

© 2014 Tous droits réservés.

doc.univ-lille1.fr

Thèse de Coralie Escande, Lille 1, 2013

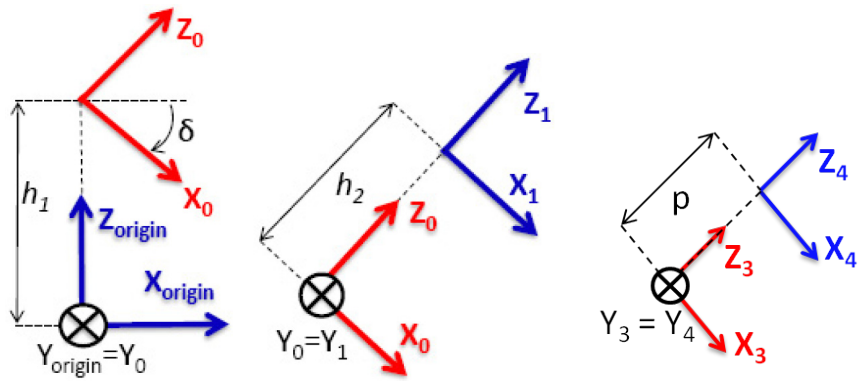

(a) (b) (c)

Figure 2.8: The two constant transformations: (a) and (b) decomposition of the first constant transformation ${}^{\text{origin}}_{1}\mathbf{T}$, (c) final constant transformation ${}^{3}_{4}\mathbf{T}$

rotation about δ (in rad) around the y-axis and finally a constant translation of h_2 (in mm) along the z-axis.

$$ {}^{\text{origin}}_{1}\mathbf{T} = \begin{bmatrix} \cos\delta & 0 & \sin\delta & h_2 \sin\delta \\ 0 & 1 & 0 & 0 \\ -\sin\delta & 0 & \cos\delta & h_2\cos\delta + h_1 \\ 0 & 0 & 0 & 1 \end{bmatrix} \tag{2.5} $$

The second constant transformation matrix ${}^{3}_{4}\mathbf{T}$, shown in equation (2.6), is calculated geometrically, where p is the distance (in mm) between the center of the basis of the rotative part and of the end-effector.

$$ {}^{3}_{4}\mathbf{T} = \begin{bmatrix} 1 & 0 & 0 & 0 \\ 0 & 1 & 0 & 0 \\ 0 & 0 & 1 & p \\ 0 & 0 & 0 & 1 \end{bmatrix} \tag{2.6} $$

The nominal values of h_1, δ, h_2 and p are calculated from the Computer-Aided Design (CAD) model of the CBHA. The other transformation matrices of the bending sections are detailed in the following subsection.

2.3.3 Kinematic Transformations of Bending Sections

The homogeneous transformation matrix $\mathbf{T}_j$ between the Frames $\{\mathbf{x}_j, \mathbf{y}_j, \mathbf{z}_j\}$ and $\{\mathbf{x}_{j+1}, \mathbf{y}_{j+1}, \mathbf{z}_{j+1}\}$ of the j^{th} section can be written as shown in equation (2.7a). The two rotation matrices $\mathbf{R}_z(\phi_j)$ and $\mathbf{R}_y(\theta_j)$ are given respectively by equations (2.7b) and (2.7c), and the translation vector $\mathbf{p}_j$ is deduced from Figure 2.5 as

© 2014 Tous droits réservés.

doc.univ-lille1.fr

Thèse de Coralie Escande, Lille 1, 2013

shown by equation (2.7d).

$$\mathbf{T}_j = \begin{bmatrix} \mathbf{R}_z(\phi_j) & 0 \\ 0 & 1 \end{bmatrix} \begin{bmatrix} \mathbf{R}_y(\theta_j) & \mathbf{p}_j \\ 0 & 1 \end{bmatrix} \tag{2.7a}$$

$$\mathbf{R}_z(\phi_j) = \begin{bmatrix} \cos\phi_j & -\sin\phi_j & 0 \\ \sin\phi_j & \cos\phi_j & 0 \\ 0 & 0 & 1 \end{bmatrix} \tag{2.7b}$$

$$\mathbf{R}_y(\theta_j) = \begin{bmatrix} \cos\theta_j & 0 & \sin\theta_j \\ 0 & 1 & 0 \\ -\sin\theta_j & 0 & \cos\theta_j \end{bmatrix} \tag{2.7c}$$

$$\mathbf{p}_j = \begin{bmatrix} r_j(1-\cos\theta_j) \\ 0 \\ r_j\sin\theta_j \end{bmatrix} \tag{2.7d}$$

Finally, by substituting equations (2.7b), (2.7c) and (2.7d) into equations (2.7a), then the transformation matrix $\mathbf{T}_j$ can be expressed as shown by equation (2.8) as follows:

$$\mathbf{T}_j = \begin{bmatrix} c\phi_j c\theta_j & -s\phi_j & c\phi_j s\theta_j & r_j c\phi_j(1-c\theta_j) \\ s\phi_j c\theta_j & c\phi_j & s\phi_j s\theta_j & r_j s\phi_j(1-c\theta_j) \\ -s\theta_j & 0 & c\theta_j & r_j s\theta_j \\ 0 & 0 & 0 & 1 \end{bmatrix} \tag{2.8}$$

, where r_j is the curvature radius of the bending j^{th} section, and where $c\phi_j = \cos\phi_j$, $s\phi_j = \sin\phi_j$, $c\theta_j = \cos\theta_j$, and $s\theta_j = \sin\theta_j$, with $j = 1, 2$.

In the transformation matrix (2.8), and according to (Webster et al. 2010), the tip Frame is aligned so that the x-axis points towards the circle center and the z-axis is tangent with this circle. However the tip has to be oriented such that it aligns with the base Frame when it slides along the arc towards the basis in order to be able to multiply the transformation matrices in the case of multi-section. For that, it is needed to post multiply equation (2.8) by a homogeneous transformation with rotation matrix $\mathbf{R}_z(-\phi_j)$ and zero translation. Thus, the final transformation matrix for one section is calculated as in following equation (2.9), where the developed equation is given in (2.10).

$$^{j}_{j+1}\mathbf{T} = \mathbf{T}_j\mathbf{R}_z(-\phi_j) \tag{2.9}$$

© 2014 Tous droits réservés.

doc.univ-lille1.fr

Thèse de Coralie Escande, Lille 1, 2013

$$T = \begin{bmatrix} c^2\phi_j c\theta_j + s^2\phi_j & c\phi_j s\phi_j(c\theta_j - 1) & c\phi_j s\theta_j & r_j c\phi_j(1 - c\theta_j) \\ c\phi_j s\phi_j(c\theta_j - 1) & s^2\phi_j c\theta_j + c^2\phi_j & s\phi_j s\theta_j & r_j s\phi_j(1 - c\theta_j) \\ -c\phi_j s\theta_j & -s\phi_j s\theta_j & c\theta_j & r_j s\theta_j \\ 0 & 0 & 0 & 1 \end{bmatrix} \tag{2.10}$$

The independent transformation is a function of the arc parameters $\{r_j, \phi_j, \theta_j\}$ of the j^{th} section. Now, these parameters can be expressed in terms of tube lengths l_i, as described in the following section.

2.4 Specific Kinematic Transformation

The purpose of the specific transformation is to calculate the arc parameters $\{r_j, \phi_j, \theta_j\}$ of the j^{th} section in function of the tube lengths l_i.

2.4.1 Calculation of the Specific Kinematic Transformation

The calculation of this transformation is based on preliminary equations deduced from the Figure 2.9. This figure illustrates a top view of the j^{th} bending section with the Frame of the basis of the $(j+1)^{\text{th}}$ section. For the following calculation, it is assumed that $i = 1$ when $j = 1$ and $i = 4$ when $j = 2$, with $i \in [1; 6]$ and $j \in [1; 2]$.

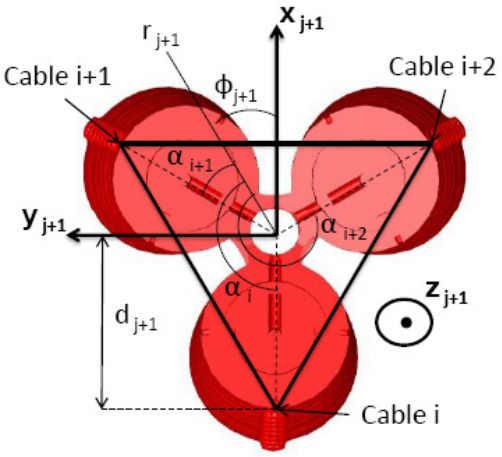

Figure 2.9: Top view of the j^{th} bending section

From Figure 2.9, the following is deduced:

© 2014 Tous droits réservés.

doc.univ-lille1.fr

Thèse de Coralie Escande, Lille 1, 2013

- the angles α_i, α_{i+1}, and α_{i+2} which are expressed in equation (2.11) are a function of ϕ_j

$$\begin{cases} \alpha_i = \pi - \phi_j \\ \alpha_{i+1} = \frac{\pi}{3} - \phi_j \\ \alpha_{i+2} = \frac{5\pi}{3} - \phi_j \end{cases} \tag{2.11}$$

- the distance d_j between the center of the j^{th} bending section and the location of each potentiometer's cable of this j^{th} section.

It is worth noting that the form of the CBHA is conic (see Figure 2.10) and the tubes are not exactly parallel. For simplification reasons for the kinematic model calculation, it is assumed that each section is approximated to a cylinder with a median value d_j of the radius (Figure 2.10). Each radius corresponds to the distance between the center of the CBHA and the location of the j^{th} cable potentiometer.

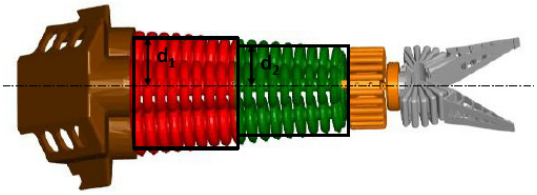

Figure 2.10: Definition of the radius d_1 and d_2

When the j^{th} section is curved, it describes a perfect arc of circle. This means that the center of the whole section describes an arc of circle with the center point $[r_j; 0; 0]^{\text{T}}$ when $\phi_j = 0$. This means also that the center of each tube describes an arc of circle with the center point $[r_i; 0; 0]^{\text{T}}$ when $\phi_j = 0$. This aspect can be described by (2.12) based on the Figure (2.11), where r_j is the curvature radius of the j^{th} section and r_i is the curvature radius of the i^{th} cable.

$$\begin{cases} r_i = r_j - d_j \cos(\alpha_i) \\ r_{i+1} = r_j - d_j \cos(\alpha_{i+1}) \\ r_{i+2} = r_j - d_j \cos(\alpha_{i+2}) \end{cases} \tag{2.12}$$

Each arc of circle is defined by its intrinsic parameters $\{r_j, \theta_j, L_j\}$ that are related by equations (2.13) deduced from equations (2.12), (2.1) and (2.2).

$$\begin{cases} l_i = L_j - d_j \theta_j \cos(\alpha_i) \\ l_{i+1} = L_j - d_j \theta_j \cos(\alpha_{i+1}) \\ l_{i+2} = L_j - d_j \theta_j \cos(\alpha_{i+2}) \end{cases} \tag{2.13}$$

© 2014 Tous droits réservés.

doc.univ-lille1.fr

Thèse de Coralie Escande, Lille 1, 2013

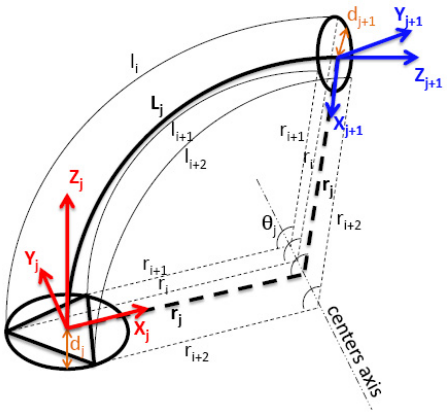

Figure 2.11: View of the different curvature radius for one bending section ($\phi_j = 0$)

Adding the equations of the system (2.13) results in the following equation:

$$3L = l_i + l_{i+1} + l_{i+2} + d_j\theta_j(\cos(\alpha_i) + \cos(\alpha_{i+1}) + \cos(\alpha_{i+2})) \tag{2.14}$$

Note that the values of the angles α_i, α_{i+1} and α_{i+2} are interdependent and verify the relation expressed by equation (2.15).

$$\cos(\alpha_i) + \cos(\alpha_{i+1}) + \cos(\alpha_{i+2}) = 0 \tag{2.15}$$

Combining the equation (2.14) and (2.15), the relation between the arc length L_j of the j^{th} section and the length l_i of the i^{th} cable can be written as indicated in following equation (2.16).

$$\boxed{L_j = \frac{l_i + l_{i+1} + l_{i+2}}{3}} \tag{2.16}$$

2.4.1.1 Calculation of the Orientation Angle

In order to calculate the orientation angle ϕ_j, the terms L_j and $d_j\theta_j$ have to be eliminated from the equations system (2.13). This leads to the following equation (2.17).

$$\frac{l_{i+1} - l_i}{\cos(\alpha_i) - \cos(\alpha_{i+1})} = \frac{l_{i+2} - l_{i+1}}{\cos(\alpha_{i+1}) - \cos(\alpha_{i+2})} \tag{2.17}$$

By combining equations (2.17) and (2.11), the expression of the orientation angle can be obtained as shown in expression (2.18) [13].

[13]The inverse tangent function has to be computed as "*atan2*" function in order to take into

© 2014 Tous droits réservés.

doc.univ-lille1.fr

Thèse de Coralie Escande, Lille 1, 2013

$$\boxed{\phi_j = \tan^{-1}\left(\frac{\sqrt{3}(l_{i+2} - l_{i+1})}{(2l_i - l_{i+1} - l_{i+2})}\right)} \tag{2.18}$$

2.4.1.2 Calculation of the Curvature Radius

To calculate the curvature r_j, equations (2.1) and (2.2) are combined with equation (2.13) to obtain the following equation (2.19).

$$K_j = \frac{L_j - l_i}{L_j d_j \cos(\alpha_i)} \tag{2.19}$$

Substituting equations (2.11) and (2.18) in equation (2.19) and using the trigonometric simplifications, the final expression of the curvature radius r_j can then be written as follows:

$$\boxed{r_j = \frac{(l_i + l_{i+1} + l_{i+2})d_j}{D_j}} \tag{2.20a}$$

, where:

$$\boxed{D_j = 2\sqrt{l_i^2 + l_{i+1}^2 + l_{i+2}^2 - l_i l_{i+1} - l_i l_{i+2} - l_{i+1} l_{i+2}}} \tag{2.20b}$$

2.4.1.3 Calculation of the Curvature Angle

To calculate the curvature angle θ_j, equations (2.1) and (2.2) are combined with equation (2.20a) to obtain the expression (2.21) as follows:

$$\boxed{\theta_j = \frac{D_j}{3d_j}} \tag{2.21}$$

2.4.2 Singularities

Practically, the straight posture of a section[14] leads to a singularity because of an infinite curvature radius. Three singularity configurations are defined as follows:

- the first bending section is in straight posture while the second bending section is curved;

account the four-quadrant of the trigonometric circle. Indeed the function "*atan2*" gives results in the closed interval $[-\pi; \pi]$, unlike the function "*atan*", which gives results in the closed interval $[\frac{-\pi}{2}; \frac{\pi}{2}]$.

[14] The straight posture is defined by identical tubes lengths, where $r_j = \infty$, $D_j = 0$, $\theta_j = 0$, and ϕ_j is undefined.

© 2014 Tous droits réservés.

doc.univ-lille1.fr

Thèse de Coralie Escande, Lille 1, 2013

- the second bending section is in straight posture while the first bending section is curved;
- the two bending sections are in straight posture at the same time.

However, this singular case is easily handled by using the constant transformation matrix ${}^{j}_{j+1}\mathbf{T}_s$ expressed in (2.22) instead of ${}^{j}_{j+1}\mathbf{T}$ given by (2.8).

$$ {}^{j}_{j+1}\mathbf{T}_s = \begin{bmatrix} 1 & 0 & 0 & 0 \\ 0 & 1 & 0 & 0 \\ 0 & 0 & 1 & l_i \\ 0 & 0 & 0 & 1 \end{bmatrix} \tag{2.22} $$

In order to avoid switching between normal mode and singular mode, it is proposed to derive each element of the forward transformation of each section using multivariate Taylor series expansion (Godage et al. 2011).

Another issue of the singularity problem is addressed in terms of numerical stability and consists in studying the limits of the expression of a bending section forward transformation when θ_j tends toward 0 (Rolf and Steil 2012).

2.5 Orientations

The purpose of this section is to identify the orientations $\{\Phi, \Theta, \Psi\}$ of the Frame $\{\mathbf{x}_4, \mathbf{y}_4, \mathbf{z}_4\}$ associated to the end-effector. Various representations of the orientation exist in the literature, such as Euler angles and Quaternions (Khalil and Dombre 1999). In the studied case, the convention Yaw-Pitch-Roll is used, where $\{\Phi, \Theta, \Psi\}$ correspond respectively to the rotations around z-axis, y-axis, and x-axis. The identification of the orientations is based on the method described in (Khalil and Dombre 1999; Siciliano et al. 2009; Spong et al. 2006).

From (2.9), the direction cosine matrix ${}^{\text{origin}}_{4}\mathbf{R}$ is defined and setup as (2.23). The development of this matrix is given in (2.24) page 44. The next step consists in multiplying per $\mathbf{R}z(-\Phi)$ the left of the expression as in (2.25) to simplify the identification. The development of this expression is given in (2.26) page 44.

$$ {}^{\text{origin}}_{4}\mathbf{R} = \begin{bmatrix} r_{11} & r_{12} & r_{13} \\ r_{21} & r_{22} & r_{23} \\ r_{31} & r_{32} & r_{33} \end{bmatrix} = \mathbf{R}_z(\Phi).\mathbf{R}_y(\Theta).\mathbf{R}_x(\Psi) \tag{2.23} $$

$$ \mathbf{R}_z(-\Phi)\,{}^{\text{origin}}_{4}\mathbf{R} = \mathbf{R}_y(\Theta)\mathbf{R}_x(\Psi) \tag{2.25} $$

The orientation Φ can then be identified with the orientation matrix elements (2,1) of the expression (2.26), yielding to (2.28)

© 2014 Tous droits réservés.

doc.univ-lille1.fr

Thèse de Coralie Escande, Lille 1, 2013

$$R_z(\Phi).R_y(\Theta).R_x(\Psi) = \begin{bmatrix} \cos\Phi\cos\Theta & \cos\Phi\cos\Theta\sin\Psi - \sin\Phi\cos\Psi & \cos\Phi\sin\Theta\cos\Psi + \sin\Phi\sin\Psi \\ \sin\Phi\cos\Theta & \sin\Phi\sin\Theta\sin\Psi + \cos\Phi\cos\Psi & \sin\Phi\sin\Theta\sin\Psi - \cos\Phi\cos\Psi \\ -\sin\Theta & \cos\Theta\sin\Psi & \cos\Theta\cos\Psi \end{bmatrix} \tag{2.24}$$

$$\begin{bmatrix} r_{11}\cos\Phi + r_{21}\sin\Phi & r_{12}\cos\Phi + r_{22}\sin\Phi & r_{13}\cos\Phi + r_{23}\sin\Phi \\ -r_{11}\sin\Phi + r_{21}\cos\Phi & -r_{12}\sin\Phi + r_{22}\cos\Phi & -r_{13}\sin\Phi + r_{23}\cos\Phi \\ r_{31} & r_{32} & r_{33} \end{bmatrix} = \begin{bmatrix} \cos\Theta & \sin\Theta\sin\Psi & \sin\Theta\cos\Psi \\ 0 & \cos\Psi & -\sin\Psi \\ -\sin\Theta & \cos\Theta\sin\Psi & \cos\Theta\cos\Psi \end{bmatrix} \tag{2.26}$$

$$-r_{11}\sin\Phi + r_{21}\cos\Phi = 0 \tag{2.27}$$

$$\boxed{\begin{cases} \Phi = \arctan 2(r_{21}, r_{11}) \\ or \\ \Phi = \arctan 2(-r_{21}, -r_{11}) \end{cases}} \tag{2.28}$$

The identification of the other orientations Θ and Ψ can be done using the orientation matrix elements (1,1), (3,1) and (2,2), (2,3) of the expression (2.26) as mentioned in (2.30) and (2.32).

$$\begin{cases} r_{11}\cos\Phi + r_{21}\sin\Phi = \cos\Theta \\ r_{31} = -\sin\Theta \end{cases} \tag{2.29}$$

$$\boxed{\Theta = \arctan 2(-r_{31}, r_{11}\cos\Phi + r_{21}\sin\Phi)} \tag{2.30}$$

$$\begin{cases} -r_{12}\sin\Phi + r_{22}\cos\Phi = \cos\Psi \\ -r_{13}\sin\Phi + r_{23}\cos\Phi = -\sin\Psi \end{cases} \tag{2.31}$$

$$\boxed{\Psi = \arctan 2(r_{13}\sin\Phi - r_{23}\cos\Phi, -r_{12}\sin\Phi + r_{22}\cos\Phi)} \tag{2.32}$$

© 2014 Tous droits réservés.

doc.univ-lille1.fr

Thèse de Coralie Escande, Lille 1, 2013

2.6 Experiment and Validation

The goal of this section is to describe the experimental test bench and validation for the obtained FKM of the CBHA.

2.6.1 Description of the Test Bench

The test bench used in this experiment is a trilateration-based system. It allows us to validate a part of the FKM corresponding to the relationship between the Cartesian coordinates of the extremity target of the second bending section with the tube length. The validation of the orientation part of the model will be done through another experimental test bench, described in the next chapter. The experiment is done only with the CBHA, without the gripper and in absence of the mobile omnidrive platform. This test bench (Figure 2.12) is composed of:

- 1 profiled metallic platform with size of 700×700 mm;
- 4 external proportional wire-potentiometers[15] fixed on profiled metallic posts;
- 8 proportional valves supplying 2.5 *bar* for each tube: 3 for the first section, 3 for the second section, and 2 for the rotation part. The proportional valves for rotation part are not used for these experiments;
- 6 embedded proportional wire-potentiometers[15] placed along the tubes measuring the voltage corresponding to the tube length variation;
- 1 Input/Output control board of *DSpace* interfaced with programs developed in *MatLab/Simulink* and *ControlDesk* softwares.

The 4 measurements of the external wire-potentiometers are used to estimate the position of the tip of the CBHA, thanks to trilateration calculation. The 6 measurements of the embedded wire-potentiometers are inputs of the FKM. The obtained results compare the Cartesian coordinates of the CBHA tip, calculated from the analytical model with those calculated from the adapted trilateration. An overview of the global architecture is given in Figure 2.13.

[15]The accuracy of the wire-potentiometer (Microepsilon 2013) is defined by two parameters: the linearity (0.5 mm +/− 0.1 FSO for external potentiometers and 0.75 mm +/− 0.1 FSO for embedded potentiometers) and the resolution (0.15 mm for external potentiometers and 0.2 mm for embedded potentiometers).

© 2014 Tous droits réservés.

doc.univ-lille1.fr

Thèse de Coralie Escande, Lille 1, 2013

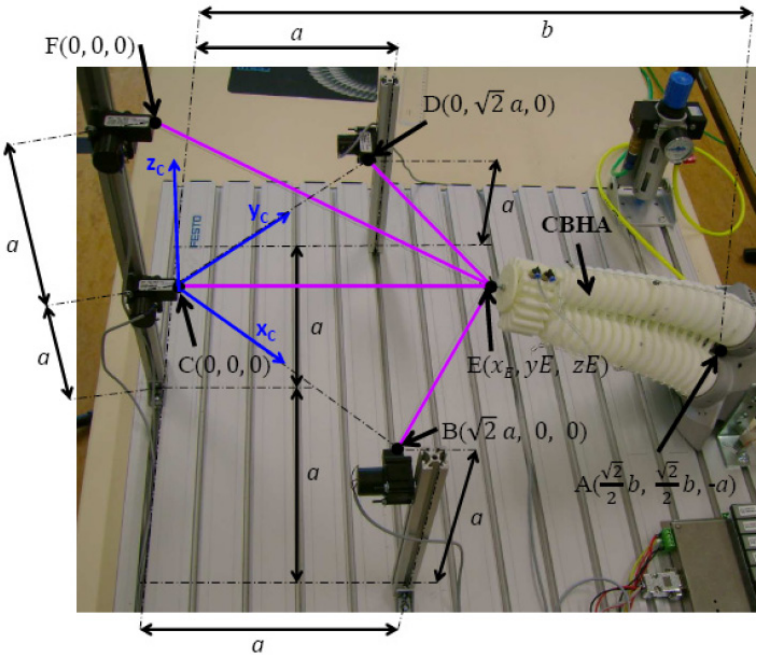

(a)

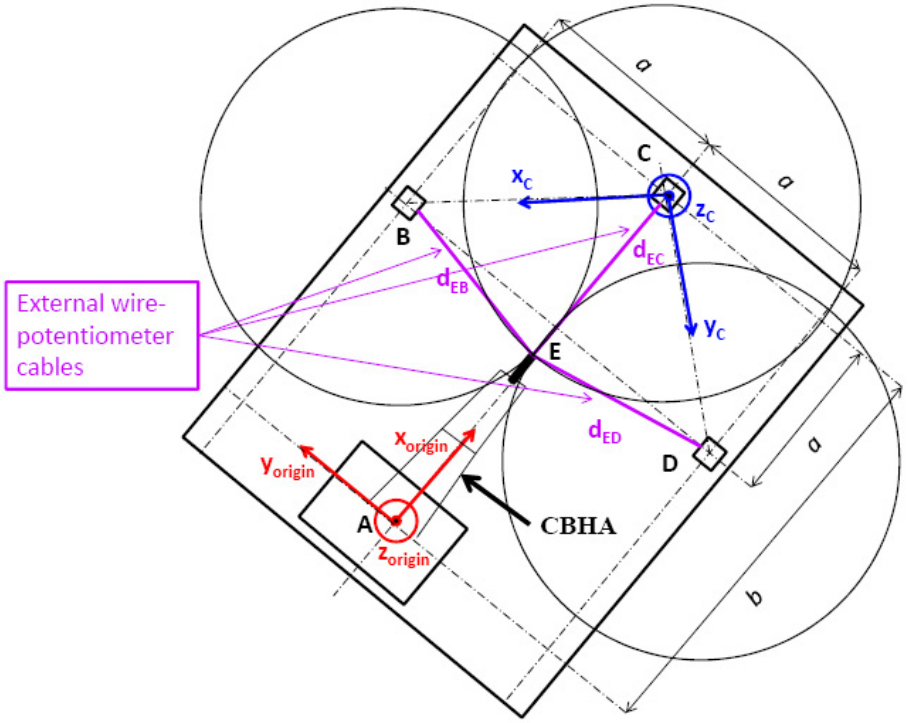

(b)

Figure 2.12: Overview of the trilateration test bench: (a) Photo of the test bench with the dimensions and the point coordinates , (b) Geometric Sketch of the test bench (top view)

© 2014 Tous droits réservés.

doc.univ-lille1.fr

Thèse de Coralie Escande, Lille 1, 2013

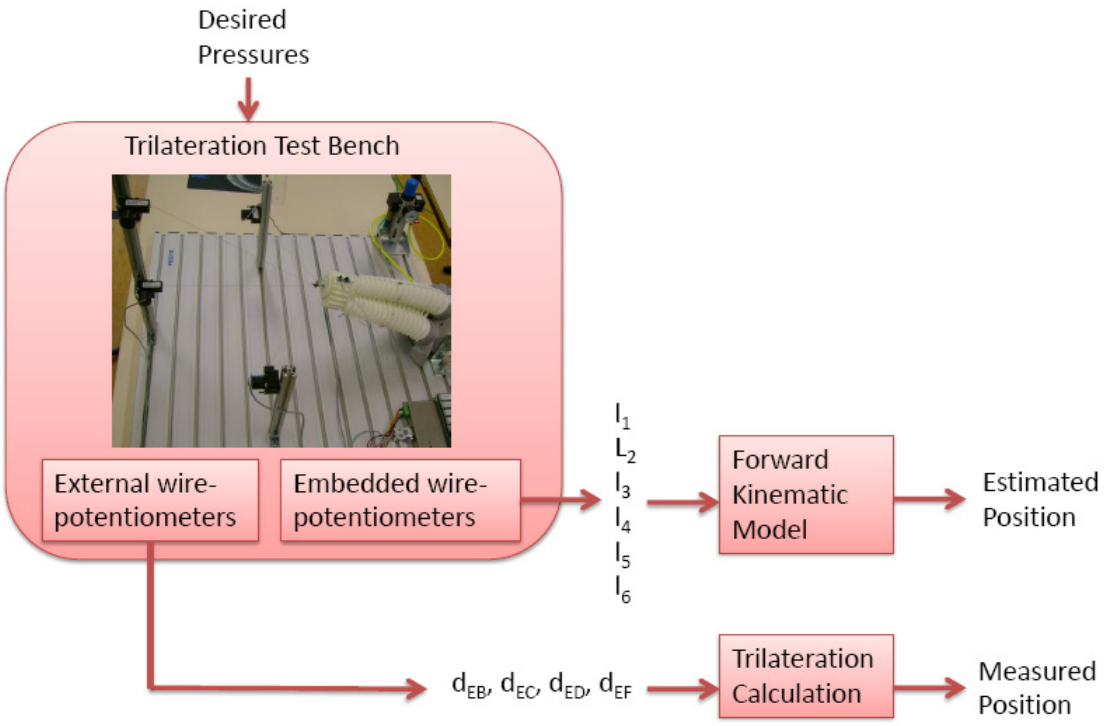

Figure 2.13: Overview of the trilateration test bench architecture

© 2014 Tous droits réservés.

doc.univ-lille1.fr

Thèse de Coralie Escande, Lille 1, 2013

2.6.1.1 Description of the Sensors Calibration

The wire-potentiometers are delivering voltages which are proportional to the measured lengths. The transformation between voltage and length is done with a calibrated equation adapted to the test bench. The nominal transformation equation of the wire-potentiometers is given in equation (2.33), where l_{nominal} is the nominal length corresponding to v_{nominal}, M_{nominal} is the maximal length of the wire-potentiometer [16], v_{nominal} is the voltage given by the wire-potentiometer, and S_{nominal} is the voltage source [17]. The integer gain of 10 is used because the DSpace input/output board limits the output analog value to its decimal nominal value.

$$l_{\text{nominal}} = \frac{10 M_{\text{nominal}} v_{\text{nominal}}}{S_{\text{nominal}}} \tag{2.33}$$

Equation 2.33 is suited for the external wire-potentiometer but not those embedded on the CBHA, used to measure the tubes elongation. Indeed, the embedded wire-potentiometers are installed under the trunk, measuring then the tubes lengths in addition with a dead length which is different for each tube. Moreover, each wire-potentiometer of the second section measures also the tube lengths of the first bending section. An adapted calibration has to be done with different measurements shown in Table 2.1, where $i \in [1;6]$ is the tube number, v^i_{measured} is the measured voltage of the embedded wire-potentiometer attached to the tube i, l^i_{measured} is the measured length of the embedded wire-potentiometer attached to tube i, v^i_{nominal} is the nominal voltage corresponding to the measured length, and d^i_v is the following subtraction: $v^i_{\text{measured}} - v^i_{\text{nominal}}$.

Table 2.1: Potentiometer Calibration Table

Tube i	v^i_{measured} [V]	l^i_{measured} [mm]	v^i_{nominal} [V]	d^i_v [V]
1	0.41	100	0.2	0.21
2	0.35	100	0.2	0.15
3	0.39	100	0.2	0.19
4	0.56	200	0.4	0.16
5	0.61	200	0.4	0.21
6	0.57	200	0.4	0.17

[16] in our case, $M_{\text{nominal}} = 750\ mm$ for the external wire-potentiometer and $M_{\text{nominal}} = 500\ mm$ for the embedded wire-potentiometers

[17] in our case $S_{\text{nominal}} = 10\ V$

© 2014 Tous droits réservés.

doc.univ-lille1.fr

Thèse de Coralie Escande, Lille 1, 2013

Thus, the resulting equation of calibration is represented by (2.34), where l^i_{measured} is the measured length of the wire-potentiometer attached to the tube i, d^i_v is the voltage difference $v^i_{\text{measured}} - v^i_{\text{nominal}}$, M_{nominal} is the maximal length of the wire-potentiometer [16], S_{nominal} is the voltage source[17]. Moreover, the cables of the wire-potentiometers of the second bending section measuring also the tube lengths of the first bending section, some subtraction needs to be done as shown in the equation system 2.35.

$$l^i_{\text{measured}} = \frac{10 M_{\text{nominal}}(v^i_{\text{measured}} - d^i_v)}{S_{\text{nominal}}} \tag{2.34}$$

$$\begin{cases} l_1 = l^1_{\text{measured}} \\ l_2 = l^2_{\text{measured}} \\ l_3 = l^3_{\text{measured}} \\ l_4 = l^4_{\text{measured}} - l^1_{\text{measured}} \\ l_5 = l^5_{\text{measured}} - l^2_{\text{measured}} \\ l_6 = l^6_{\text{measured}} - l^3_{\text{measured}} \end{cases} \tag{2.35}$$

2.6.1.2 Adapted Trilateration

The principle of the trilateration consists in calculating the intersection of 3 spheres by a radius measured with the external wire-potentiometers placed with the same height. However, this method does not allow knowing the sign of the z-coordinate value. To solve this problem, an additional wire-potentiometer[18] is used to measure the radius of a fourth sphere. In the following, the calculation of the Cartesian coordinates of the CBHA tip is developed.

The Frame used for the trilateration has been placed at the origin position $C(0, 0, 0)$, shown in Figure 2.12 in order to simplify the calculations. The points A, B, C, D, E, and F are defined as follows:

- A is the origin point of the CBHA placed at $A(\frac{b\sqrt{2}}{2}, \frac{b\sqrt{2}}{2}, -a)$ from the origin point $C(0, 0, 0)$;
- B and D are positions of lateral external wire-potentiometers which are located at the same height of C, where $B(\sqrt{2}a, 0, 0)$ and $D(0, \sqrt{2}a, 0)$;
- F corresponds to the position of the fourth external wire-potentiometer which is above the point C, where $F(0, 0, a)$;
- E is the position of the tip of the CBHA, where $E(x_{\text{E}}, y_{\text{E}}, z_{\text{E}})$ is the unknown Cartesian coordinates in the trilateration problem.

[18] placed on the double height

© 2014 Tous droits réservés.

doc.univ-lille1.fr

Thèse de Coralie Escande, Lille 1, 2013

The external wire-potentiometers are fixed to point E so that we can identify the distances d_{EB}, d_{EC}, d_{ED}, and d_{EF} representing the radius of the 4 different spheres (see Figure 2.12).

Equations of the four spheres are given by the system (2.36), expressed in terms of unknown coordinates of the CBHA tip $\{x_{\mathrm{E}}, y_{\mathrm{E}}, z_{\mathrm{E}}\}$.

$$\begin{cases} d_{\mathrm{EB}}^2 = (x_{\mathrm{E}} - \sqrt{2}a)2 + y_{\mathrm{E}}^2 + z_{\mathrm{E}}^2 \\ d_{\mathrm{EC}}^2 = x_{\mathrm{E}}^2 + y_{\mathrm{E}}^2 + z_{\mathrm{E}}^2 \\ d_{\mathrm{ED}}^2 = x_{\mathrm{E}}^2 + (y_{\mathrm{E}} - \sqrt{2}a)^2 + z_{\mathrm{E}}^2 \\ d_{\mathrm{EF}}^2 = x_{\mathrm{E}}^2 + y_{\mathrm{E}}^2 + (z_{\mathrm{E}} - a)^2 \end{cases} \tag{2.36}$$

The difference between the two first equations of the system (2.36) allows deducing the expression of x_{E} (2.37). Then, expression of y_{E} (2.38) is obtained from the combination of the second and third equations of the system (2.36). Finally, z_{E} is deduced from the difference of the fourth and second equations of the system (2.36).

$$x_{\mathrm{E}} = \frac{d_{\mathrm{EC}}^2 - d_{\mathrm{EB}}^2 + 2a^2}{2\sqrt{2}a} \tag{2.37}$$

$$y_{\mathrm{E}} = \frac{x_{\mathrm{B}}^2 + d_{\mathrm{EC}}^2 - d_{\mathrm{ED}}^2}{2\sqrt{2}a} \tag{2.38}$$

$$z_{\mathrm{E}} = \pm\frac{d_{\mathrm{EF}}^2 - d_{\mathrm{EC}}^2 - a^2}{2a} \tag{2.39}$$

To obtain the sign of z_{E}, the distances d_{EC} and D_{EF} are compared. Figure 2.14 shows different zones where the sign of z_{E} can be calculated. They are described by the equations (2.40), (2.41) and by the system (2.42).

$$z_{\mathrm{E}} = 0 \Leftrightarrow \left\{ d_{\mathrm{EF}} = \sqrt{a^2 + d_{\mathrm{EC}}^2} \right\} \tag{2.40}$$

$$z_{\mathrm{E}} < 0 \Leftrightarrow \left\{ (d_{\mathrm{EC}} < d_{\mathrm{EF}}) \& (d_{\mathrm{EF}} > \sqrt{a^2 + d_{\mathrm{EC}}^2}) \right\} \tag{2.41}$$

$$z_{\mathrm{E}} > 0 \Leftrightarrow \left\{ \begin{array}{c} d_{\mathrm{EC}} \geq D_{\mathrm{EF}} \\ or \\ (d_{\mathrm{EC}} < \sqrt{a^2 + d_{\mathrm{EC}}^2}) \& (d_{\mathrm{EC}} < D_{\mathrm{EF}}) \end{array} \right\} \tag{2.42}$$

The position calculated by the adapted trilateration gives the position of the tip of the CBHA in a Frame different from that used by the model calculation. The trilateration calculates the position of the CBHA tip in the Frame $\{\mathbf{x}_{\mathrm{C}}, \mathbf{y}_{\mathrm{C}}, \mathbf{z}_{\mathrm{C}}\}$ placed on point C, while the kinematic model calculates the position of the CBHA

© 2014 Tous droits réservés.

doc.univ-lille1.fr

Thèse de Coralie Escande, Lille 1, 2013

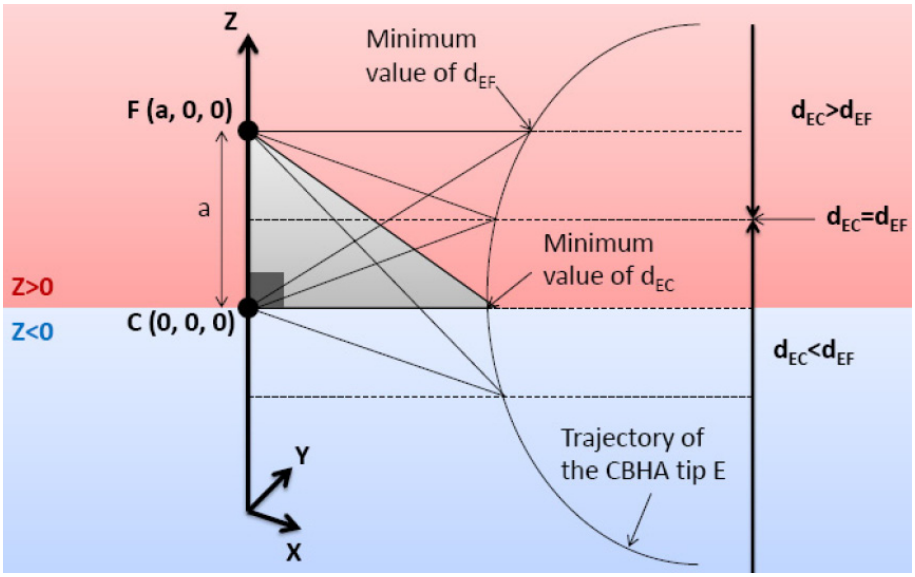

Figure 2.14: Side view of the possible configurations of the external potentiometers

tip in the Frame $\{\mathbf{x}_{\text{origin}}, \mathbf{y}_{\text{origin}}, \mathbf{z}_{\text{origin}}\}$ placed on point A. Thus, the following matrix transformation (2.43) is used to describe the geometric transformations between the two Frames shown in Figure 2.12.

$$ {}^{\text{C}}_{\text{origin}}\mathbf{T} = \begin{bmatrix} \cos\gamma & -\sin\gamma & 0 & b\cos\gamma \\ \sin\gamma & \cos\gamma & 0 & b\sin\gamma \\ 0 & 0 & 1 & a \\ 0 & 0 & 0 & 1 \end{bmatrix} \tag{2.43} $$

2.6.2 Results and Discussion

For the experimental validation, the constant parameters shown in Table 2.2 have been manually measured.

Table 2.2: Constant parameters Values

Parameter	Value	Unit
a	185	mm
b	570	mm
γ	$\frac{3\pi}{4}$	rad

Three trajectories are generated and compared for the FKM validation of the CBHA. They correspond to the trajectories of the CBHA tip $\{x_{\text{E}}, y_{\text{E}}, z_{\text{E}}\}$, issued

© 2014 Tous droits réservés.

doc.univ-lille1.fr

Thèse de Coralie Escande, Lille 1, 2013

from both trilateration technique and the FKM. Each trajectory has been realized in 10 sec, corresponding to 2501 captures of position. For each trajectory, errors on x, y and z and euclidean errors are deduced. The first trajectory (Figure 2.15) has been realized by varying in open-loop the air pressure for each tube individually of the first bending section. The second trajectory (Figure 2.17) explores the maximum workspace in all directions based on the motion of the second bending section. Finally, the third trajectory (Figure 2.19) corresponds to a movement combining both bending sections. Figures 2.16, 2.18 and 2.20 show respectively the euclidean error between the trilateration and the FKM calculations.

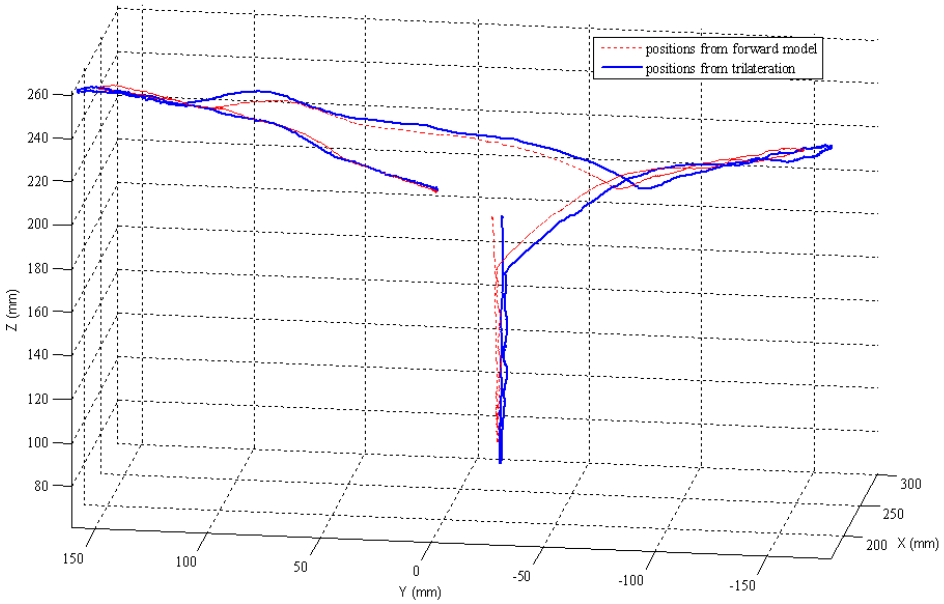

Figure 2.15: Trajectory 1: only the first bending section is moving

For this experiment, with the used tube length of the CBHA, it is assumed that the curvature of the tubes is a perfect arc of circle. This assumption has been considered in order to simplify the calculation of the model, but it is different in the case of long bending section of the CBHA. Moreover, the structure of the CBHA in a straight posture describes a conical form in the real case, while for the modeling, it is assumed as a cylindrical form for each bending section. These two modeling assumptions are sources of uncertainties. The CBHA is a succession of Polyamide-based backbones, and the characteristic of this material combined to the structure of the CBHA are not well-known. This modeling uncertainty can be considered in the calibration of the parameters showed in the next chapter. In addition, the pneumatic actuators are known to be inaccurate for positioning

© 2014 Tous droits réservés.

doc.univ-lille1.fr

Thèse de Coralie Escande, Lille 1, 2013

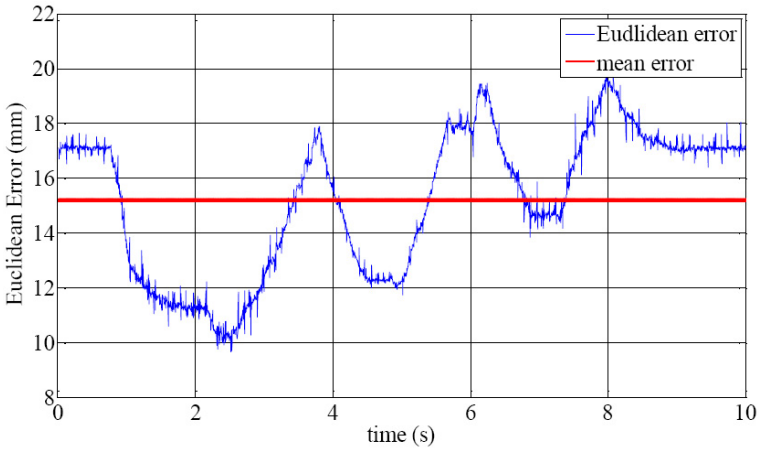

Figure 2.16: Euclidian error of the trajectory 1

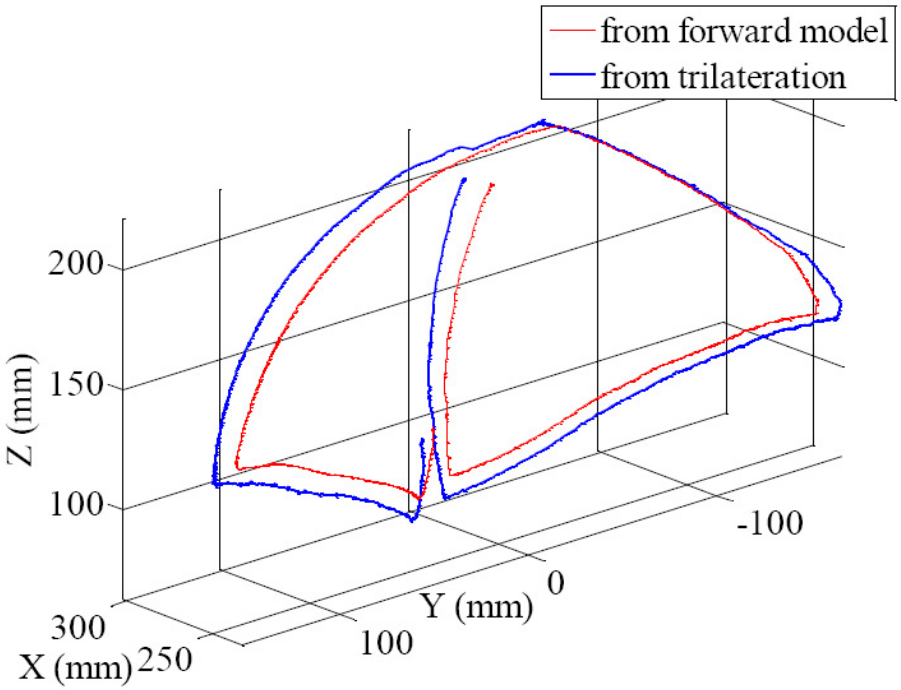

Figure 2.17: Trajectory 2: only the second bending section is moving

© 2014 Tous droits réservés.

doc.univ-lille1.fr

Thèse de Coralie Escande, Lille 1, 2013

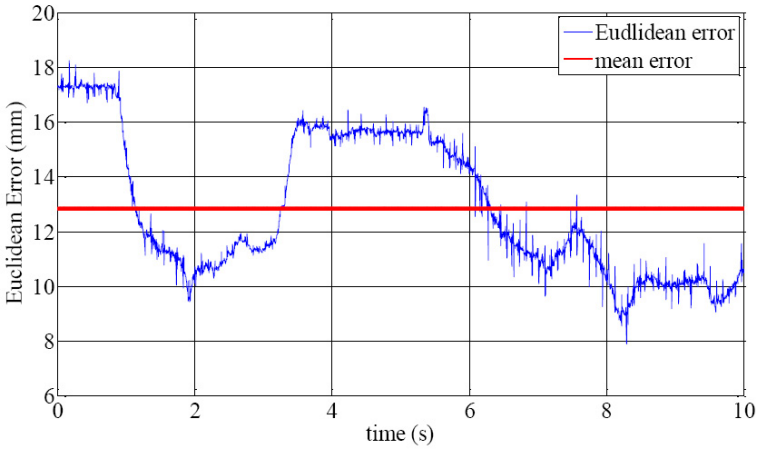

Figure 2.18: Euclidian error of the trajectory 2

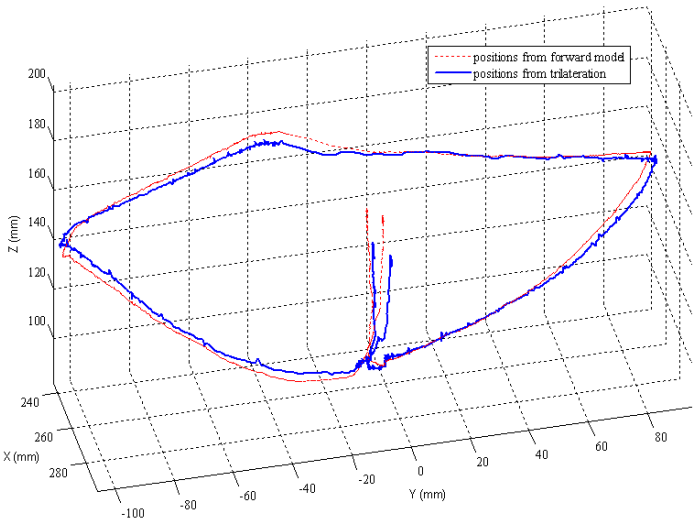

Figure 2.19: Trajectory 3: both bending sections are moving

© 2014 Tous droits réservés.

doc.univ-lille1.fr

Thèse de Coralie Escande, Lille 1, 2013

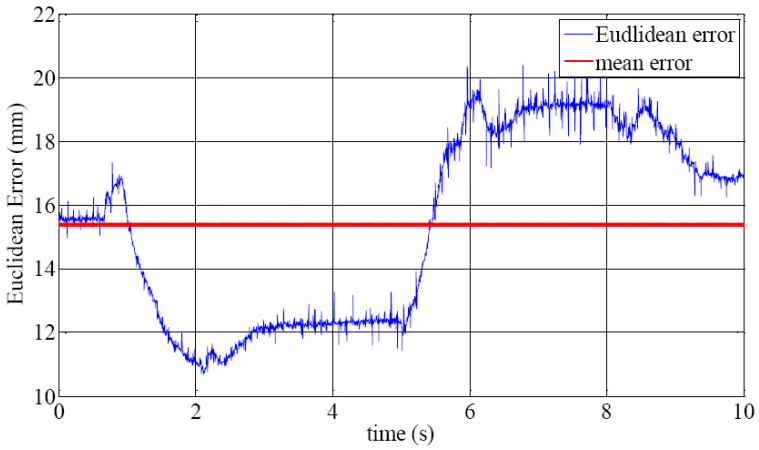

Figure 2.20: Euclidean error of trajectory 3

control. Finally, the inaccurate placement of the wire-potentiometers at a specific height generates other parameter uncertainties. Thus, all uncertainties (parameter and measurement) on the different components of the test bench can explain the error between the adapted trilateration and the FKM calculations.

It is worth noting that the trilateration technique used in this experimental validation is completely different from that used for the navigation of mobile robots. Indeed, trilateration is a technique for position estimation from range measurements which is often used in robot navigation. Mobile robots use a variety of sensors (such as cameras, sonar sensors,...) to obtain ranges or angles (or both), for landmarking and then use trilateration or triangulation to obtain a position estimation. In this case, optimizing trilateration is a fundamental issue to enhance the robot position estimation. In our study, the CBHA is fixed and trilateration is done using wired potentiometers (direct measure), thus error sources are considerably reduced when the position of external potentiometers is well identified and accurate from one potentiometer to another according to the CBHA Frame. If they are not well positioned, it affects considerably the performance of the validation results.

In addition, the CBHA is a complex system affected by the bending behavior of its structure and the shape memory effect. Compared to commercial robots, the more accurate continuum flexible robots are characterized by non-rigid structures; the CBHA is more of a hyper-redundant robot with a concatenation of multiple platforms (vertebra or backbones). This hyper-redundancy is controlled by only six inputs, which gives to the CBHA the property of an under-actuated system.

The phenomenon of shape memory can be observed, particularly when the CBHA stays in a distorted posture for a long time, then it takes time to go back to the initial posture. This disturbing case is not considered in the FKM but it

© 2014 Tous droits réservés.

doc.univ-lille1.fr

Thèse de Coralie Escande, Lille 1, 2013

can explain also the non-superposition of the starting points of the trilateration and the FKM. The origin of this phenomenon stems from: the strength of the material, the friction between backbones, and the hysteresis effect in the valves.

The advantage of this test bench is its low cost but its inconvenient is some inacuracies due to the aforementioned uncertainties. Moreover, the orientation of the CBHA tip can not be measured using this test bench and a diagnostic to isolate the different sources of errors is not feasible on this test bench.

2.7 Conclusion of the Chapter

In this chapter, a FKM of the CBHA has been developed, based on geometric approach for modeling continuum robots. Experimental tests have been conducted by comparing the numerical FKM results with those of the trilateration techniques. The results of this experiment permitted the validation of the FKM of the CBHA.

The generated trajectories of the CBHA tip have been reproduced through the numerical model with an exact profile reconstruction in presence of a convergence error. This latter is issued from the presence of multiple uncertainties (parameter and modeling), where some of them are identified and estimated using the kinematic calibration (level 2) developed in the next chapter.

This chapter presented also level 1 calibration, corresponding to the relationship between the signal provided by the length sensors and their real displacements.

© 2014 Tous droits réservés.

doc.univ-lille1.fr

Thèse de Coralie Escande, Lille 1, 2013

Chapter 3

Kinematic Calibration

The FKM developed in Chapter 2 is composed by a set of deterministic parameters and measured variables, regrouped through the following nonlinear relation (3.1).

$$\begin{pmatrix} x \\ y \\ z \\ \Phi \\ \Theta \\ \Psi \end{pmatrix} = f \begin{pmatrix} l_1 \\ l_2 \\ l_3 \\ l_4 \\ l_5 \\ l_6 \end{pmatrix} \tag{3.1}$$

The determination of these deterministic parameters is crucial for the model validation and its convergence. For this reason, the calibration of the model is needed to improve the model accuracy. This is done after kinematic uncertainties identification and estimation using an appropriate experimental test bench, to determine the coordinates of the CBHA tip with more accuracy.

3.1 Calibration Technique

There usually exists inaccuracies in the kinematic model identification of a manipulator robot arising from two types of uncertainties (Majarena et al. 2010) : kinematic and non-kinematic uncertainties. The kinematic uncertainties are due to imprecise knowledge of the robot kinematics, and the non-kinematic uncertainties arises from the robot element compliances, thermal deformations, wear of parts, frictions between elements, dimensional drifts and tolerances, and component replacement effects. These uncertainties subsequently affect the accuracy of the kinematic model and the placement of the end-effector[19]. This is the reason

[19]CBHA tip or center of tool

© 2014 Tous droits réservés.

doc.univ-lille1.fr

Thèse de Coralie Escande, Lille 1, 2013

why a kinematic calibration is required, allowing the FKM to calculate a reliable and accurate placement.

Three levels of robot calibration can be identified (Hollerbach et al. 1996; Majarena et al. 2010; Mooring et al. 1991; Quinet et al. 2012; Roth et al. 1987):

- **Level** 1 of calibration is defined as "joint level" calibration. The aim is to define the accurate relationship between the signal provided by the real displacement and those indicated by the sensor. The joint sensors are defined as proprioceptive sensors since they measure the internal state of the robot. It should be not confused with the exteroceptive sensors which collect information about external environment (obstacle detection, distance measures, artificial vision, etc) (Khalil and Dombre 1999). In the case of the CBHA, the proprioceptive sensors (wire-potentiometers) have to be calibrated in order to convert the electric signal in a length quantity, as explained in the previous chapter.

- For the **level** 2, calibration is defined as the entire robot kinematic model calibration. At this level, the purpose of the calibration is to determine the basic kinematic of the robot as well as the correct joint-angle relationships. In the case of the CBHA, the constant parameters $\{h_1, \delta, h_2, d_1, d_2, p\}$ of the model, describing the robot dimensions have also to be calibrated using the method described in this chapter and the results of this calibration are presented after the test bench description.

- Finally, in **level** 3, the calibration is defined as "non-kinematic", where it is taking in account the non-kinematic uncertainties. In the case of the CBHA, this level of calibration can take in account some dynamic aspects which are important for the control algorithm such as nonlinearities of hysteresis phenomenon on the pressure valves, deformations and non-neglected weights.

The calibration literature contains a variety of metrology systems, which can be classified based on the number of measured pose components (position and orientation) : partial when only position is measured (3 DoF) or complete when position and orientation are measured (6 DoF).

Generally, there exist three types of kinematic calibration methods for robots (Majarena et al. 2010). The first type, named external calibration, uses an external device, i.e., laser tracker, optical system, and coordinate measuring machine, to acquire the information of robot end-effector pose or joint parameters. The second type, called constrained calibration, depends on a physical constraint using additional mechanical system during the calibration process. The third type, namely self-calibration, utilizes the internal sensors to implement the measuring process, i.e an embedded camera.

© 2014 Tous droits réservés.

doc.univ-lille1.fr

Thèse de Coralie Escande, Lille 1, 2013

The importance of the calibration procedure resides in the fact that it can be used to enhance the robot accuracy through software rather than changing the mechanical structure or design of the robot. This importance is naturally reflected in the amount of research activities devoted to the topic of robot calibration (Hollerbach et al. 1996; Mooring et al. 1991; Roth et al. 1987; Zhuang and Roth 1995) . It has been studied for various robotic architectures : serial robots (In-Chul 2008; Meggiolaro et al. 2002) and parallel robots (Hernandez-Martinez et al. 2010; Zhuang 1997), using measurement systems and optimization method (Mooring et al. 1991).

3.2 Calibration Problem Statement

The aforementioned definition of kinematic calibration (level 2) assumes that a nominal kinematic model is known, but that this relationship is not necessarily accurate. For the considered CBHA, the nominal relationship is defined by the relation (3.2), where $\mathbf{\Pi}$ represents the vector of the model parameters $\{h_1, \delta, h_2, d_1, d_2, p\}$ and $l_{i=1..6}$ the tube lengths. The general principle of calibration methods is to identify the values of $\mathbf{\Pi}$ parameters leading to the best kinematic behavior of the CBHA in terms of pose accuracy. The nominal pose of the end-effector of the CBHA, with respect to the fixed reference Frame $\{\mathbf{x}_{\text{origin}}, \mathbf{y}_{\text{origin}}, \mathbf{z}_{\text{origin}}\}$, can be deduced from the nominal expression of ${}^{\text{origin}}_{4}\mathbf{T}$ and can be written as in equation (3.3). This nominal pose can be differentiated from the measured pose expressed in equation (3.4).

$$ {}^{\text{origin}}_{4}\mathbf{T} = f(\mathbf{\Pi}, l_i) \tag{3.2} $$

$$ \text{Pose}_{\text{nominal}} = \{x, y, z, \Phi, \Theta, \Psi\} \tag{3.3} $$

$$ \text{Pose}_{\text{measured}} = \{x', y', z', \Phi', \Theta', \Psi'\} \tag{3.4} $$

In the literature, the cost function of the pose error of the end-effector is expressed for the l^{th} robot posture with the relation (3.5), where the position error and the orientation error are defined using the Euclidean distance as in expressions (3.6) and (3.7), and where the coefficient η represents a weighting coefficient[20] that allows:

- To make homogenous the quantities appearing in the expression of the cost function since it has the dimension of a distance;

[20]For the experimental calibration, the coefficient η is equal to 10.

© 2014 Tous droits réservés.

doc.univ-lille1.fr

Thèse de Coralie Escande, Lille 1, 2013

- To allocate more importance or less to the contribution of orientation errors.

$$E_l = E_{\text{xyz}} + \eta E_{\Phi\Theta\Psi} \tag{3.5}$$

$$E_{\text{xyz}} = \sqrt{(x - x')^2 + (y - y')^2 + (z - z')^2} \tag{3.6}$$

$$E_{\Phi\Theta\Psi} = \sqrt{(\Phi - \Phi')^2 + (\Theta - \Theta')^2 + (\Psi - \Psi')^2} \tag{3.7}$$

For the case of the CBHA, the orientation of the pose (i.e. the CBHA tip) is not available from the existing embedded sensors. Thus, a physical concatenation of the CBHA and external industrial rigid-link manipulator robot has been realized (see Figure 3.1), in order to get the instantaneous indirect measurements of the orientation of the tip Frame. This external manipulator robot allows the measurement of its own end-effector pose, in terms of position and orientations. Thus, it is used as an external sensors for measurement of the orientations of the CBHA. This is possible when the Frames of the CBHA tip and those of the manipulator end-effector are superposed.

In this configuration, the error $E_{\Phi\Theta\Psi}$ described in equation (3.7) can not be directly calculated because the respective orientation of the Frame $\{\mathbf{x}_{\text{manipulator}}, \mathbf{y}_{\text{manipulator}}, \mathbf{z}_{\text{manipulator}}\}$ relative to the Frame $\{\mathbf{x}_{\text{CBHA}}, \mathbf{y}_{\text{CBHA}}, \mathbf{z}_{\text{CBHA}}\}$ is not well-known. However this relative orientation is expected to be constant due to the rigid link between the CBHA and the industrial manipulator shown in Figure 3.1. Thus the constraint of equation (3.8) can be used in the calibration, where $\mathbf{R}^{-1}_{\text{manipulator}}$ is the inverse rotation matrix of the industrial manipulator, $\mathbf{R}_{\text{CBHA}}$ is the rotation matrix of the CBHA, and $\mathbf{R}_{\text{cst}}$ is the matrix resulting from this product and is expected to be constant in the ideal case.

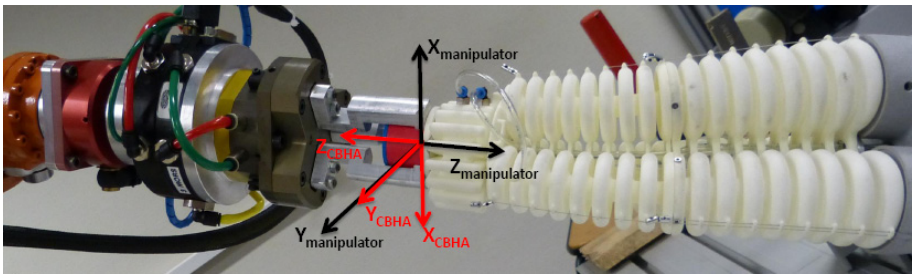

Figure 3.1: Zoom on the link between the industrial manipulator and the CBHA.

$$\mathbf{R}^{-1}_{\text{manipulator}}\mathbf{R}_{\text{CBHA}} = \mathbf{R}_{\text{cst}} \tag{3.8}$$

© 2014 Tous droits réservés.

doc.univ-lille1.fr

Thèse de Coralie Escande, Lille 1, 2013

The direction cosine vectors of this matrix can be used to calculate the corresponding angles $\{\Phi_{\mathbf{R}_{\text{cst}}}, \Theta_{\mathbf{R}_{\text{cst}}}, \Psi_{\mathbf{R}_{\text{cst}}}\}$ with ZYX convention. To minimize the variability of the matrix $\mathbf{R}_{\text{cst}}$, an error $E_{\mathbf{R}_{\text{cst}}}$ on the relative orientation is calculated in equation (3.9), where the variables $\{\overline{\Phi_{\mathbf{R}_{\text{cst}}}}, \overline{\Theta_{\mathbf{R}_{\text{cst}}}}, \overline{\Psi_{\mathbf{R}_{\text{cst}}}}\}$ are respectively the average values of $\{\Phi_{\mathbf{R}_{\text{cst}}}, \Theta_{\mathbf{R}_{\text{cst}}}, \Psi_{\mathbf{R}_{\text{cst}}}\}$.

$$E_{\mathbf{R}_{\text{cst}}} = \sqrt{(\Phi_{\mathbf{R}_{\text{cst}}} - \overline{\Phi_{\mathbf{R}_{\text{cst}}}})^2 + (\Theta_{\mathbf{R}_{\text{cst}}} - \overline{\Theta_{\mathbf{R}_{\text{cst}}}})^2 + (\Psi_{\mathbf{R}_{\text{cst}}} - \overline{\Psi_{\mathbf{R}_{\text{cst}}}})^2} \tag{3.9}$$

At this stage of calibration, where the pose errors are expressed, the following keeps the resolution of an optimization problem.

The cost function of the optimization problem is given through equation (3.10), which is minimized in order to find the best corrections on the parameters $\{h_1, \delta, h_2, d_1, d_2, p\}$. The errors E_{xyz} and $E_{\mathbf{R}_{\text{cst}}}$ are normalized. In summary, the calibration optimizes the parameters $\{h_1, \delta, h_2, d_1, d_2, p\}$ using the 6 measurements of the manipulator pose $\{x_{\text{manipulator}}, y_{\text{manipulator}}, z_{\text{manipulator}}, \Phi_{\text{manipulator}}, \Theta_{\text{manipulator}}, \Psi_{\text{manipulator}}\}$.

The multivariate nonlinear and constrained[21] optimization problem of equation (3.11) should be solved, where n_{pos} represents the number of considered postures in the workspace. Furthermore, it is noted that the vector $\mathbf{\Pi}$ of the model parameters should be investigated within realistic bounds reflecting real technological constraints on the CBHA.

$$F_{\text{objective}} = \|E_{\text{xyz}}\| + \eta \|E_{\mathbf{R}_{\text{cst}}}\| \tag{3.10}$$

$$\begin{cases} \min\limits_{\mathbf{\Pi}} \sum\limits_{l=1}^{n_{\text{pos}}} F_{\text{objective}} \\ \mathbf{\Pi}_{\min} \leq \mathbf{\Pi} \leq \mathbf{\Pi}_{\max} \end{cases} \tag{3.11}$$

The process of minimizing the cost function is carried out using the deterministic optimization technique called the Sequential Quadratic Programming (SQP) method. It belongs to the most powerful nonlinear programming algorithms that is used nowadays, for solving nonlinear programming problems. The theoretical background of SQP is described in (Nocedal et al. 2006). The SQP method tries to solve the Karuch-Kuhn-Tucker (KKT) equations which are the necessary optimality conditions for a constrained nonlinear optimization problem (Barclay et al. 1997; Fletcher 1987; Powell 1984). Its excellent numerical performance was tested and compared with other methods in numerous references, e.g. (Schittkowski 2002). In (Schittkowski 1980), the author has implemented and tested a version that outperforms every other tested method in terms of efficiency, accuracy, and

[21] In this case, all of the constraints are inequalities.

© 2014 Tous droits réservés.

doc.univ-lille1.fr

Thèse de Coralie Escande, Lille 1, 2013

percentage of successful solutions, over a large number of test problems. The basic algorithm is then extended to solve also nonlinear least squares problems efficiently (Schittkowski 2002). The SQP methods allow to closely mimic Newton's method for constrained optimization just as is done for unconstrained optimization. At each major iteration of the SQP method, the objective function is approximated with a quadratic function and nonlinear constraints are linearized. In the same iteration, an approximation is made of the Hessian of the Lagrangian function using a quasi-Newton updating method. This is then used to generate a Quadratic Programming (QP) sub-problem, whose solution is used to form a search direction for a line search procedure. The SQP method is also coupled with a multi-start strategy in order to avoid the problem of local minima.

3.3 Experiment and Results

To examine kinematic performances and properties of the CBHA, it is important to have an accurate measurement of the robot kinematics. In this section we are going to describe an experimental setup used for measuring the real poses of the CBHA with high accuracy. For this purpose, an industrial manipulator has been coupled with the CBHA generating the movement. Thus, this test bench is a constrained level 2 calibration system. Such test bench allows obtaining accurate results which are much better and can be used to calibrate the constant parameters of the FKM of the CBHA.

3.3.1 Description of the Test Bench

In the presented work, a KUKA (KR6 Arc) manipulator robot, shown in Figure 3.2 is used to reach the desired trajectories by gripping the extremity of the CBHA. The programming language Kuka Robot Language (KRL) is used to create trajectories easily in an industrial environment. The programs are done through the Kuka System Software (KSS) which is running on VxWorks. The Input/Output (I/O) connections are used to communicate with the program, such as the serial connection RS232. Although VxWorks is a real-time operating system, the user can not influence the execution of a motion during the interpolation process.

For this case, another software package named Remote Sensor Interface (RSI) is installed. This package allows the user to control the robot in real-time, by influencing the robot motion via a correction during the path execution. The RSI-EthernetXML is considered to exchange data between the robot and a remote server using an Ethernet connection as shown in Figure 3.2. When the connection is established, the robot controller send messages every 12 ms (interpolation cycle) and the remote computer must answer in a given time. All the communication

© 2014 Tous droits réservés.

doc.univ-lille1.fr

Thèse de Coralie Escande, Lille 1, 2013

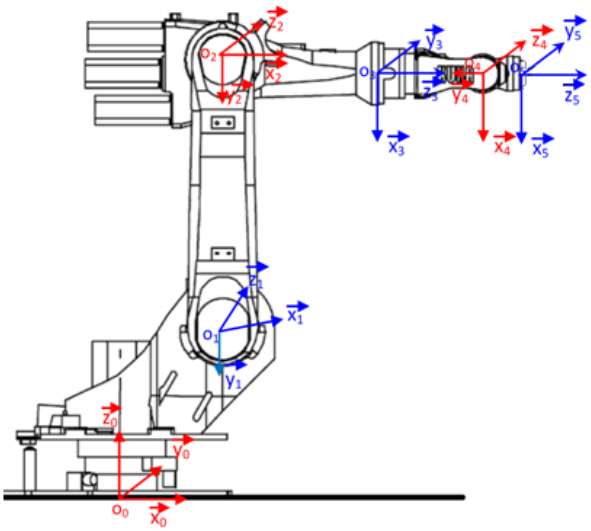

Figure 3.2: Overview of the industrial manipulator

packets are transmitted as eXtensible Markup Language (XML) strings, where it is possible to configure the content of these packets. In the default configuration, the robot sends its actual joint and Cartesian positions, while the remote computer sends joint angles or position corrections. Predefined objects in RSI software are used to send joints angles, position, current and torque of each joint actuator to the remote application for the supervision. The remote computer is running under a Debian squeeze GNU/Linux operating system with a real-time Xenomai kernel. It is important for such accurate robot operation to use a real-time kernel to ensure a robust execution of the task with respect to the timing. In the application of Figure 3.3, after a thread starts handling the communication with the robot, another part executes the acquisition algorithm. The thread communication opens a Transmission Control Protocol (TCP) connection with the robot and start parsing the received messages using the libXML2 package (XML C parser and toolkit of Gnome) recommended by KUKA. The real-time task is executed for data collection, used to validate the FKM of the CBHA in off-line mode.

From the CBHA side, a DSpace I/O board linked to an external PC is used to receive the measurements of the potentiometers and to send a trigger signal to the industrial manipulator for the synchronization of the starting time. The DSpace control board contains a PowerPC 750GX running at 1 GHz for rapid control prototyping with an application memory of 32 MB. For programing, the toolbox Real-Time Interface (RTI) for DSpace in MatLab/Simulink is used. The monitoring software ControlDesk permits to set manually the trigger signal and

© 2014 Tous droits réservés.

doc.univ-lille1.fr

Thèse de Coralie Escande, Lille 1, 2013

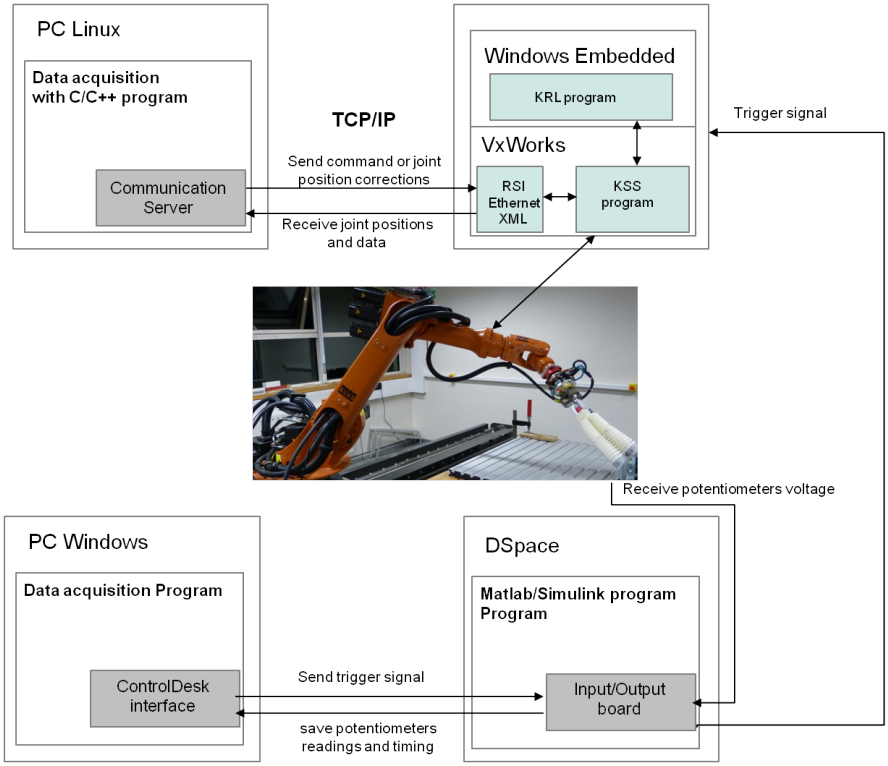

Figure 3.3: Overview of the calibration experiment architecture

© 2014 Tous droits réservés.

doc.univ-lille1.fr

Thèse de Coralie Escande, Lille 1, 2013

to show the plotted potentiometers signals.

This experiment allows validating the FKM in terms of positions and orientations. Indeed, the industrial manipulator gives instantaneously the orientations $\{\Phi_{\text{manipulator}}, \Theta_{\text{manipulator}}, \Psi_{\text{manipulator}}\}$ while the FKM calculates the tip Frame orientations of the CBHA $\{\Phi_{\text{CBHA}}, \Theta_{\text{CBHA}}, \Psi_{\text{CBHA}}\}$.

The accuracy of the industrial manipulator of Figure 3.4 allows calibrating the constant parameters of the FKM. This calibration is useful because the first experimental validation, using the trilateration test bench presented in the previous chapter, has shown that the model is sensitive to varying parameters combinations.

Because of the Basis Frame placement shown in Figure 3.4, two additional Frame transformations are also added : one before (${}^{\text{basis}}_{\text{origin}}\mathbf{T}$) and one after (${}^{4}_{\text{kuka}}\mathbf{T}$) the CBHA transformation ${}^{\text{origin}}_{4}\mathbf{T}$. The final transformation is shown in (3.12), where ${}^{4}_{\text{kuka}}\mathbf{T}$ is expressed in equation (3.13), and ${}^{\text{basis}}_{\text{origin}}\mathbf{T}$ is expressed in equation (3.14), and where x_{a} and y_{a} are distances (in mm), β and α are angles (in rad) shown in Figure 3.4. These parameters $\{x_{\text{a}}, y_{\text{a}}, \alpha, \beta\}$ are also included in the parameters calibration.

$$ {}^{\text{basis}}_{\text{kuka}}\mathbf{T} = {}^{\text{basis}}_{\text{origin}}\mathbf{T}\, {}^{\text{origin}}_{4}\mathbf{T}\, {}^{4}_{\text{kuka}}\mathbf{T} \tag{3.12} $$

$$ {}^{4}_{\text{kuka}}\mathbf{T} = \begin{bmatrix} -1 & 0 & 0 & 0 \\ 0 & 1 & 0 & 0 \\ 0 & 0 & -1 & 0 \\ 0 & 0 & 0 & 1 \end{bmatrix} \tag{3.13} $$

$$ {}^{\text{base}}_{\text{origin}}\mathbf{T} = \begin{bmatrix} \cos\alpha & -\sin\alpha & 0 & x_{\text{a}} \\ \sin\alpha & \cos\alpha & 0 & y_{\text{a}} \\ 0 & 0 & 1 & 0 \\ 0 & 0 & 0 & 1 \end{bmatrix} \begin{bmatrix} \cos\beta & 0 & \sin\beta & 0 \\ 0 & 1 & 0 & 0 \\ -\sin\beta & 0 & \cos\beta & 0 \\ 0 & 0 & 0 & 1 \end{bmatrix} \tag{3.14} $$

3.3.2 Results

Table 3.1 shows the constant parameters values obtained before and after calibration, and the absolute error. Figure 3.5 illustrates the positions of the trajectory executed by the industrial manipulator, while Figure 3.6 presents the euclidean error of positions. Finally, Figure 3.7 provides the Euler angles and Figure 3.8 mentions the corresponding errors.

3.3.3 Discussion

First, the results shown in Figures 3.5 and 3.6 point out a better accuracy of the model in terms of positions thanks to the parameters calibration. The average

© 2014 Tous droits réservés.

doc.univ-lille1.fr

Thèse de Coralie Escande, Lille 1, 2013

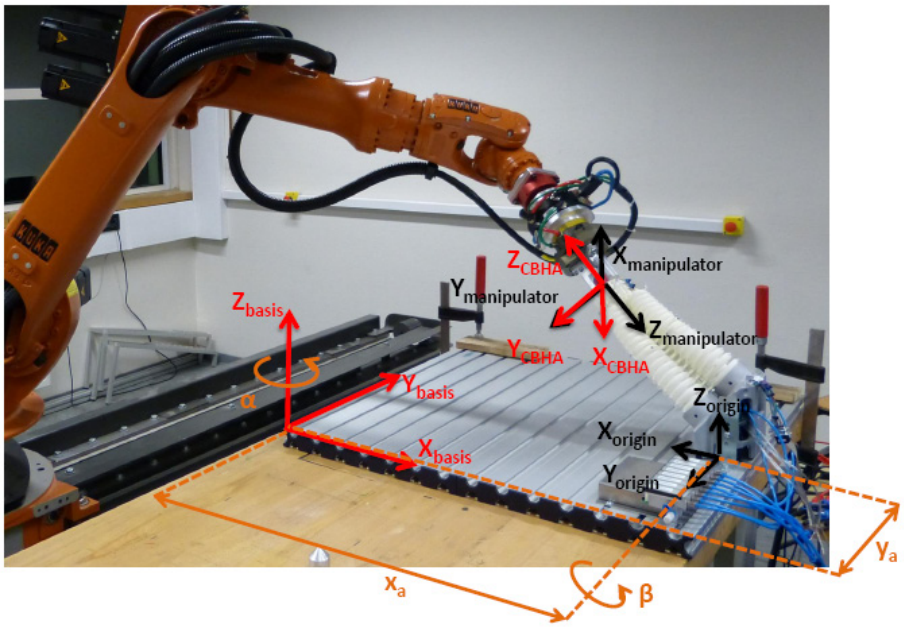

Figure 3.4: Overview of the position of the Frames

Table 3.1: Calibrated constant parameters

Parameter	Initial Value	Calibrated Value	Absolute Error
x_a (mm)	652.93	648.93	4
y_a (mm)	350	346	4
α (rad)	3.1416	3.1669	0.0253
β (rad)	0.0349	0.0698	0.0349
h_1 (mm)	73.99	71.99	2
δ (rad)	0.8727	0.8628	0.0099
h_2 (mm)	22.13	26.13	4
d_1 (mm)	63.5085	58.2987	5.2098
d_2 (mm)	52.8275	56.1374	3.3099
p (mm)	55	56.3228	1.3228

© 2014 Tous droits réservés.

doc.univ-lille1.fr

Thèse de Coralie Escande, Lille 1, 2013

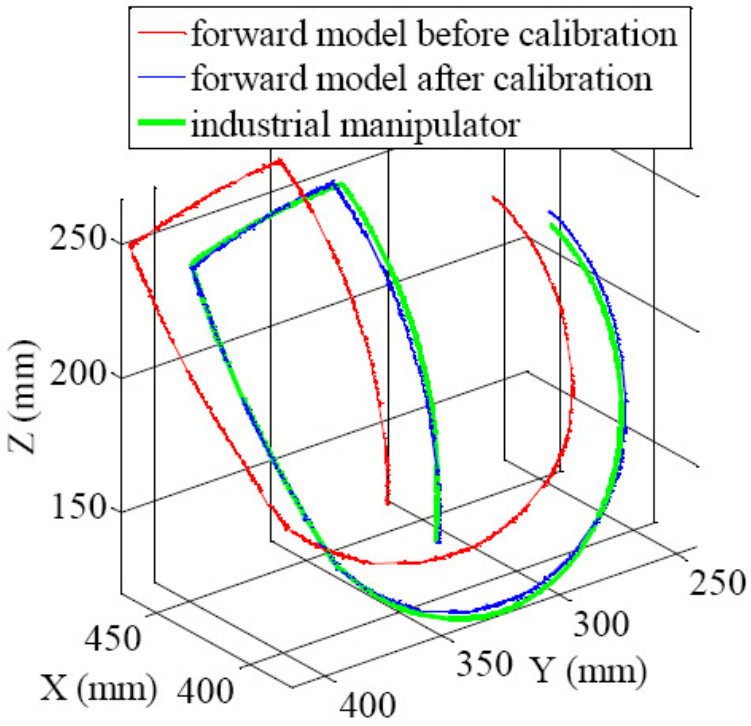

Figure 3.5: 3D Trajectories of measured and estimated positions

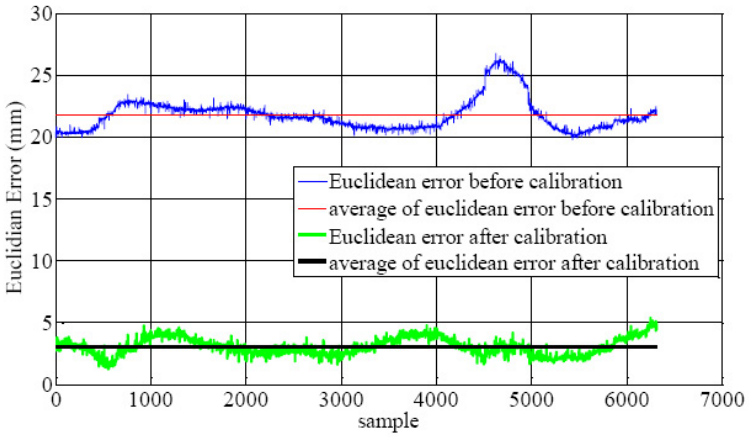

Figure 3.6: Euclidean error of the trajectory executed with industrial manipulator

© 2014 Tous droits réservés.

doc.univ-lille1.fr

Thèse de Coralie Escande, Lille 1, 2013

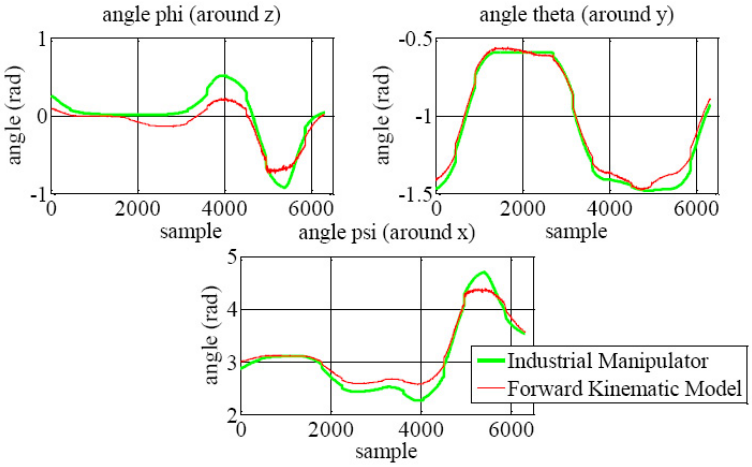

Figure 3.7: Euler angle of the trajectory executed with industrial manipulator

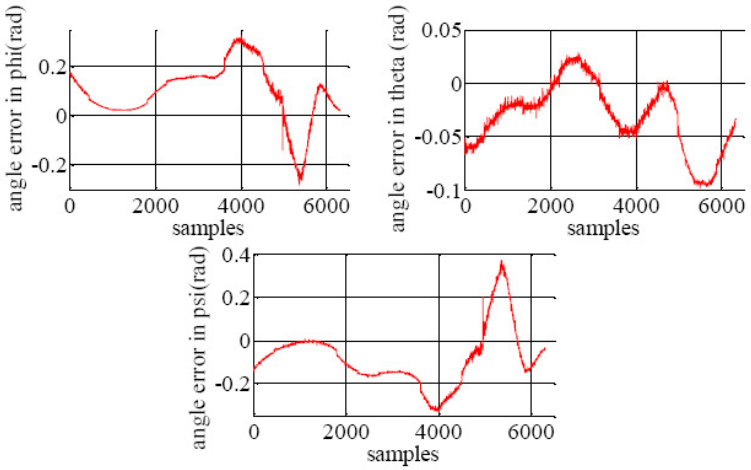

Figure 3.8: Error on the Euler angle of the trajectory executed with industrial manipulator

© 2014 Tous droits réservés.

doc.univ-lille1.fr

Thèse de Coralie Escande, Lille 1, 2013

of the Euclidian error is about 3 mm, which represents less than 1 % of the total length of the CBHA. This has been possible thanks to the calibrated value of the constant parameters given in Table 3.1, where it is noticed that the parameters x_a, y_a, h_1, and h_2 have reached saturation.

Secondly, the Figures 3.7 and 3.8 show that the estimated orientation follows the measured orientation with presence of some uncertainties[22] and validates the orientation modeling.

When the industrial manipulator generates and imposes a trajectory to the CBHA, a constraint is imposed to the latter and errors in orientation are induced from the flexible posture of the CBHA, originally due to the type of the CBHA constitutive material. This aspect can be seen as a non-geometric phenomenon inducing an uncertainty which can not be corrected by a level-2 calibration. However this problem will not appear in the real case because the mobile bionic robot RobotinoXT has to move autonomously and it is not supposed to be guided by an external robot manipulator. Moreover, in the calculation of the orientations $\{\Phi, \Theta, \Psi\}$ of the CBHA, expressed in equations (2.28), (2.30) and (2.32), it is noticed that the calculation of the orientations Θ and Ψ are depending on that of the orientation Φ. Finally, the industrial manipulator can not cover all of the workspace of the CBHA because of kinematic movement constraints.

Moreover, there is a dependency between the tubes lengths l_i as shown in equation (2.16). This dependency can be observed on the mechanical structure of the CBHA, where each backbones are linked together on the middle of the CBHA. This fact reduces then the number of degrees of freedom to 4 per section.

In addition, the modeling assumptions of constant curvature and of constant section diameter are also sources of errors because they are only approximations, according to the small size of the CBHA.

3.4 Conclusion of the Chapter

In this chapter, the calibration of the CBHA kinematic model is developed for the level 2. In order to improve the accuracy of the model, a level 2 calibration of the geometric parameters has been done, using optimization method by minimizing the errors between the results of the numerical model and of the experiment, issued from the association with the industrial robot. The constant parameters $\{h_1, \delta, h_2, d_1, d_2, p\}$ of the FKM describing the robot dimensions have been optimized. The accuracy obtained after this level 2 calibration has been improved from the level 1 calibration in terms of positions and orientations. The use of an external manipulator robot helps in estimating the orientations of the CBHA tip Frame instantly.

[22] including the industrial robot accuracy uncertainty

© 2014 Tous droits réservés.

doc.univ-lille1.fr

Thèse de Coralie Escande, Lille 1, 2013

© 2014 Tous droits réservés.

doc.univ-lille1.fr

Thèse de Coralie Escande, Lille 1, 2013

Chapter 4

Inverse Kinematic Modeling

In the context of robotic manipulation, the Inverse Kinematic Model (IKM) calculates the joint coordinates from the Cartesian coordinates of the tool's center placed on the end-effector. The IKM is an inverse function of the Forward Kinematic Model (FKM); these two models are non linear in most cases. According to the redundancy of the robot model, several solutions related to inverse kinematic issue exist:

- No solution: Target point is outside the workspace or inaccessible;
- Unique Solution: Point target reachable in one way;
- Multiple Solutions: Joint coordinates are calculated without ambiguity (Case of redundant robots);
- Infinite Solutions: Infinite number of joint coordinates allow reaching a target point (Case of hyper-redundant robots).

In the case of the CBHA, the (FKM) models the Cartesian coordinates of the gripper's center in function of the six tubes lengths by using the (FKM) of one bending section depending on its three tubes lengths. The CBHA being composed of 2 sections, it is needed to be able to control the pose of the second bending section's tip by varying the six tubes lengths. In this chapter, the goal is to calculate the IKM of the CBHA, i.e. to calculate the relation between the position of the second bending section's tip and the six tubes lengths. It is worth noting that the orientation is not available. The model equations system being highly non-linear and under-determined, the IKM calculation is very complex and gives an infinite number of solutions. Moreover, the workspace needs to be determined in order to be sure that the desired target position is reachable. Thus this chapter presents first the workspace identification before the IKM of the CBHA.

© 2014 Tous droits réservés.

doc.univ-lille1.fr

Thèse de Coralie Escande, Lille 1, 2013

4.1 Workspace

In this section, the identification of the CBHA workspace is studied based on the forward kinematic model of the CBHA and on its physical constraints. The workspace is then illustrated by simulated and experimental results. The workspace of a manipulator arm is the space of reachable positions by the tip of the arm. The knowledge of the workspace allows identifying the desired position from a set of reachable positions.

4.1.1 Workspace Identification

The exact determination of the workspace can be done in the case of the CBHA, using two different ways. On one hand, from the forward kinematic model presented in the previous chapters 1 and 2, by simulating the variation of the tube lengths through the identification process illustrated by the Figure 4.1. On the other hand through an experiment by measuring tube lengths for a pressure input variations. This workspace is limited by the following constraints:

1. The length of each tube is bounded;

2. The total length of CBHA is bounded.

3. If one tube length has an extremal value, then the two other tubes have the same length.

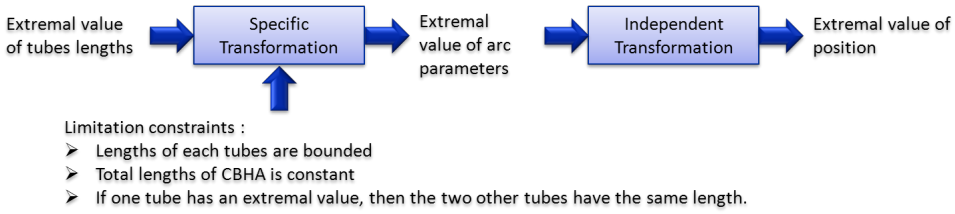

Figure 4.1: Workspace identification process

The identification begins by studying the effects of these limitations on arc parameters of the configuration space of the CBHA. Indeed, the arc parameters described in chapter 2 depend on the lengths of the tubes, as given by the following equations:

© 2014 Tous droits réservés.

doc.univ-lille1.fr

Thèse de Coralie Escande, Lille 1, 2013

$$\begin{cases} L_j = \frac{l_i+l_{i+1}+l_{i+2}}{3} \\ \phi_j = \tan^{-1}\left(\frac{\sqrt{3}(l_{i+2}-l_{i+1})}{2l_i-l_{i+1}-l_{i+2}}\right) \\ r_j = \frac{(l_i+l_{i+1}+l_{i+2})}{D_j} d_j \\ \theta_j = \frac{D_j}{3d_j} \\ D_j = 2\sqrt{{l_i}^2+{l_{i+1}}^2+{l_{i+2}}^2-l_il_{i+1}-l_il_{i+2}-l_{i+1}l_{i+2}} \end{cases} \tag{4.1}$$

,with j the section number, i the tube number, and where: $i = 1$ for $j = 1$ and $i = 4$ for $j = 2$. These equations are studied for the minimum and maximum values of each tube: $l_{i,\min}, l_{i+1,\min}, l_{i+2,\min}$ and $l_{i,\max}, l_{i+1,\max}, l_{i+2,\max}$.

The CBHA is designed symmetrically, where the minimum and maximum values of the tubes of the same section j are unique and noted $l_{j,\min}$ and $l_{j,\max}$. Note that the total length of the tube is constant.

It is observed that if one of the tubes of a same section has an extremal length value, then the other two tubes have a same lengths, which is different from the extremal value of the first tube, and which is noted $l_e \neq l_{j,\max} \neq l_{j,\min}$:

Table 4.1: Extremal posture for a CBHA's section

$l_i = l_{j,max}$	$\Rightarrow$	$l_{i+1} = l_{i+2} = l_e$	
$l_{i+1} = l_{j,max}$	$\Rightarrow$	$l_i = l_{i+2} = l_e$	$\Rightarrow$ first local extrema
$l_{i+2} = l_{j,max}$	$\Rightarrow$	$l_i = l_{i+1} = l_e$	
$l_i = l_{j,min}$	$\Rightarrow$	$l_{i+1} = l_{i+2} = l_e$	
$l_{i+1} = l_{j,min}$	$\Rightarrow$	$l_i = l_{i+2} = l_e$	$\Rightarrow$ second local extrema
$l_{i+2} = l_{j,min}$	$\Rightarrow$	$l_i = l_{i+1} = l_e$	

Substituting the values of Table 4.1 into the equations (4.1) for each possible position, the maximal and minimal values of the arc parameters may be identified as follows:

$$L = L_1 + L_2 = 205\,\text{mm} \tag{4.2}$$

$$\phi_{j,\min} = \frac{-\pi}{2} \tag{4.3}$$

$$\phi_{j,\max} = \frac{\pi}{2} \tag{4.4}$$

$$D_{j,\min} = 0 \tag{4.5}$$

© 2014 Tous droits réservés.

doc.univ-lille1.fr

Thèse de Coralie Escande, Lille 1, 2013

$$r_{j,\max} = \text{not defined} \tag{4.6}$$

$$\theta_{j,\min} = 0 \tag{4.7}$$

A first local extrema can be calculated, when one of the tubes length is maximum, as follows:

$$D_{j,\max} = 3 \left\| l_{j,\max} - l_e \right\| \tag{4.8}$$

$$r_{j,\min} = \frac{3\ L_j d_j}{D_{j,\max}} \tag{4.9}$$

$$\theta_{j,\max} = \frac{D_{j,\max}}{3\ d_j} \tag{4.10}$$

A second local extrema can be calculated, when one of the tubes length is minimum, as follows:

$$D2_{j,\max} = 3 \left\| l_{j,\min} - l_e \right\| \tag{4.11}$$

$$r2_{j,\min} = \frac{3\ L_j d_j}{D2_{j,\max}} \tag{4.12}$$

$$\theta 2_{j,\max} = \frac{D2_{j,\max}}{3\ d_j} \tag{4.13}$$

4.1.2 Obtained Results

Figures 4.2 show the area of experimental work of the CBHA, figures 4.3 below show the simulated workspace of the CBHA. Each workspace figure is shown with different points of view: a 3D representation and the three plane views.

© 2014 Tous droits réservés.

doc.univ-lille1.fr

Thèse de Coralie Escande, Lille 1, 2013

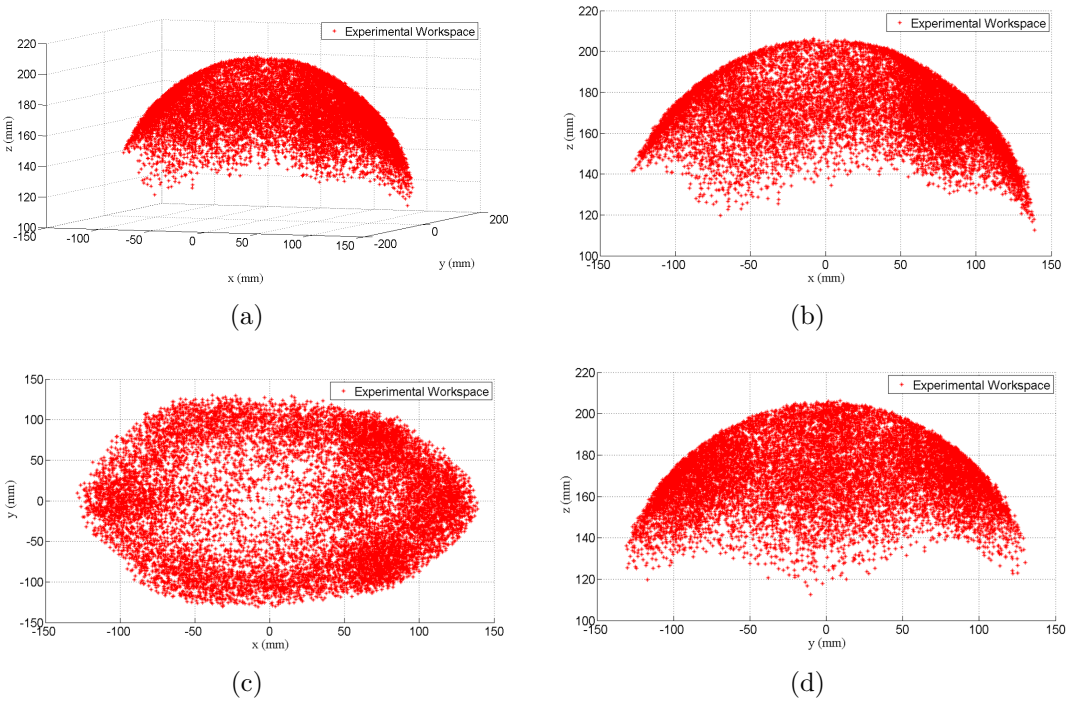

Figure 4.2: Several points of view of the experimental workspace of CBHA: (a) 3D view, (b) view of the plane XZ, (c) view of the plane XY, (d) view of the plane ZY

© 2014 Tous droits réservés.

doc.univ-lille1.fr

Thèse de Coralie Escande, Lille 1, 2013

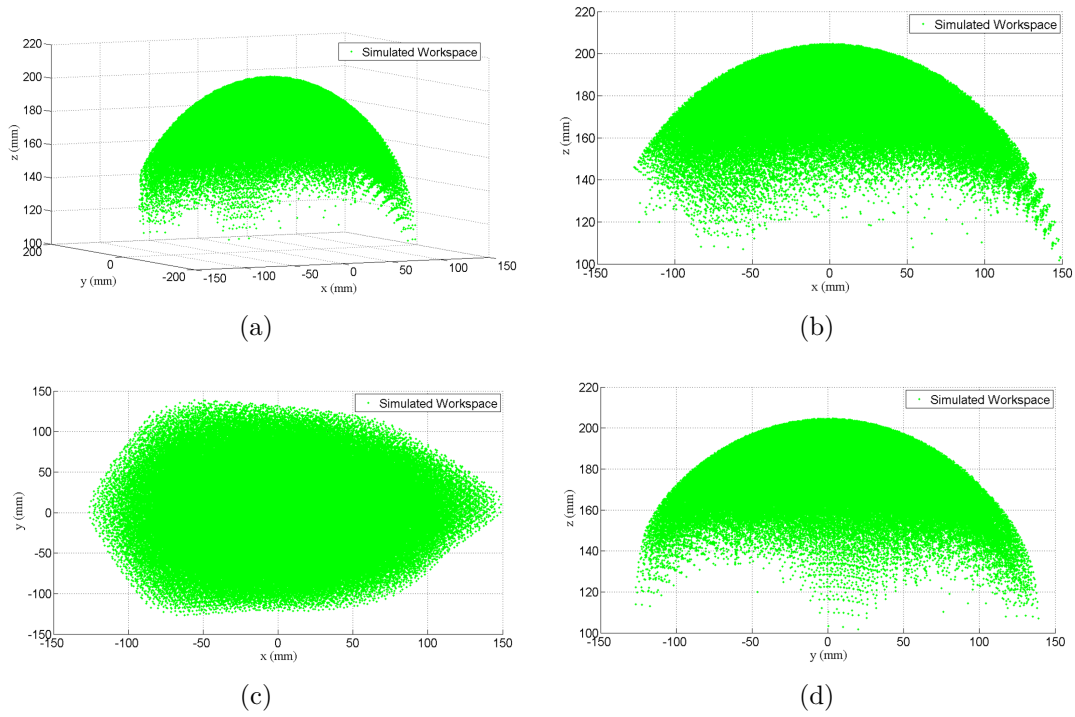

Figure 4.3: Several points of view of the experimental workspace of CBHA: (a) 3D view, (b) view of the plane XZ, (c) view of the plane XY, (d) view of the plane ZY

4.1.3 Discussion

The global form of the simulated workspace is similar to those obtained with the experimental data. The plotted positions are not exactly the same, because the simulated workspace is obtained by varying the tubes lengths as input of the FKM with physical constraints[23], while the experimental workspace is obtained by varying the tubes pressures. It is noticed that the experimental workspace is smaller than the simulated workspace. It is due to the fact that the input pressure is limited to 2 bar[24].

[23] extremal values of tubes lengths, bending sections lengths and arc parameters

[24] If more pressure would be available, then the simulated workspace and the experimental workspace would have the same size.

© 2014 Tous droits réservés.

doc.univ-lille1.fr

Thèse de Coralie Escande, Lille 1, 2013

4.2 Global Modeling Method for the IKM

Thus, this chapter propose an alternative method for the IKM calculation, based on the modeling of hyper-redundant robots, and more exactly of serial-parallel robots (hybrid robots), which traduce the CBHA's backbone composed of 17 concatenated vertebrae. Indeed, each inter-vertebrae is similar to a parallel system structure of 3 DoF, as shown in Figure 4.4, which means $3 \times 16 = 48$ DoF for the entire CBHA. It is the reason why the modeling assumptions of this chapter are different from those of the previous chapters. The effect of deeming a continuous robot to hybrid parallel robot was used to calculate the forward kinematics of Bionic Handling Assistant robot (BHA) (Mahl, Hildebrandt, et al. 2012). Modeling of parallel architectures has been addressed in several references (Chibani, Chettibi, et al. 2013; Chibani, Mahfoudi, et al. 2013; Ibrahim et al. 2007; Mintenbeck et al. 2010; Yu et al. 2010)

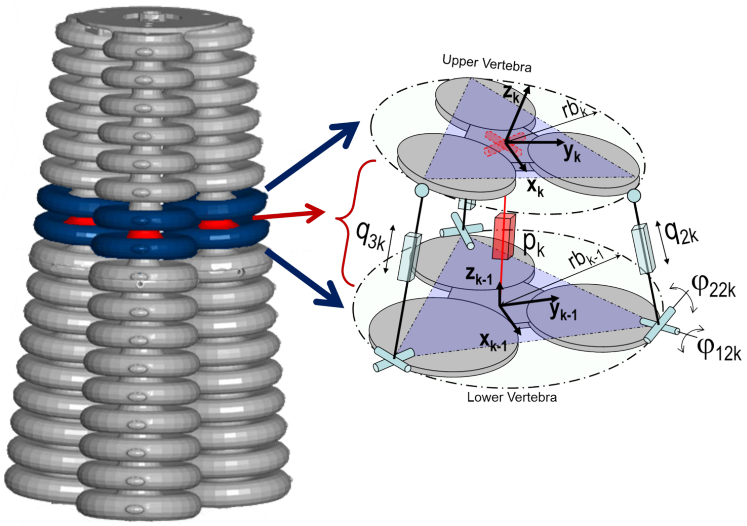

Figure 4.4: Achitecture of backbone represented by a parallel robot 3UPS-1UP

The IKM of the CBHA is done by combining two approaches:

1. Algebraic approach based on two different methods for determining the IKM of one CBHA's inter-vertebra:
   (a) The first method called Raghavan and Roth (Raghavan et al. 1990);
   (b) The second method based on the algebraic Chasles theorem, used to validate the unique solution of the inverse model of a vertebra;

© 2014 Tous droits réservés.

doc.univ-lille1.fr

Thèse de Coralie Escande, Lille 1, 2013

2. Numerical approach based on both iterative optimization method for CBHA's posture, and distribution of the vertebrae along its length.

The resulting IKM is compared with the experimental data and then used to simulate a set of points which represents the workspace.

4.2.1 Modeling Assumption

In this chapter, it is assumed that there is a uniform curvature throughout the CBHA's tubes, as if the CBHA were constituted of only one bending section. This assumption has been adopted in light of the following considerations :

- It simplifies the modeling.
- The trajectory generated by the industrial rigid manipulator and used to validate the model does not include different section curvatures

This assumption constrains the possible movements, reducing the attainable positions in a subspace of workspace.

Each inter-vertebra is modeled as a parallel robot so that the modeled bending section is modeled as a serial-parallel robot (hybrid robot), so that neither torsion nor longitudinal and lateral translations are possible.

The shape is not anymore assumed to be a cylinder, but the conical shape is taken in account by calculating the diameter of each vertebrae.

4.2.2 Determination of the Vertebra Radius

Before determining the model of each vertebra, it is necessary to determine the radius of the considered vertebra, knowing that the entire shape of the CBHA is conical.

For calculating the radius of each vertebra, that of the basis (rb_0) and the last vertebra (rb_{16}) are assumed known. Equation (4.14) is then deduced from Figure 4.5, with $L_k = \frac{k\ L}{N_{\text{module}}}$, where $k = 1..16$ is the number of inter-vertebrae, and N_{module} specifies the number of all inter-vertebrae, i.e. $N_{\text{module}} = 16$.

$$rb_k = L_k \frac{rb_1 - rb_{16}}{L} + rb_{16} \tag{4.14}$$

© 2014 Tous droits réservés.

doc.univ-lille1.fr

Thèse de Coralie Escande, Lille 1, 2013

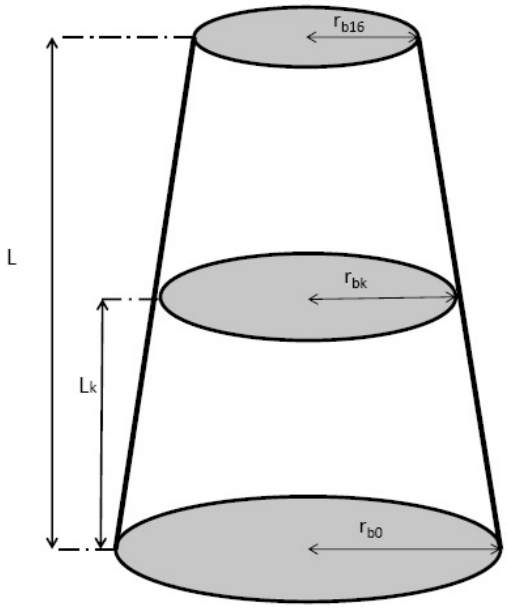

Figure 4.5: Determination of the vertebrae radius

Thus, the equation (4.15) is obtained.

$$\boxed{rb_k = \frac{k}{N_{module}}(rb_1 - rb_{16}) + rb_{16}} \tag{4.15}$$

4.3 Inter-vertebrae Inverse Kinematic Model

Among the parallel robots, there exist different types of structures: RPS, UPS, RPR ... characterized by their joints types: Universal (U), spherical (S), prismatic (P), and revolute (pivot) (R). CBHA's Inter-vertebrae are similar to a parallel 3UPS-1PU type robot, wherein each vertebra is represented by an equilateral triangle in a circumscribing circle with its corresponding diameter. Each kinematic serial UPS is represented by a succession of non-slip pivots and slides joints:

- Universal joint (U): 2 pivot joints;
- Prismatic joint (P): 1 prismatic active joint;
- Spherical joint (S): 3 pivot joints.

The PU's kinematic chain is represented by a succession of non-slip pivots and slides joints:

© 2014 Tous droits réservés.

doc.univ-lille1.fr

Thèse de Coralie Escande, Lille 1, 2013

- Prismatic joint (P): 1 prismatic passive joint;
- Universal joint (U): 2 pivot joints.

Three prismatic joints for the kinematic serial UPS located on the side are considered active and are used to control the position and orientation of the upper vertebra related to the lower vertebra, due to variable lengths q_{mk} of prismatic joint (P), with $m = 1, .., 3$ the number of prismatic active joints and $k = 1, .., 16$ the number of inter-vertebrae.

The prismatic joint of the kinematic serial PU, located in the center is considered passive and is used to constrain possible linear movements by the translations in longitudinal and lateral ways, so that the torsion around its main axis is constrained[25]. This serial PU allows thus making the torsional stress impossible as well as the longitudinal and lateral translations impossible.

4.3.1 Modeling of the Inter-vertebra Based on Raghavan and Roth Method

The method of Raghavan and Roth allows to determine the joint variables from a set of non linear equations, obtained through a closed kinematic chain. It can be applied to any type of robots with any type of shape. This process is based on the resolution called dialectic elimination (Salmon 1885).

4.3.1.1 Modeling the Open Kinematic Chain UPS

The method of D-H (Hartenberg et al. 1955) is used to determine the homogeneous transformation matrix of the UPS open kinematic chain. Figure 4.6 defines the different Frames according to the DH convention. Thus, z_{mnk} axes were placed on the joint axes and x_{mnk} axes are defined by the common perpendicular to the axis z_{mnk} and z_{mnk+1}, where $m = 1, .., 3$ is the number kinematic chain, $n = 1, .., 6$ the joint number and $k = 1, .., 16$ is the inter-vertebra number.

The D-H parameters enable, with the minimum number of parameters, the deduction of the homogeneous elementary transformation matrices defining a linked Frame to a body assumed to be perfectly rigid according to another body in a kinematic chain.

[25]There is no torsion on the CBHA

© 2014 Tous droits réservés.

doc.univ-lille1.fr

Thèse de Coralie Escande, Lille 1, 2013

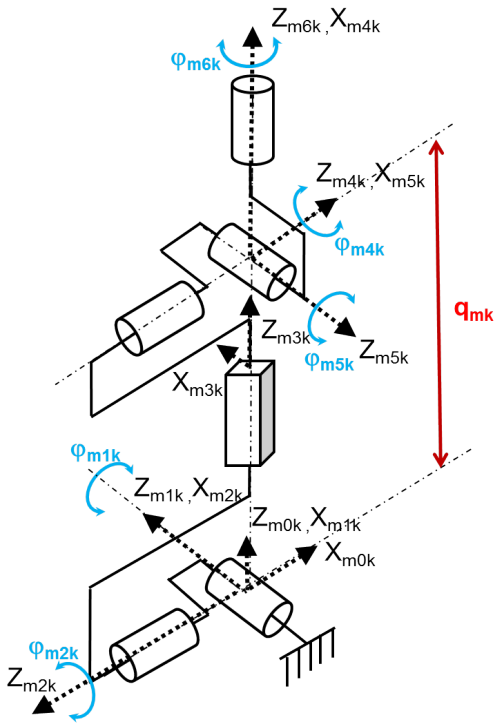

Figure 4.6: Frames placement of a kinematic chain UPS

The passage from a Frame to another is expressed in terms of 4 kinematic parameters:

- ρ_{mnk}: angle between axis $z_{mn(k-1)}$ and z_{mnk} relative to rotation around $x_{m(n-1)k}$;
- λ_{mnk}: distance between $z_{mn(k-1)}$ and z_{mnk} along $x_{m(n-1)k}$;
- φ_{mnk}: angle between axis $x_{mn(k-1)}$ and x_{mnk} relative to rotation around $z_{m(n-1)k}$;
- q_{mk}: distance between $x_{mn(k-1)}$ and x_{mnk} along $z_{m(n-1)k}$.

The forward kinematic model of the closed kinematic chain UPS-PU numbered m can be written in the form of equation (4.16), where ξ_{mnk} is the joint vector defined by equation (4.17).

$$ {}^{0m}_{6m}\mathbf{M} = {}^{0m}_{1m}\mathbf{M}_{(\xi_{m1k})}\,{}^{1m}_{2m}\mathbf{M}_{(\xi_{m2k})}\,{}^{2m}_{3m}\mathbf{M}_{(\xi_{m3k})}\,{}^{3m}_{4m}\mathbf{M}_{(\xi_{m4k})}\,{}^{4m}_{5m}\mathbf{M}_{(\xi_{m5k})}\,{}^{5m}_{6m}\mathbf{M}_{(\xi_{m6k})} \tag{4.16} $$

$$ \xi_{mnk} = [\xi_{m1k}, \xi_{m2k}, \xi_{m3k}, \xi_{m4k}, \xi_{m5k}, \xi_{m6k}]^T \tag{4.17} $$

© 2014 Tous droits réservés.

doc.univ-lille1.fr

Thèse de Coralie Escande, Lille 1, 2013

The joint variable ξ_{mnk} associated to the n^{th} joint ($n = 1, .., 6$) is expressed in equation (4.18), according to the type of the joint, with φ_{mnk} if it concerns a pivot joint, q_{mk} in the case of slide joint.

$$\xi_{mnk} = \varphi_{mnk} + \sigma_{mnk}(q_{mk} - \varphi_{mnk}) \tag{4.18}$$

The variable σ_{mnk} is defined as follows:

- $\sigma_{mnk} = 0$ for pivot joint;
- $\sigma_{mnk} = 1$ for slide joint.

The binary variable μ_{mnk} is introduced to specify the type of actuation:

- $\mu_{mnk} = 1$ for active joint;
- $\mu_{mnk} = 0$ for passive joint.

The parameters in Table 4.2 are used to generate the various transformation matrices $\mathbf{M}$ of equation (4.16), as developed in the set of equations (4.19).

Table 4.2: D-H parameters table

Link	σ_{mnk}	μ_{mnk}	ρ_{mnk}	λ_{mnk}	φ_{mnk}	q_{mk}
1	0	0	$-90°$	0	φ_{m1k}	0
2	0	0	$90°$	0	φ_{m2k}	0
3	1	1	$90°$	0	0	q_{mk}
4	0	0	$90°$	0	φ_{m4k}	0
5	0	0	$-90°$	0	φ_{m5k}	0
6	0	0	$-90°$	0	φ_{m6k}	0

$$ {}^{0m}_{1m}\mathbf{M} = \begin{pmatrix} \cos(\varphi_{m1k}) & \sin(\varphi_{m1k}) & 0 & 0 \\ 0 & 0 & -1 & 0 \\ -\sin(\varphi_{m1k}) & -\cos(\varphi_{m1k}) & 0 & 0 \\ 0 & 0 & 0 & 1 \end{pmatrix} \tag{4.19a} $$

$$ {}^{1m}_{2m}\mathbf{M} = \begin{pmatrix} \cos(\varphi_{m2k}) & \sin(\varphi_{m2k}) & 0 & 0 \\ 0 & 0 & 1 & 0 \\ \sin(\varphi_{m2k}) & \cos(\varphi_{m2k}) & 0 & 0 \\ 0 & 0 & 0 & 1 \end{pmatrix} \tag{4.19b} $$

© 2014 Tous droits réservés.

doc.univ-lille1.fr

Thèse de Coralie Escande, Lille 1, 2013

$$ {}^{2m}_{3m}\mathbf{M} = \begin{pmatrix} 1 & 0 & 0 & 0 \\ 0 & 0 & 1 & -q_{mk} \\ 0 & 1 & 0 & 0 \\ 0 & 0 & 0 & 1 \end{pmatrix} \tag{4.19c} $$

$$ {}^{3m}_{4m}\mathbf{M} = \begin{pmatrix} \cos(\varphi_{m4k}) & \sin(\varphi_{m4k}) & 0 & 0 \\ 0 & 0 & 1 & 0 \\ \sin(\varphi_{m4k}) & \cos(\varphi_{m4k}) & 0 & 0 \\ 0 & 0 & 0 & 1 \end{pmatrix} \tag{4.19d} $$

$$ {}^{4m}_{5m}\mathbf{M} = \begin{pmatrix} \cos(\varphi_{m5k}) & \sin(\varphi_{m5k}) & 0 & 0 \\ 0 & 0 & -1 & 0 \\ -\sin(\varphi_{m5k}) & -\cos(\varphi_{m5k}) & 0 & 0 \\ 0 & 0 & 0 & 1 \end{pmatrix} \tag{4.19e} $$

$$ {}^{5m}_{6m}\mathbf{M} = \begin{pmatrix} \cos(\varphi_{m6k}) & \sin(\varphi_{m6k}) & 0 & 0 \\ 0 & 0 & -1 & 0 \\ -\sin(\varphi_{m6k}) & -\cos(\varphi_{m6k}) & 0 & 0 \\ 0 & 0 & 0 & 1 \end{pmatrix} \tag{4.19f} $$

By replacing the developments of the various matrices (4.19) in equation (4.16), the matrix ${}^{0m}_{6m}\mathbf{M}$ can be written as shown in equation (4.20), where the different matrix elements are given in the set of equations (4.21). The notations C and S means respectively cos and sin.

$$ {}^{0m}_{6m}\mathbf{M} = \begin{pmatrix} t_{11} & t_{12} & t_{13} & t_{14} \\ t_{21} & t_{22} & t_{23} & t_{24} \\ t_{31} & t_{32} & t_{33} & t_{34} \\ 0 & 0 & 0 & 1 \end{pmatrix} \tag{4.20} $$

$$ \begin{aligned} t_{11} = ((&C\varphi_{1mk}C\varphi_{2mk}C\varphi_{4mk} + C\varphi_{1mk}S\varphi_{2mk}S\varphi_{4mk})C\varphi_{5mk} + S\varphi_{1mk}S\varphi_{5mk})C\varphi_{6mk} \\ &- (-C\varphi_{1mk}C\varphi_{2mk}S\varphi_{4mk} + C\varphi_{1mk}S\varphi_{2mk}C\varphi_{4mk})S\varphi_{6mk} \end{aligned} \tag{4.21a} $$

$$ \begin{aligned} t_{12} = ((&C\varphi_{1mk}C\varphi_{2mk}C\varphi_{4mk} + C\varphi_{1mk}S\varphi_{2mk}S\varphi_{4mk})C\varphi_{5mk} + S\varphi_{1mk}S\varphi_{5mk})S\varphi_{6mk} \\ &+ (-C\varphi_{1mk}C\varphi_{2mk}S\varphi_{2mk} + C\varphi_{1mk}S\varphi_{2mk}C\varphi_{4mk})C\varphi_{6mk} \end{aligned} \tag{4.21b} $$

© 2014 Tous droits réservés.

doc.univ-lille1.fr

Thèse de Coralie Escande, Lille 1, 2013

$$t_{13} = -(C\varphi_{m1k}C\varphi_{m2k}C\varphi_{m4k} + C\varphi_{m1k}S\varphi_{m2k}S\varphi_{m4k})S\varphi_{m5k} + S\varphi_{m1k}C\varphi_{m5k} \quad (4.21c)$$

$$t_{14} = -C\varphi_{m1k}S\varphi_{m2k}q_{mk} \quad (4.21d)$$

$$\begin{aligned} t_{21} = (&-S\varphi_{2mk}C\varphi_{4mk} + C\varphi_{2mk}S\varphi_{4mk})C\varphi_{5mk}C\varphi_{6mk} \\ &- (S\varphi_{2mk}S\varphi_{4mk} + C\varphi_{2mk}C\varphi_{4mk})S\varphi_{6mk} \end{aligned} \quad (4.21e)$$

$$\begin{aligned} t_{22} = (&-S\varphi_{2mk}C\varphi_{4mk} + C\varphi_{2mk}S\varphi_{4mk})C\varphi_{5mk}S\varphi_{6mk} \\ &+ (S\varphi_{2mk}S\varphi_{4mk} + C\varphi_{2mk}C\varphi_{4mk})C\varphi_{6mk} \end{aligned} \quad (4.21f)$$

$$t_{23} = -(-S\varphi_{m2k}C\varphi_{m4k} + C\varphi_{m2k}S\varphi_{m4k})S\varphi_{m5k} \quad (4.21g)$$

$$t_{24} = C\varphi_{m2k}q_{mk} \quad (4.21h)$$

$$\begin{aligned} t_{31} = ((&-S\varphi_{m1k}C\varphi_{m2k}C\varphi_{m4k} - S\varphi_{m1k}S\varphi_{m2k}S\varphi_{m4k})C\varphi_{m5k} + C\varphi_{m1k}S\varphi_{m5k})C\varphi_{m6k} \\ &- (S\varphi_{m1k}C\varphi_{m2k}S\varphi_{m4k} - S\varphi_{m1k}S\varphi_{m2k}C\varphi_{m4k})S\varphi_{m6k} \end{aligned} \quad (4.21i)$$

$$\begin{aligned} t_{32} = ((&-S\varphi_{m1k}C\varphi_{m2k}C\varphi_{m4k} - S\varphi_{m1k}S\varphi_{m2k}S\varphi_{m4k})C\varphi_{m5k} + C\varphi_{m1k}S\varphi_{m5k})S\varphi_{m6k} \\ &+ (S\varphi_{m1k}C\varphi_{m2k}S\varphi_{m4k} - S\varphi_{m1k}S\varphi_{m2k}C\varphi_{m4k})C\varphi_{m6k} \end{aligned} \quad (4.21j)$$

$$t_{33} = -(-S\varphi_{m1k}C\varphi_{m2k}C\varphi_{m4k} - S\varphi_{m1k}S\varphi_{m2k}S\varphi_{m4k})S\varphi_{m5k} + C\varphi_{m1k}C\varphi_{m5k} \quad (4.21k)$$

© 2014 Tous droits réservés.

doc.univ-lille1.fr

Thèse de Coralie Escande, Lille 1, 2013

$$t_{34} = S\varphi_{m1k} S\varphi_{m2k} q_{mk} \tag{4.21l}$$

The model of each kinematic chain UPS enables us to model inter-vertebrae, and this will be presented in the next section.

4.3.1.2 Inter-vertebrae Modeling

Inter-vertebrae modeling consists in calculating the position of the center of the upper vertebra in the Frame of the center of the lower vertebra. In terms of mathematical notation, this means that the matrix ${}^{k-1}_{k}\mathbf{M}$ defines the transformation between the Frame $\Re_k$ linked to the upper vertebra and $\Re_{k-1}$ linked to the lower vertebra. This matrix is expressed by the equation (4.22) based on Figure 4.7, given in a closed kinematic chain representation.

$${}^{k-1}_{k}\mathbf{M} = {}^{k-1}_{0m}\mathbf{M}\,{}^{0m}_{6m}\mathbf{M}\,{}^{6m}_{k}\mathbf{M} \tag{4.22}$$

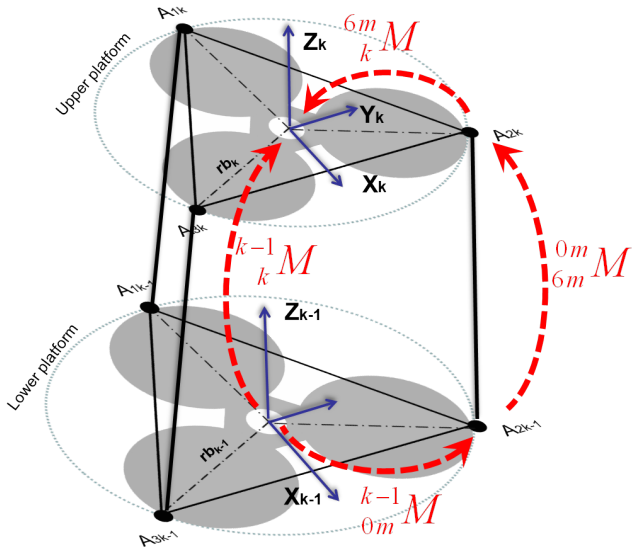

Figure 4.7: Definition of the different transformations

To calculate the transformation matrices ${}^{k-1}_{0m}\mathbf{M}$ and ${}^{6m}_{k}\mathbf{M}$, it is necessary to define the radius rb_k of the vertebra, with the angles τ_1, τ_2 and τ_3 mentioned on Figure 4.8 as equation (4.23).

© 2014 Tous droits réservés.

doc.univ-lille1.fr

Thèse de Coralie Escande, Lille 1, 2013

$$\tau_1 = \pi \ ; \tau_2 = \frac{\pi}{3}; \tau_3 = \frac{5\pi}{3} \tag{4.23}$$

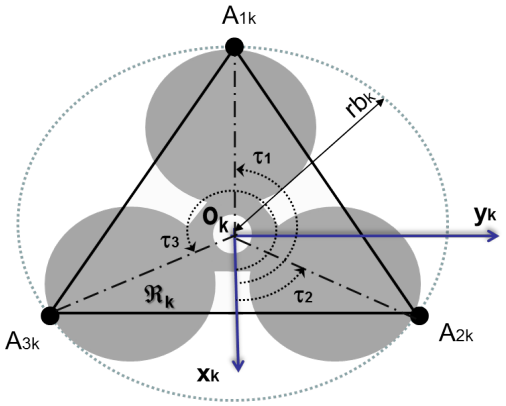

Figure 4.8: Top view of the k^{th}. vertebra

Thus, transformations ${}^{k-1}_{0m}\mathbf{M}$ and ${}^{6m}_{k}\mathbf{M}$ can be expressed respectively as equations (4.24) and (4.25), where $m = 1, .., 3$ and $k = 1, .., 16$:

$${}^{k-1}_{0m}\mathbf{M} = \begin{pmatrix} \cos(\tau_m) & -\sin(\tau_m) & 0 & \cos(\tau_m) rb_{k-1} \\ \sin(\tau_m) & \cos(\tau_m) & 0 & \sin(\tau_m) rb_{k-1} \\ 0 & 0 & 1 & 0 \\ 0 & 0 & 0 & 1 \end{pmatrix} \tag{4.24}$$

$${}^{6m}_{k}\mathbf{M} = \begin{pmatrix} -\sin(\tau_m) & -\cos(\tau_m) & 0 & -rb_k \\ \cos(\tau_m) & -\sin(\tau_m) & 0 & 0 \\ 0 & 0 & 1 & 0 \\ 0 & 0 & 0 & 1 \end{pmatrix} \tag{4.25}$$

Equation (4.22) can be written according to equation (4.26), where, ${}^{k-1}_{k}\mathbf{M}$ is the transformation matrix of the target pose $\{X_k,\ Y_k,\ Z_k, \Phi_k, \Theta_k, \Psi_k\}$ of the upper-vertebra relative to the lower-vertebra, as shown in equation (4.27), where c means cos and s means sin.

$${}^{k-1}_{k}\mathbf{M} = {}^{k-1}_{0m}\mathbf{M}^{0m}_{1m}\mathbf{M}^{1m}_{2m}\mathbf{M}^{2m}_{3m}\mathbf{M}^{3m}_{4m}\mathbf{M}^{4m}_{5m}\mathbf{M}^{5m}_{6m}\mathbf{M}^{6m}_{k}\mathbf{M} \tag{4.26}$$

$${}^{k-1}_{k}\mathbf{M} = \begin{pmatrix} c\Phi_k c\Theta_k & c\Phi_k s\Theta_k s\Psi_k - s\Phi_k c\Psi_k & c\Phi_k s\Theta_k c\Psi_k + s\Phi_k s\Psi_k & X_k \\ s\Phi_k c\Theta_k & s\Phi_k s\Theta_k s\Psi_k + c\Phi_k c\Psi_k & s\Phi_k s\Theta_k c\Psi_k - c\Phi_k s\Psi_k & Y_k \\ -s\Theta_k & s\Psi_k c\Theta_k & c\Psi_k c\Theta_k & Z_k \\ 0 & 0 & 0 & 1 \end{pmatrix} \tag{4.27}$$

© 2014 Tous droits réservés.

doc.univ-lille1.fr

Thèse de Coralie Escande, Lille 1, 2013

Then, it is possible to rewrite equation (4.26) as equation (4.28). Members of the left and right side of equation (4.28) represent the composition of the Basis Frame transformation $\Re_{0m}$ to the Frame $\Re_{4m}$, using two distinct paths whose elements are functions of joint variables. As mentioned in equation (4.29), with A, B and C being constant parameters, independent from the joints. Thus equation (4.29) shows that the prismatic joints q_{mk} depend only on joints φ_{m1k} and φ_{m2k}. The identification elements by elements of the 4^{th} column of equality (4.29) establishes the three equations (4.30a), (4.30b) and (4.30c).

$$ {}^{0m}_{1m}\mathbf{M}^{1m}_{2m}\mathbf{M}^{2m}_{3m}\mathbf{M}^{3m}_{4m}\mathbf{M} = {}^{0m}_{k-1}\mathbf{M}^{k-1}_{k}\mathbf{M}^{k}_{6m}\mathbf{M}^{6m}_{5m}\mathbf{M}^{5m}_{4m}\mathbf{M} \tag{4.28} $$

$$ \begin{pmatrix} f11(\varphi_{m2k}) & f12(\varphi_{m2k},\varphi_{m4k}) & f13(\varphi_{m2k},\varphi_{m3k}) & f14(\varphi_{m2k},q_{mk}) \\ f21(\varphi_{m1k},\varphi_{m2k}) & f22(\varphi_{m1k},\varphi_{m2k},\varphi_{m4k}) & f23(\varphi_{m1k},\varphi_{m2k},\varphi_{m4k}) & f24(\varphi_{m1k},\varphi_{m2k},q_{mk}) \\ f31(\varphi_{m1k},\varphi_{m2k}) & f32(\varphi_{m1k},\varphi_{m2k},\varphi_{m4k}) & f33(\varphi_{1mk},\varphi_{m2k},\varphi_{m4k}) & f34(\varphi_{m1k},\varphi_{m2k},q_{mk}) \\ 0 & 0 & 0 & 1 \end{pmatrix} $$
$$ = \begin{pmatrix} g11(\varphi_{m5k},\varphi_{m6k}) & g12(\varphi_{m6k}) & g13(\varphi_{m5k},\varphi_{m6k}) & A \\ g21(\varphi_{m5k},\varphi_{m6k}) & g22(\varphi_{m6k}) & g23(\varphi_{m5k},\varphi_{m6k}) & B \\ g31(\varphi_{m5k},\varphi_{m6k}) & g32(\varphi_{m6k}) & g33(\varphi_{m5k},\varphi_{m6k}) & C \\ 0 & 0 & 0 & 1 \end{pmatrix} \tag{4.29} $$

$$ \begin{gathered} rb_k\cos(\Theta_k)\cos(\Phi_k)\cos(\tau_m)^2 + rb_k\cos(\Theta_k)\sin(\tau_m)\sin(\Phi_k)\cos(\tau_m) + Y_k\sin(\tau_m) \\ + rb_k\sin(\tau_m)\cos(\tau_m)\cos(\Phi_k)\sin(\Theta_k)\sin(\Psi_k) + rb_k\sin(\Phi_k)\sin(\Theta_k)\sin(\Psi_k) \\ - rb_k\sin(\tau_m)\cos(\tau_m)\sin(\Phi_k)\cos(\Psi_k) - rb_k\cos(\tau_m)^2\sin(\Phi_k)\sin(\Theta_k)\sin(\Psi_k) \\ + rb_k\cos(\Phi_k)\cos(\Psi_k) - rb_k\cos(\tau_m)^2\cos(\Phi_k)\cos(\Psi_k) + X_k\cos(\tau_m) \\ - rb_{k-1} = -\cos(\varphi_{m1k})\sin(\varphi_{m2k})q_{mk} \end{gathered} \tag{4.30a} $$

$$ \begin{gathered} -rb_k\cos(\Theta_k)\sin(\tau_m)\cos(\Phi_k)\cos(\tau_m) + rb_k\cos(\Theta_k)\cos(\tau_m)^2\sin(\Phi_k) + \cos(\tau_m)Y_k \\ + rb_k\cos(\tau_m)^2\cos(\Phi_k)\sin(\Theta_k)\sin(\Psi_k) + rb_k\sin(\tau_m)\cos(\tau_m)\cos(\Phi_k)\cos(Psi) \\ + rb_k\sin(\Phi_k)\cos(\Psi_k) - rb_k\cos(\tau_m)^2\sin(\Phi_k)\cos(\Psi_k) - rb_k\cos(\Phi_k)\sin(\Theta_k)\sin(\Psi_k) \\ + rb_k\sin(\tau_m)\cos(\tau_m)\sin(\Phi_k)\sin(\Theta_k)\sin(\Psi_k) - \sin(\tau_m)X_k = \cos(\varphi_{m2k})q_{mk} \end{gathered} \tag{4.30b} $$

© 2014 Tous droits réservés.

doc.univ-lille1.fr

Thèse de Coralie Escande, Lille 1, 2013

$$-rb_k \sin(\Theta_k)\cos(\tau_m)+rb_k \cos(\Theta_k)\sin(\Psi_k)\sin(\tau_m)+Z_k \;=\; \sin(\varphi_{m1k})\sin(\varphi_{m2k})q_{mk} \tag{4.30c}$$

However, in the case of the CBHA, the matrix ${}^{k-1}_{k}\mathbf{M}$ given by equation (4.27) represents the transformation of the kinematic chain PU, which adds constraints movement: translations along the x- and y-axis and torsion around z-axis are not possible. Thus, ${}^{k-1}_{k}\mathbf{M}$ matrix can be written in a simplified form as shown in equation (4.31).

$${}^{k-1}_{k}\mathbf{M} = \begin{pmatrix} \cos\Theta_k & \sin\Theta_k \sin\Psi_k & \sin\Theta_k \cos\Psi_k & 0 \\ 0 & \cos\Psi_k & -\sin\Psi_k & 0 \\ -\sin\Theta_k & \sin\Psi_k \cos\Theta_k & \cos\Psi_k \cos\Theta_k & Z_k \\ 0 & 0 & 0 & 1 \end{pmatrix} \tag{4.31}$$

This simplifies greatly the three equations(4.30a), (4.30b) and (4.30c) as shown in equations (4.32a), (4.32b) and (4.32c).

$$\begin{aligned} rb_k \cos(\Theta_k)\cos\left(\tau_m\right)^2 + rb_k \sin(\tau_m)\cos(\tau_m)\sin(\Theta_k)\sin(\Psi_k) + rb_k \cos(\Psi_k) \\ - rb_k \cos\left(\tau_m\right)^2 \cos(\Psi_k) - rb_{k-1} = -\cos(\varphi_{m1k})\sin(\varphi_{m2k})q_{mk} \end{aligned} \tag{4.32a}$$

$$\begin{aligned} -\sin(\tau_m)(\cos(\Theta_k)\cos(\tau_m) + \sin(\tau_m)\sin(\Theta_k)\sin(\Psi_k) - rb_k \cos(\tau_m)\cos(\Psi_k)) \\ = \cos(\varphi_{m2k})q_{mk} \end{aligned} \tag{4.32b}$$

$$-rb_k \sin(\Theta_k)\cos(\tau_m) + rb_k \cos(\Theta_k)\sin(\Psi_k)\sin(\tau_m) + Z_k = \sin(\varphi_{m1k})\sin(\varphi_{m2k})q_{mk} \tag{4.32c}$$

The solution of this system of three equations (4.32) with three unknown variables (q_{mk}, ϕ_{m1k}, ϕ_{m2k}) gives the expression of q_{mk} in function of known variables. The inverse kinematic model of inter-vertebra is obtained by substituting the index $m = 1, .., 3$ in q_{mk}, as shown in the system of equations (4.33), which contains 2 distinct solutions: $q_{mk} = \sqrt{{q_{mk}}^2}$ and $q_{mk} = -\sqrt{{q_{mk}}^2}$. Since the variable q_{mk}

© 2014 Tous droits réservés.

doc.univ-lille1.fr

Thèse de Coralie Escande, Lille 1, 2013

defines a distance, the positive solution $q_{mk} = \sqrt{{q_{mk}}^2}$ is selected.

$$q_{1k}^2 = Z_k^2 + 2rb_k Z_k \sin(\Theta_k) - 2rb_k rb_{k-1}\cos(\Theta_k) + rb_k^2 + rb_{k-1}^2 \tag{4.33a}$$

$$\begin{aligned} q_{2k}^2 = {} & Z_k^2 + rb_k^2 + rb_{k-1}^2 + Z_k rb_k(\sqrt{3}\cos(\Theta_k)\sin(\Psi_k) - \sin(\Theta_k)) \\ & - rb_k rb_{k-1}(\frac{\sqrt{3}}{2}\sin(\Theta_k)\sin(\Psi_k) + \frac{3}{2}\cos(\Psi_k) + \frac{1}{2}\cos(\Theta_k)) \end{aligned} \tag{4.33b}$$

$$\begin{aligned} q_{3k}^2 = {} & Z_k^2 + rb_k^2 + rb_{k-1}^2 - Z_k rb_k(\sqrt{3}\cos(\Theta_k)\sin(\Psi_k) + \sin(\Theta_k)) \\ & + rb_k rb_{k-1}(\frac{\sqrt{3}}{2}\sin(\Theta_k)\sin(\Psi_k) - \frac{3}{2}\cos(\Psi_k) - \frac{1}{2}\cos(\Theta_k)) \end{aligned} \tag{4.33c}$$

4.3.2 Geometrical Model Based of the Inter-vertebra (Chasles Theorem)

Unlike the previous method, which requires more calculations, the geometric method is valid only for parallel robots with six degrees of freedom; it offers in only some relations a unique solution, based on a few basic geometric relationships. This method was applied for robots such as "snake-like catheter manipulator", representing parallel robots type 3-RPS assembled in series (Mintenbeck et al. 2010). In Figure 4.9, it is shown the attachment points of three kinematic chains UPS: the points A_{mk} designate the vertices of the upper vertebra and the points A_{mk-1} the vertices of the lower vertebra, where $m = 1, .., 3$, represents the number of kinematic chains UPS and $k = 0, .., 16$ the number of inter-vertebrae. The coordinates of these three points are given by equations (4.34), relative to the center of the k^{th} vertebra.

$$A_{1k} = \begin{bmatrix} -rb_k \\ 0 \\ 0 \end{bmatrix}; A_{2k} = \begin{bmatrix} \frac{1}{2}rb_k \\ \frac{\sqrt{3}}{2}rb_k \\ 0 \end{bmatrix}; A_{3k} = \begin{bmatrix} \frac{1}{2}rb_k \\ -\frac{\sqrt{3}}{2}rb_k \\ 0 \end{bmatrix} \tag{4.34}$$

© 2014 Tous droits réservés.

doc.univ-lille1.fr

Thèse de Coralie Escande, Lille 1, 2013

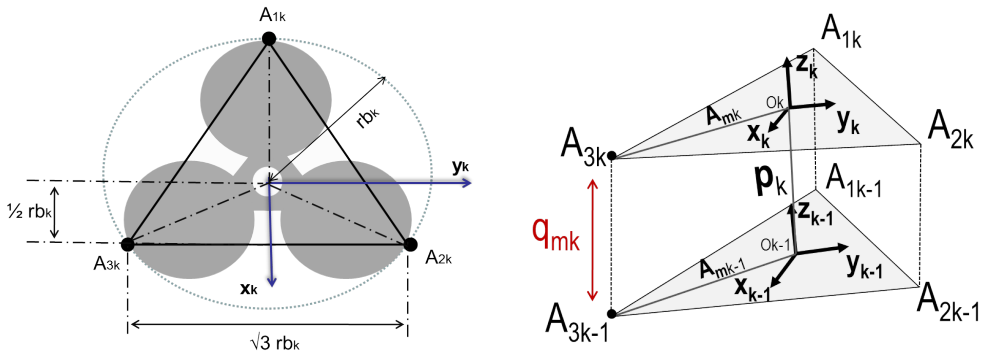

(a) (b)

Figure 4.9: Definition of attachment points: (a) Top view representation of attachment points of one vertebra, (b) Spatial representation of attachment points

A reference Frame $\Re_{k-1}\{O_{k-1}, x_{k-1}, y_{k-1}, z_{k-1}\}$ is located in the center of the lower-vertebra. Similarly, another reference Frame, is located in the center of the upper-vertebra $\Re_k\{O_k, x_k, y_k, z_k\}$. The length of the active prismatic joint kinematic chain for each UPS is defined by: $q_{mk} = \mathbf{A}_{mk}\mathbf{A}_{mk-1}$ with $m = 1, .., 3$ and $k = 0, .., 16$. Thus, the inverse kinematics of the parallel manipulator can be solved by equation (4.35) which describes the relationship of Chasles.

$$\overrightarrow{q_{mk}} = \overrightarrow{A_{mk-1}A_{mk}} = \overrightarrow{A_{mk-1}O_{k-1}} + \overrightarrow{O_{k-1}O_k} + \overrightarrow{O_kA_{mk}} \tag{4.35}$$

If the position of the upper-vertebra is denoted by the vector $\mathbf{P}_k$ and the orientation is denoted by the rotation matrix $\mathbf{R}^{Ok}_{Ok-1}$, then the vector $\overrightarrow{q_{mk}}$ in the Frame $\Re_{k-1}$ can be expressed by equation 4.36, where $\mathbf{P}_k$ is given by equation (4.37) and $\mathbf{R}^{Ok}_{Ok-1}$ is given by equation (4.38).

$$\mathbf{Q}_{mk}|_{\Re_{k-1}} = \mathbf{P}_k + \mathbf{R}^{Ok}_{Ok-1} \times \mathbf{A}_{mk} - \mathbf{A}_{mk-1} \tag{4.36}$$

$$\mathbf{P}_k = \begin{bmatrix} X_k \\ Y_k \\ Z_k \end{bmatrix} \tag{4.37}$$

$$\mathbf{R}^{Ok}_{Ok-1} = \begin{bmatrix} c\Phi_k c\Theta_k & c\Phi_k s\Theta_k s\Psi_k - s\Phi_k c\Psi_k & c\Phi_k s\Theta_k c\Psi_k + s\Phi_k s\Psi_k \\ s\Phi_k c\Theta_k & s\Phi_k s\Theta_k s\Psi_k + c\Phi_k c\Psi_k & s\Phi_k s\Theta_k c\Psi_k - c\Phi_k s\Psi_k \\ -s\Theta_k & s\Psi_k c\Theta_k & c\Psi_k c\Theta_k \end{bmatrix} \tag{4.38}$$

After substituting the expressions of $\mathbf{P}_k$ and $\mathbf{R}^{Ok}_{Ok-1}$ in equation (4.36), the

© 2014 Tous droits réservés.

doc.univ-lille1.fr

Thèse de Coralie Escande, Lille 1, 2013

equations (4.39a), (4.39b) and (4.39c) are obtained.

$$\mathbf{Q}_{1k} = \begin{bmatrix} X_k - \cos(\Phi_k)\cos(\Theta_k) rb_k + rb_{k-1} \\ Y_k - \sin(\Phi_k)\cos(\Theta_k) rb_k \\ Z_k + \sin(\Theta_k) rb_k \end{bmatrix} \tag{4.39a}$$

$$\mathbf{Q}_{2k} = \begin{bmatrix} X_k + \frac{1}{2}\cos(\Phi_k)\cos(\Theta_k) rb_k + \frac{\sqrt{3}}{2} rb_k(\cos(\Phi_k)\sin(\Theta_k)\sin(\Psi_k) - \sin(\Phi_k)\cos(\Psi_k)) - \frac{1}{2} rb_{k-1} \\ Y_k + \frac{1}{2}\sin(\Phi_k)\cos(\Theta_k) rb_k + \frac{\sqrt{3}}{2} rb_k(\sin(\Phi_k)\sin(\Theta_k)\sin(\Psi_k) + \cos(\Phi_k)\cos(\Psi_k)) - \frac{\sqrt{3}}{2} rb_{k-1} \\ Z_k - \frac{1}{2}\sin(\Theta_k) rb_k + \frac{\sqrt{3}}{2}\cos(\Theta_k)\sin(\Psi_k) rb_k \end{bmatrix} \tag{4.39b}$$

$$\mathbf{Q}_{3k} = \begin{bmatrix} X_k + \frac{1}{2}\cos(\Phi_k)\cos(\Theta_k) rb_k - \frac{\sqrt{3}}{2} rb_k(\cos(\Phi_k)\sin(\Theta_k)\sin(\Psi_k) - \sin(\Phi_k)\cos(\Psi_k)) - \frac{1}{2} rb_{k-1} \\ Y_k + \frac{1}{2}\sin(\Phi_k)\cos(\Theta_k) rb_k - \frac{\sqrt{3}}{2} rb_k(\sin(\Phi_k)\sin(\Theta_k)\sin(\Psi_k) - \cos(\Phi_k)\cos(\Psi_k)) + \frac{\sqrt{3}}{2} rb_{k-1} \\ Z_k - \frac{1}{2}\sin(\Theta_k) rb_k - \frac{\sqrt{3}}{2}\cos(\Theta_k)\sin(\Psi_k) rb_k \end{bmatrix} \tag{4.39c}$$

Expression q_{mk} corresponds to the vectors norm of (4.39a), (4.39b) and (4.39c), as shown in equation (4.40).

$$q_{mk} = \|\mathbf{Q}_{mk}\| = (\mathbf{Q}_{mk}{}^T \,.\, \mathbf{Q}_{mk})^{1/2} \tag{4.40}$$

After developing this equation, the following expression is obtained:

$$\begin{aligned} q_{1k} = {} & (X_k{}^2 + Y_k{}^2 + Z_k{}^2 - 2rb_k(X_k\cos(\Phi_k)\cos(\Theta_k) + Y_k\sin(\Phi_k)\cos(\Theta_k) - Z_k\sin(\Theta_k)) \\ & + 2rb_{k-1}X_k - 2rb_k rb_{k-1}\cos(\Phi_k)\cos(\Theta_k) + rb_k{}^2(\sin(\Theta_k)^2 + \sin(\Phi_k)^2\cos(\Theta_k)^2 \\ & + \cos(\Phi_k)^2\cos(\Theta_k)^2) + rb_{k-1}{}^2)^{1/2} \end{aligned} \tag{4.41}$$

© 2014 Tous droits réservés.

doc.univ-lille1.fr

Thèse de Coralie Escande, Lille 1, 2013

$$
\begin{aligned}
q_{2k} = {} & ({X_k}^2 + {Y_k}^2 + {Z_k}^2 + {rb_k}^2 + {rb_{k-1}}^2 - rb_{k-1}(X_k + \sqrt{3}Y_k) \\
& + rb_k rb_{k-1}(\frac{\sqrt{3}}{2}\sin(\Phi_k)\cos(\Psi_k) - \frac{\sqrt{3}}{2}\cos(\Phi_k)\sin(\Theta_k)\sin(\Psi_k) - \frac{\sqrt{3}}{2}\sin(\Phi_k)\cos(\Theta_k) \\
& - \frac{3}{2}\sin(\Phi_k)\sin(\Theta_k)\sin(\Psi_k) - \frac{3}{2}\cos(\Phi_k)\cos(\Psi_k) - \frac{1}{2}\cos(\Phi_k)\cos(\Theta_k)) \\
& + rb_k(X_k\cos(\Phi_k)\cos(\Theta_k) + \sqrt{3}X_k\cos(\Phi_k)\sin(\Theta_k)\sin(\Psi_k) - \sqrt{3}X_k\sin(\Phi_k)\cos(\Psi_k) \\
& + Y_k\sin(\Phi_k)\cos(\Theta_k) + \sqrt{3}Y_k\sin(\Phi_k)\sin(\Theta_k)\sin(\Psi_k) + \sqrt{3}Y_k\cos(\Phi_k)\cos(\Psi_k) \\
& - Z_k\sin(\Theta_k) + \sqrt{3}Z_k\cos(\Theta_k)\sin(\Psi_k)))^{1/2}
\end{aligned}
\tag{4.42}
$$

$$
\begin{aligned}
q_{3k} = {} & ({X_k}^2 + {Y_k}^2 + {Z_k}^2 + {rb_k}^2 + {rb_{k-1}}^2 - rb_{k-1}(X_k - \sqrt{3}Y_k) \\
& + rb_k rb_{k-1}(-\frac{\sqrt{3}}{2}\sin(\Phi_k)\cos(\Psi_k) + \frac{\sqrt{3}}{2}\cos(\Phi_k)\sin(\Theta_k)\sin(\Psi_k) + \frac{\sqrt{3}}{2}\sin(\Phi_k)\cos(\Theta_k) \\
& - \frac{3}{2}\sin(\Phi_k)\sin(\Theta_k)\sin(\Psi_k) - \frac{3}{2}\cos(\Phi_k)\cos(\Psi_k) - \frac{1}{2}\cos(\Phi_k)\cos(\Theta_k)) \\
& + rb_k(X_k\cos(\Phi_k)\cos(\Theta_k) - \sqrt{3}X_k\cos(\Phi_k)\sin(\Theta_k)\sin(\Psi_k) + \sqrt{3}X_k\sin(\Phi_k)\cos(\Psi_k) \\
& + Y_k\sin(\Phi_k)\cos(\Theta_k) - \sqrt{3}Y_k\sin(\Phi_k)\sin(\Theta_k)\sin(\Psi_k) - \sqrt{3}Y_k\cos(\Phi_k)\cos(\Psi_k) \\
& - Z_k\sin(\Theta_k) - \sqrt{3}Z_k\cos(\Theta_k)\sin(\Psi_k)))^{1/2}
\end{aligned}
\tag{4.43}
$$

These expressions can be simplified by induced constraints to the movements related to the passive kinematic chain PU: $\Phi_k = 0$ because torsion is not allowed; $X_k = 0$ and $Y_k = 0$, because only the z translation is possible along the upper-vertebra relative to the lower-vertebra. Thus, the analytical solution of the inverse kinematic model of an inter-vertebra is:

$$
q_{1k} = \sqrt{{Z_k}^2 + 2rb_k Z_k\sin(\Theta_k) - 2rb_k rb_{k-1}\cos(\Theta_k) + {rb_k}^2 + {rb_{k-1}}^2} \tag{4.44}
$$

$$
\begin{aligned}
q_{2k} = {} & ({Z_k}^2 + Z_k rb_k(\sqrt{3}\cos(\Theta_k)\sin(\Psi_k) - \sin(\Theta_k)) - rb_k rb_{k-1}(\frac{\sqrt{3}}{2}\sin(\Theta_k)\sin(\Psi_k) \\
& + \frac{3}{2}\cos(\Psi_k) + \frac{1}{2}\cos(\Theta_k)) + {rb_k}^2 + {rb_{k-1}}^2)^{1/2}
\end{aligned}
\tag{4.45}
$$

© 2014 Tous droits réservés.

doc.univ-lille1.fr

Thèse de Coralie Escande, Lille 1, 2013

$$q_{3k} = ({Z_k}^2 - Z_k rb_k \left(\sqrt{3}\cos(\Theta_k)\sin(\Psi_k) + \sin(\Theta_k)\right) + rb_k rb_{k-1}(\frac{\sqrt{3}}{2}\sin(\Theta_k)\sin(\Psi_k) - \frac{3}{2}\cos(\Psi_k) - \frac{1}{2}\cos(\Theta_k)) + {rb_k}^2 + {rb_{k-1}}^2)^{1/2} \tag{4.46}$$

The result corresponds to the solution obtained by the first method of Raghavan and Roth. With the inverse kinematic model of an inter-vertebra, it is possible to obtain the inverse kinematic model of the CBHA, thanks to the generalized method described in the next section.

4.4 Generalized Kinematic Modeling of the CBHA

In this section, only the position $\{x, y, z\}$ of the end of the bionic arm is assumed to be known. This assumption complicates the issue of model calculation because the top of the arm can reach a special position with several possible postures. This illustrates the case of multiple solutions to the inverse kinematic model with infinite number of solutions. To solve this problem, an effective selection criteria associated with appropriate constraints is necessary to find the optimal posture of the CBHA. Thus, the resolution by the analytical method cannot lead to an explicit form of the inverse kinematic model. Numerical resolution, specifically, an iterative optimization method is adopted in our following development.

Figure 4.10 illustrates the process of calculating the inverse kinematic model of the CBHA using the optimization approach. The workspace is developed at the end of this chapter. From the desired position, the curve crossing the center of the CBHA is generated with the assumption of constant curvature. A method based on sequential quadratic programming (SQP) is used to spread the backbone along the curve, such that the distribution keeps uniform for the backbone along the curve. This method allows estimating the position of each vertebra, which is then included into the calculation of the inverse kinematic model of an inter-vertebra, presented in the previous section. When the distances q_{mk} are found, they are then summed to find the lengths of the CBHA's tubes. This process provides at the end an optimized posture of the CBHA, such as the curvature is the smallest one, with a minimum energy.

© 2014 Tous droits réservés.

doc.univ-lille1.fr

Thèse de Coralie Escande, Lille 1, 2013

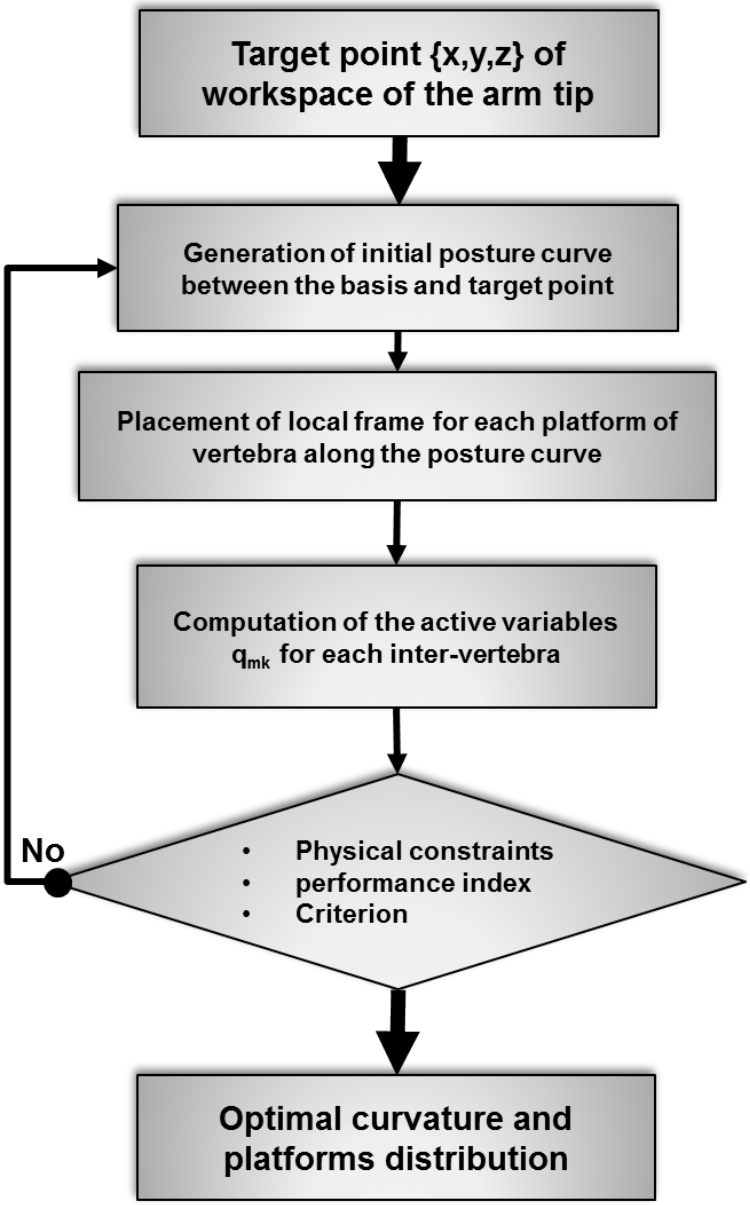

Figure 4.10: IKM Steps Calculation

In the following sections, first it is presented how the generation of the curve is performed and secondly the SQP method is developed.

© 2014 Tous droits réservés.

doc.univ-lille1.fr

Thèse de Coralie Escande, Lille 1, 2013

4.4.1 Curve Generation

Generally, Frenet-Serret Frame placement method is used to associate Frames to curve according to its tangent and orientation. Unfortunately, when the curve involves direction changes, the direction of the Frenet-Serret Frames changes in such a way that it can result in a torsion. However, the bionic arm CBHA is a hyper-redundant robot with frequent orientation changes of the curve but without possible torsion. Thus, an alternative approach based on Bishop Frames (Hanson and H. Ma 1995; Karacan et al. 2010) are more considered in our case study.

As mentioned in chapter 1, a Bishop Frame has three orthonormal unit vectors: a tangent vector to the curve $\mathbf{T}(s)$, a normal vector $\mathbf{N}_1(s)$ and a binormal vector $\mathbf{N}_2(s)$. Figure 4.11 shows various Bishop Frames $(O_k, N_{1k}, N_{2k}, T_k)$ along the central curve of the CBHA.

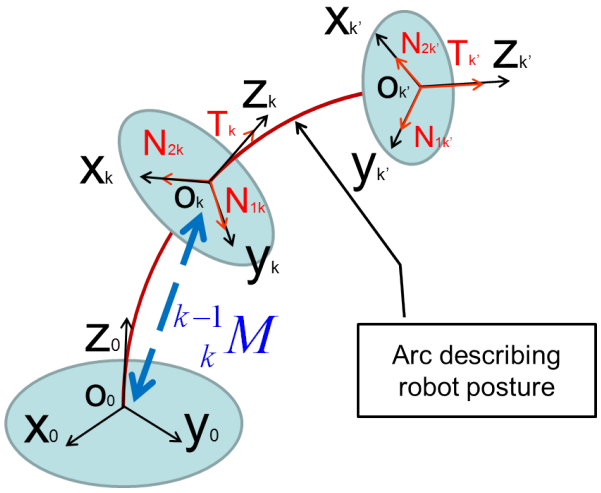

Figure 4.11: Placement of Bishop Frames on the CBHA's central curve

Then, the homogeneous transformation of equation (4.49) is obtained in function of the vector (4.47) and the matrix (4.48):

$$\mathbf{t}\,(s) = [x\,(s)\,y\,(s)\,z(s)] \tag{4.47}$$

$$\mathbf{Rot}(s) = [\mathbf{T}\,(s)\,\mathbf{N1}\,(s)\,\mathbf{N2}\,(s)] \tag{4.48}$$

$$\mathbf{M}_k(s) = \begin{pmatrix} \mathbf{Rot}(s) & \mathbf{t}(s) \\ 0 & 1 \end{pmatrix} \tag{4.49}$$

The obtained curve is parameterized by a vector $\mathbf{t} \in R^3 : \mathbf{t} = \mathbf{t}(s)$, where s

© 2014 Tous droits réservés.

doc.univ-lille1.fr

Thèse de Coralie Escande, Lille 1, 2013

is a variable parameter representing the length when crossing the curve, and is subjected to the following constraints:

- The constant curvature with a perfect arc of circle;
- The point of departure of the curve is perpendicular to the horizontal plane.

4.4.2 Optimal Placement of the Frames Using SQP Method

The Frames placement optimization is performed by a Sequential Quadratic Programming (SQP), as it is a non-linear problem under linear inequality constraints. The optimization issue can be formulated by $f(q)$, that represents the objective function adopted in the optimization procedure, as follows:

$$f(q) = \sqrt{\lambda_{\max}(Q^T Q)} \tag{4.50}$$

where $\lambda_{\max}(Q^T Q)$ is the maximum eigenvalue of $Q^T Q$.

$$\begin{cases} \min f(q) \\ q_{k,\min} \leq q_{mk} \leq q_{k,\max} \\ L_{2,\min} \leq L_2 = \frac{1}{3} \sum_{k=1}^{16} \sum_{m=1}^{3} q_{mk} \leq L_{2,\max} \end{cases} \tag{4.51}$$

Constraint values were obtained by experimental measurements and are given in Table 4.3, with $L_{\min} = 203\,\text{mm}$ et $L_{\max} = 207\,\text{mm}$.

Table 4.3: Extremal values of the lengths of each inter-vertebra in millimeter for the case of CBHA

k^{th}	**1**	**2**	**3**	**4**	**5**	**6**	**7**	**8**
$q_{\min}$	7	8	8	7.5	7.5	7.5	7.5	12
$q_{\max}$	25.5	18	17.9	18	17.5	17.5	17	18
k^{th}	**9**	**10**	**11**	**12**	**13**	**14**	**15**	**16**
$q_{\min}$	8.5	8	7.5	7	7	7	7	7
$q_{\max}$	16.5	20	20	19	18.2	18	17.5	18.5

© 2014 Tous droits réservés.

doc.univ-lille1.fr

Thèse de Coralie Escande, Lille 1, 2013

4.5 Experimental Validation

4.5.1 Obtained Results

To validate the inverse kinematic model, the experimental data obtained with the test bench described in chapter 3, representing the coupled industrial manipulator and the bionic arm, are used. The optimization toolbox of MATLAB is then used with the "*fmincon*" function. The Figure 4.12 shows the architecture of the IKM validation. On one hand, the IKM presented in this chapter is used to calculate the optimized lengths from the measured positions by the industrial manipulator KUKA. These optimized lengths are then injected in the FKM presented in the chapter 2 with the calibrated values obtained in the chapter 3 in order to calculate the optimized positions. These latter are then compared to the measured positions by KUKA, in calculating the optimized Cartesian coordinates error. On the other hand, the FKM previously mentioned is used to calculate the estimated positions from the measured tubes lengths by CBHA. These estimated positions are then compared to the measured positions by KUKA, in calculating the estimated Cartesian coordinates error.

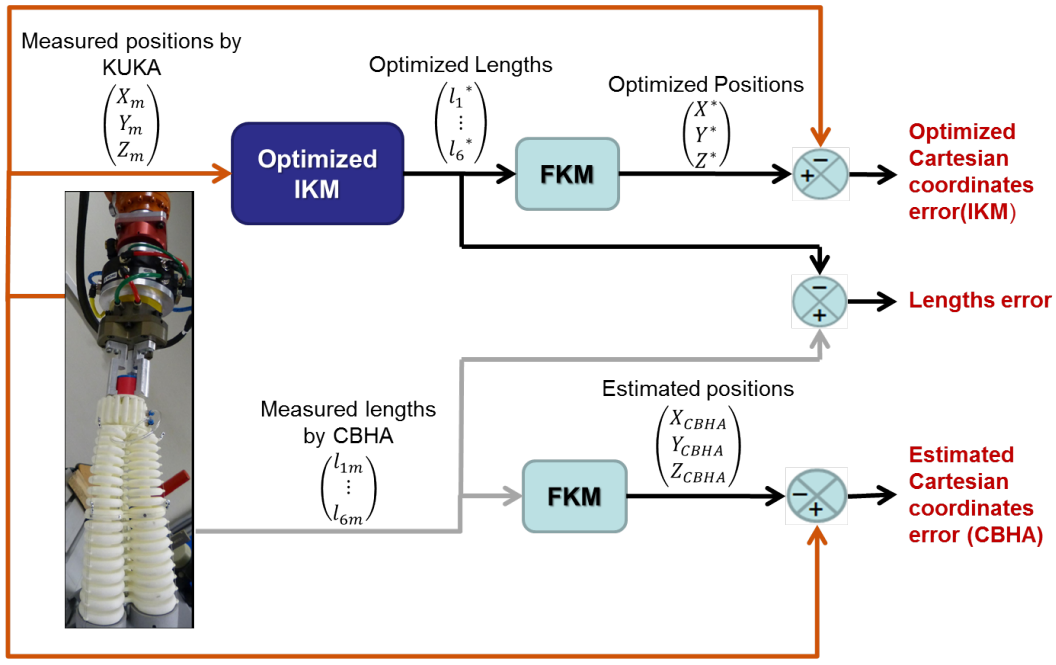

Figure 4.12: Architecture of the experimental validation

Figure 4.13 mentions the CBHA posture obtained after the optimization process of the IKM. The display of the obtained posture allowed verifying that it is coherent with the real posture and that the curvature is minimized. It also shows

© 2014 Tous droits réservés.

doc.univ-lille1.fr

Thèse de Coralie Escande, Lille 1, 2013

the optimized distribution of the different vertebrae along the central backbone curve used in the inverse kinematic model calculation. Indeed, the pose of each vertebra determines the inter-vertebra distances q_{mk}, and thus the tubes lengths. The Figure4.14 defines the different tubes lengths of the CBHA.

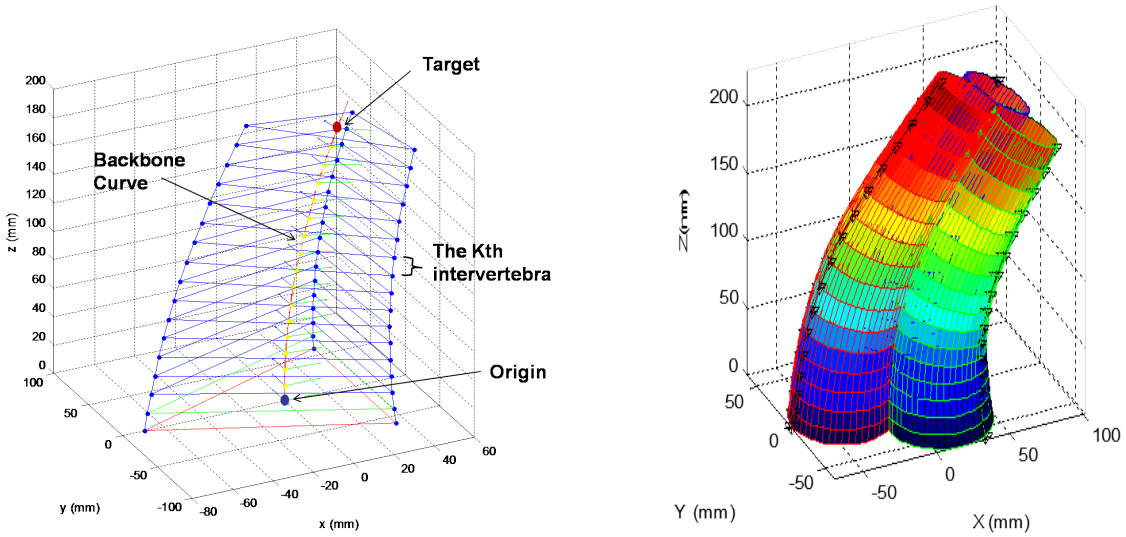

(a) Distribution of backbone along the bionic arm (b) Posture 3D optimization

Figure 4.13: Simulated representation of posture of CBHA

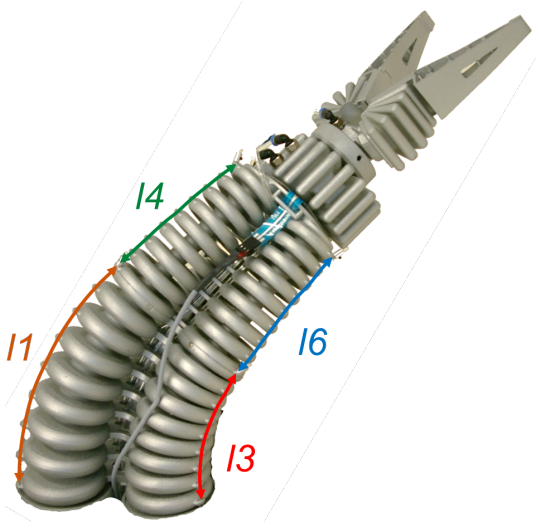

Figure 4.14: Definition of lengths l_i

© 2014 Tous droits réservés.

doc.univ-lille1.fr

Thèse de Coralie Escande, Lille 1, 2013

The trajectories of the measured, the estimated and the optimized data for the tip arm are given in Figure 4.15.

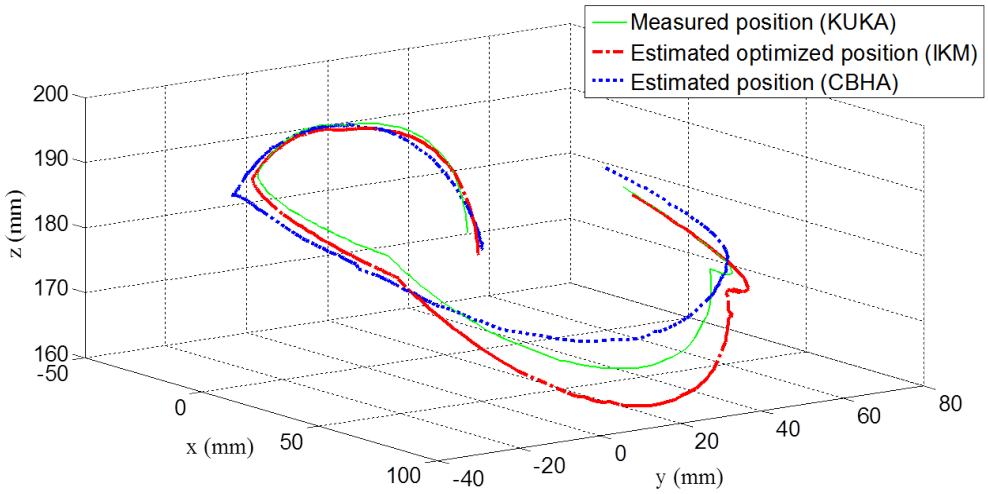

Figure 4.15: Trajectories of measured positions and of estimated positions from optimized IKM and CBHA FKM

The Figures 4.16, 4.17 and 4.18 present the length errors. The Figures 4.19 and 4.20 present the linear optimized and estimated errors for the tip arm position. The Figures 4.21 and 4.22 present the Euclidian optimized and estimated errors for the tip arm position.

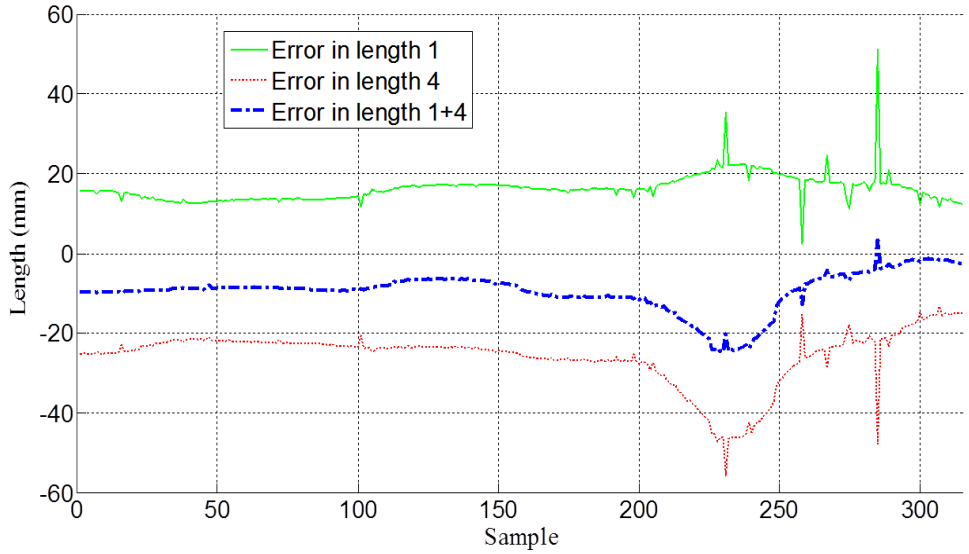

Figure 4.16: Error in lengths l_1, l_4 and l_{1+4}

© 2014 Tous droits réservés.

doc.univ-lille1.fr

Thèse de Coralie Escande, Lille 1, 2013

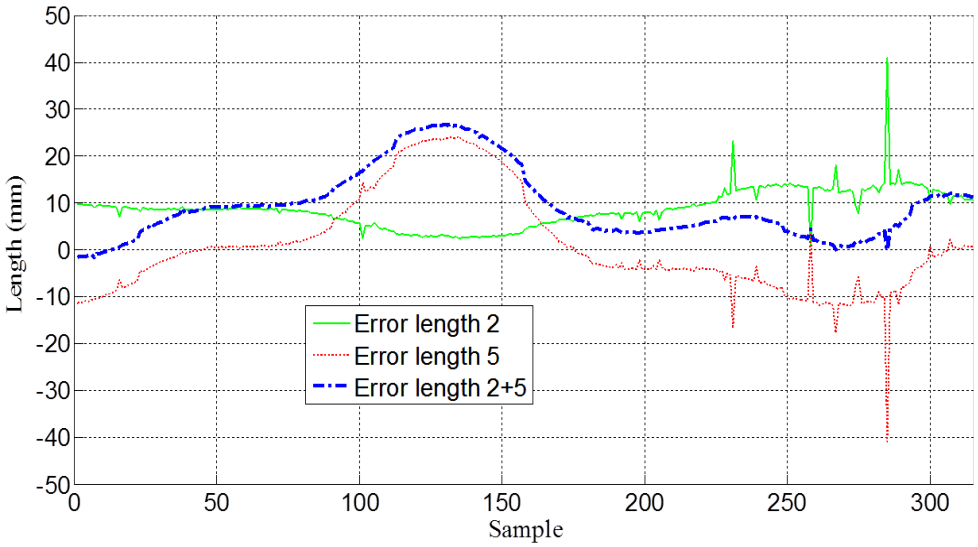

Figure 4.17: Error in lengths l_2, l_5 and l_{2+5}

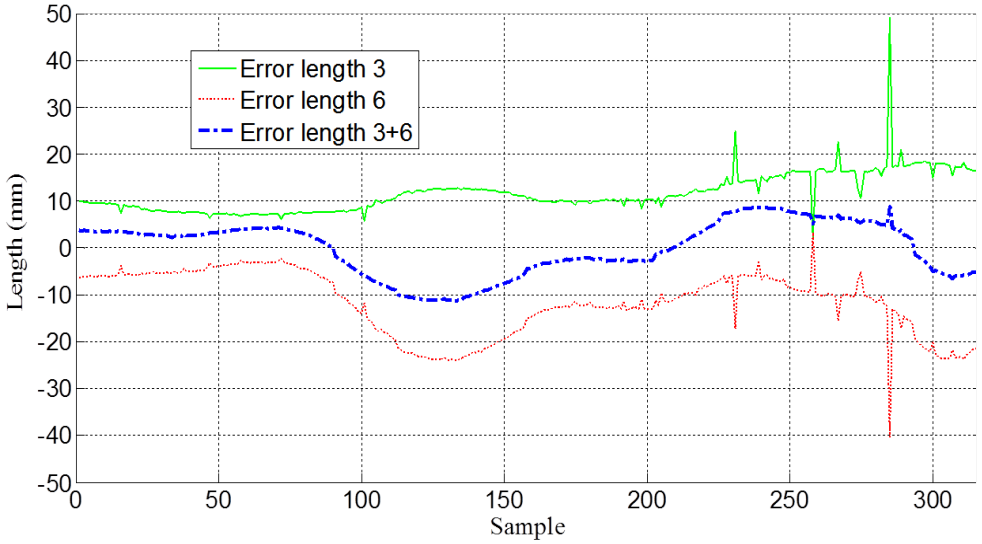

Figure 4.18: Error in lengths l_3, l_6 and l_{3+6}

© 2014 Tous droits réservés.

doc.univ-lille1.fr

Thèse de Coralie Escande, Lille 1, 2013

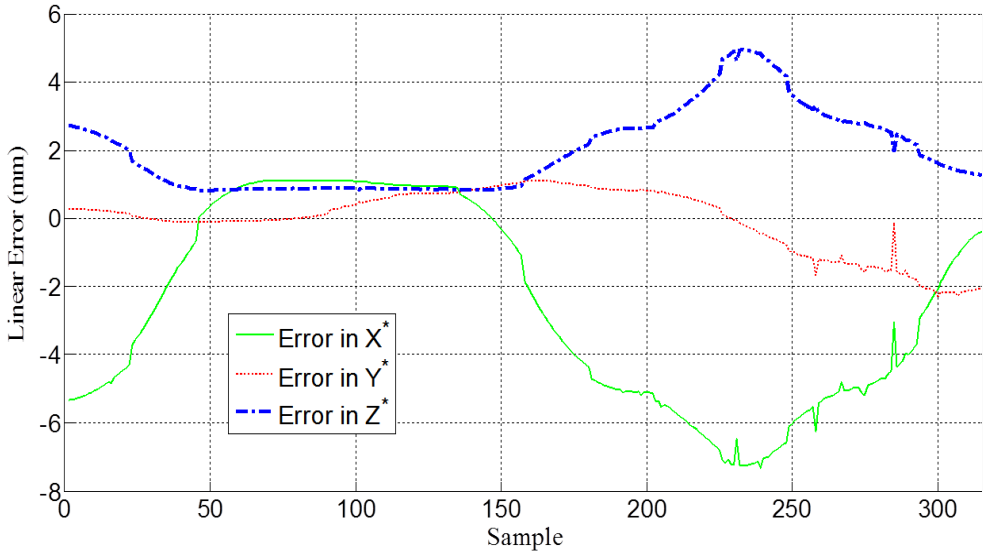

Figure 4.19: Linear error in estimated position (X^*, Y^*, Z^*)

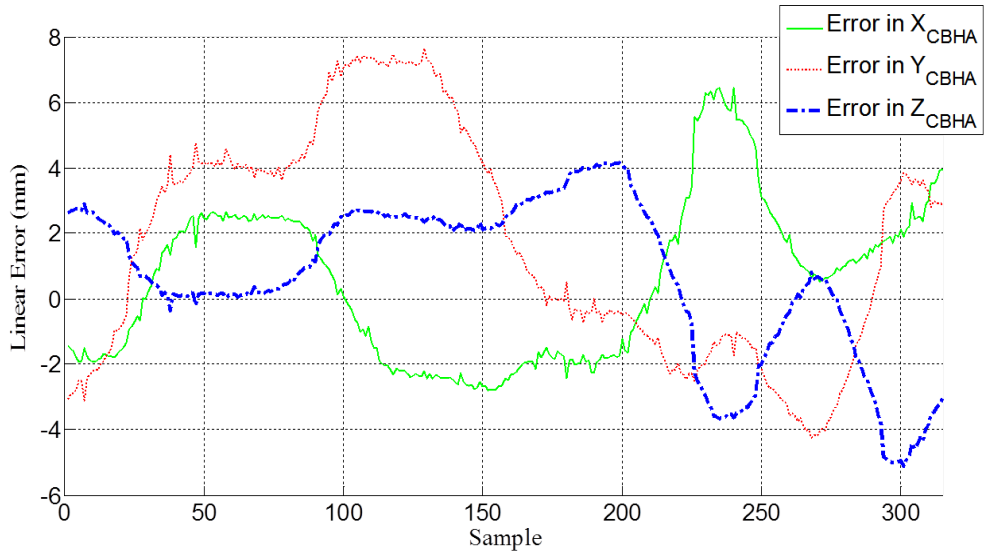

Figure 4.20: Linear error in estimated position $(X_{cbha}, Y_{cbha}, Z_{cbha})$

© 2014 Tous droits réservés.

doc.univ-lille1.fr

Thèse de Coralie Escande, Lille 1, 2013

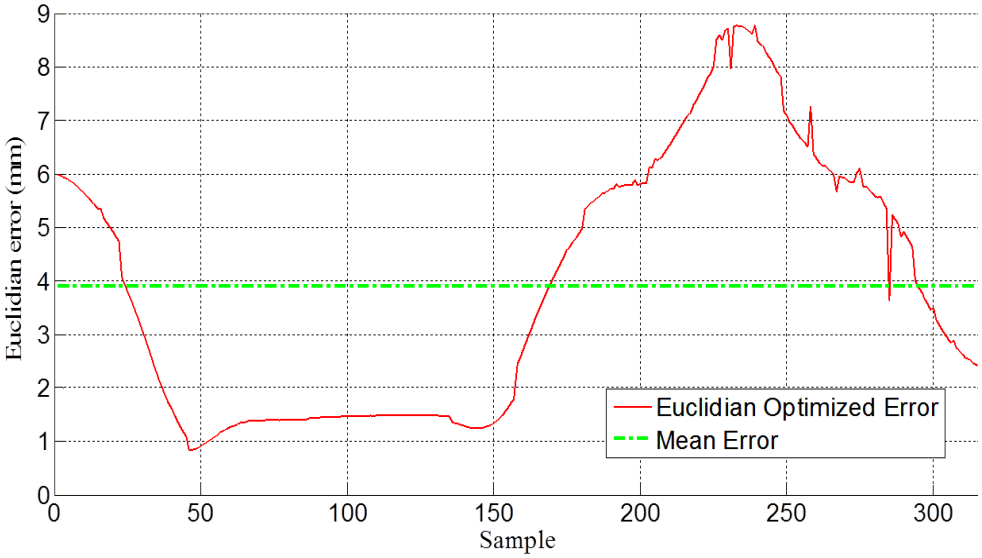

Figure 4.21: Euclidian optimized error (IKM)

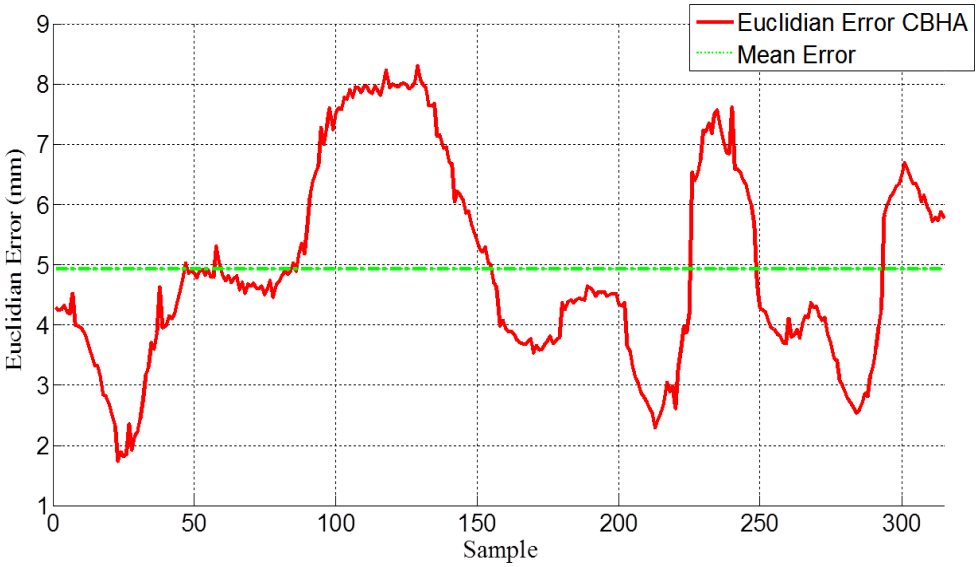

Figure 4.22: Euclidian estimated error (CBHA)

Figures 4.23 show the simulated workspace with the assumption of uniform curvature, by representing one unified section instead of two concatenated sections.

The figure 4.24 shows the workspace calculated with the assumption of uniform curvature, which indeed includes the trajectories from the experience with the industrial rigid manipulator validating the inverse kinematic model.

© 2014 Tous droits réservés.

doc.univ-lille1.fr

Thèse de Coralie Escande, Lille 1, 2013

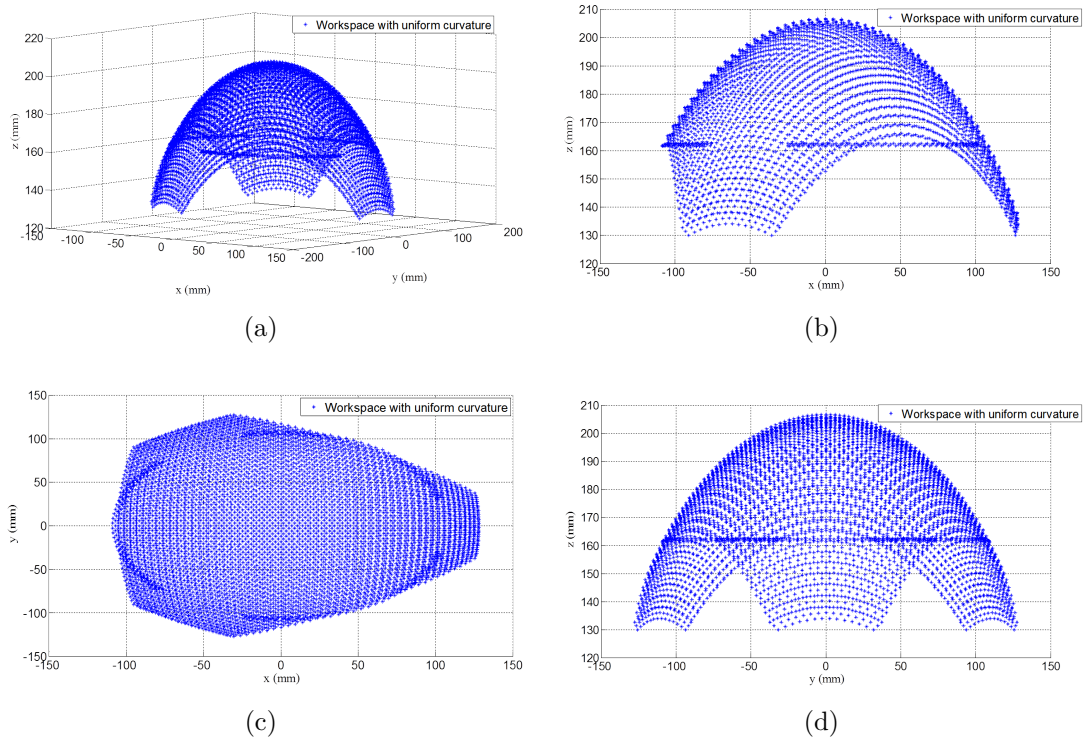

Figure 4.23: Several points of view of the simulated workspace with the assumption of uniform curvature: (a) 3D view, (b) view of the plane XZ, (c) view of the plane XY, (d) view of the plane ZY

© 2014 Tous droits réservés.

doc.univ-lille1.fr

Thèse de Coralie Escande, Lille 1, 2013

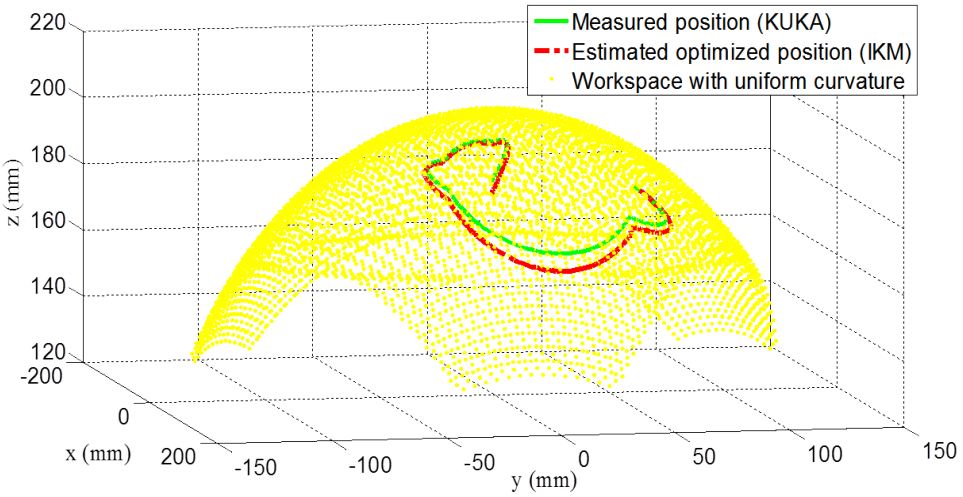

Figure 4.24: Measured and estimated position associated with workspace assuming uniform curvature

4.5.2 Discussion

It is noticed that an error of the tube lengths of millimeter can generate a position error of millimeters. The results show that the errors on the tube lengths of the first section are reported on the lengths of the tubes of the second section. This phenomenon is explained by the fact that the cable-potentiometers used to measure the second section lengths are encapsulating the first section. The calculation of the tube lengths of the second section is done by subtracting the total length of the tube with those of the first section. The accuracy of the optimized length is about 9 mm, comparing to the measured ones. This represents 4 % of the total length of both bending sections (205 mm).

In addition the inverse kinematic model takes into account the conic form of the CBHA by calculating each vertebra diameter, while the forward kinematic model supposes that each bending section is a cylinder, where the diameter of the first bending section is bigger than those of the second bending section. This assumption differentiation explains the error between the optimized Cartesian coordinates and the estimated ones.

It is also noticed that the Euclidian estimated error from the CBHA forward kinematic model reflects a worse accuracy than the results presented in chapter 3 after calibration. This can be explained by the fact that the shown trajectory represents the position of the tip of the second bending section in the Frame placed on the basis of the first bending section. This means that only 2 calibrated constant parameters are used: the diameter of the 2 bending sections.

© 2014 Tous droits réservés.

doc.univ-lille1.fr

Thèse de Coralie Escande, Lille 1, 2013

Besides, the inverse kinematic model proposes a set of tubes lengths corresponding to an optimized posture minimizing the curvature variation and to a uniform curvature, as if there was a unique section. However,the trajectory being generated by the experiment of the industrial manipulator, does not necessarily lead to an optimized posture. During the trajectory, the CBHA curvature is sometimes not uniform, i.e. the curvature of the first bending section may be different from that of the second bending section. Thus, this phenomenon explains the different tubes lengths.

The simulated workspace obtained with the uniform curvature assumption is actually a subspace of the simulated workspace. This can be explained by the fact that the uniform curvature assumption reduces the number of DoF.

The trajectory, obtained with the industrial manipulator KUKA and used to validate the IKM, is effectively belonging to the simulated workspace obtained with the uniform curvature assumption, as expected[26]. It confirms thus the validation of the IKM.

Finally, impulses observed on the length's errors can be explained by the length's sensors noises owing to a friction effect between the wires of the wire-potentiometers and the CBHA.

4.6 Conclusion of the Chapter

In this chapter, the IKM of the CBHA has been developed, by assimilating the CBHA to a hybrid parallel robot. This IKM combines two methods : an algebraic method to model the vertebrae and an optimization method to model the CBHA. Indeed, after obtaining the analytical expression of the IKM of the CBHA vertebrae, it is noticed that there exist an infinite number of solutions to the CBHA IKM. To select the best solution, the IKM is formulated as a nonlinear optimization problem, solved with an SQP method under physical constraints to obtain an optimized posture, Minimizing the CBHA curvature and based on a set of selection criteria.

The experimental data from the test bench presented in the chapter 3 have been used to validate the IKM with an accuracy of 4 % of the total length of both bending sections (205 mm). Finally, the workspace of the CBHA has been defined in terms of physical limits and has been plotted with simulated and experimental data.

[26]In the experiment with the industrial manipulator KUKA, the movement is generated by KUKA, inducing thus an uniform curvature to the CBHA

© 2014 Tous droits réservés.

doc.univ-lille1.fr

Thèse de Coralie Escande, Lille 1, 2013

© 2014 Tous droits réservés.

doc.univ-lille1.fr

Thèse de Coralie Escande, Lille 1, 2013

Chapter 5

Toolbox Implementation

This chapter concerns the software development for both forward and inverse kinematic models necessary for the autonomous control of the CBHA using specialized simulation tools such as MATLAB/SIMULINK. It is therefore necessary to implement these models. This work has been realized in the framework of a master internship (Tcheussi 2013), based on the previously developed model written in m-file programs.

RobotinoXT is one of the Bionic Learning Network Projects of FESTO-DIDACTIC. Initially, it is manually controlled, arose the need to migrate towards full autonomous control of the Compact Bionic Handling Assistant (CBHA), the bionic arm of the RobotinoXT. This migration was to be done in part on MATLAB/SIMULINK which is an advanced and high performance control and automation tool.

This toolbox implementation requires accurate modeling of the complex bionic arm. Through its constant collaboration with educational and research institutions all over the world, FESTO is working hand in gloves with these institutions to achieve this goal. LAGIS is one of these privileged institutions. The collaboration with LAGIS gave rise to this PhD topic aimed at modeling the dynamics of the CBHA. The models obtained were written as M-scripts for computation and evaluation on MATLAB. However, these scripts have a number of drawbacks:

- They are not appropriate for large public of end-users: performance control and automation algorithms are most efficiently realized with SIMULINK, using dedicated blocks rather than scripts. Besides they enable usability of already-existing SIMULINK blocks.

- They are difficult to understand: a script is basically a computer program written in M-language and so not easy to understand. For a user who doesn't know about M-language, it might not be easy to follow up what is written

© 2014 Tous droits réservés.

doc.univ-lille1.fr

Thèse de Coralie Escande, Lille 1, 2013

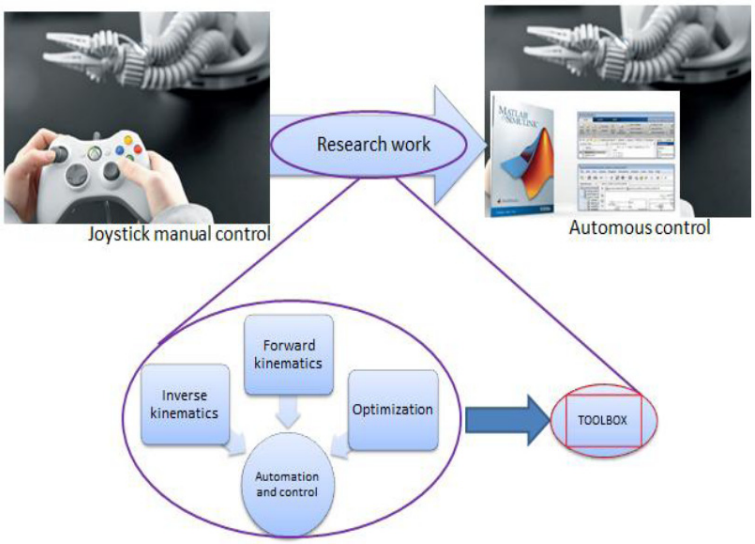

Figure 5.1: Imaged representation of the scope

in the code. All he is really interested in is that results should be put into easily usable end interface.

- They are not user friendly: A graphical user interface is always better understood than a set of instructions. Using scripts, user has to perform the tedious task of running them from the command window each time he wants to use the models. These scripts do not offer a straight forward means to present the valuable research work that has been realized.

- They are time inefficient: running multiple scripts from the command window means running them using another script which proves to be time consuming, especially in the case of multiple input data. Graphical blocks enable a rapid processing of inputs and an easy exploitation of results.

- Fastidious communication between models: imagine the output of the forward kinematics model written in a script, has to be used as inputs for the inverse kinematic model written in another script, we shall need to run at least two commands in the command window to realize this.

It was therefore necessary to create a toolbox containing SIMULINK blocks that implements the kinematic models obtained from research work in order to remedy to the above mentioned drawbacks.

© 2014 Tous droits réservés.

doc.univ-lille1.fr

Thèse de Coralie Escande, Lille 1, 2013

5.1 Main objectives

This work was aimed at producing a toolbox implementing the kinematic models of the CBHA established from research work. The designed toolbox was expected to have the same properties as other SIMULINK toolboxes present in the SIMULINK Library Browser. In greater details, it was supposed to meet the following objectives:

- Be accessible from the SIMULINK Library Browser;
- Contain blocks implementing the forward and inverse kinematic models of the CBHA;
- Contain blocks implementing necessary conversion such as the sensor voltages to corresponding sensor lengths and sensor voltages to corresponding pressures;
- Each block had to possess a help file accessible via the MATLAB Help Browser giving more details concerning the block;
- Contain examples showing how the blocks could be used in order to ensure rapid usage;
- Be as intuitive as possible.

5.2 Main Development

Besides requiring notions in programming, this work was also an instance of a development project. In this light, it was necessary to adopt a methodology that is appropriate to software development projects. In our case, the project's phases were inspired from the V-model (Wikipedia 2013a) and reformulated according to the steps illustrated in Figure 5.2.

Before starting to code, it was necessary to explore all available alternatives, offered by MATLAB, to create custom SIMULINK blocks. Thus, MATLAB offers panoply of ways to setup custom SIMULINK blocks, it was important to choose the most appropriate and optimal method that enables us to attain the aforementioned objectives. Some of them include the alternatives listed in Figure 5.3.

After a close comparison of custom block functionalities (MathsWorks 2013) resulting from different solutions, it came out that *Level-2 MATLAB S-function* (system-functions) represented the most appropriate alternative for the SIMULINK blocks. In a few words, an S-function is a computer language description of a

© 2014 Tous droits réservés.

doc.univ-lille1.fr

Thèse de Coralie Escande, Lille 1, 2013

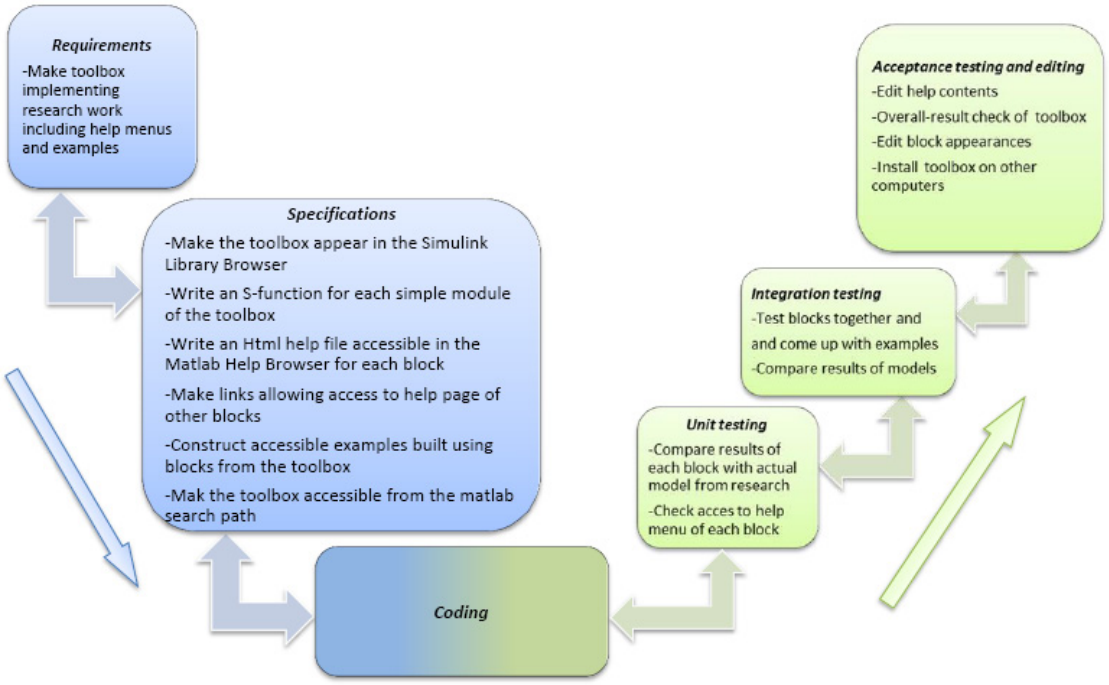

Figure 5.2: Major steps of the development of the CBHA modelling toolbox

Fcn	Apply specified expression to input
Interpreted MATLAB Function	Apply MATLAB function or expression to input
Level-2 MATLAB S-Function	Use Level-2 MATLAB S-function in model
MATLAB Function	Include MATLAB code in models that generate embeddable C code
S-Function	Include S-function in model
S-Function Builder	Create S-function from C code that you provide

Figure 5.3: Alternatives to creating custom SIMULINK blocks

© 2014 Tous droits réservés.

doc.univ-lille1.fr

Thèse de Coralie Escande, Lille 1, 2013

SIMULINK block written in MATLAB. This choice is supported for many reasons clearly explained on the Documentation Center of MathsWorks. However the key points to keep in mind are:

- S-function API enables an interaction with the SIMULINK;
- no code generation needed;
- multiple inputs and outputs supported;
- dynamic states supported;
- simple to put in place from the MATLAB scripts.

The greatest challenges were the addition of a library to the SIMULINK Library Browser, the insertion of the S-function call-back, which interacts with the MATLAB engine and the development based on HTML files the help menus of different blocks.

5.3 Creating the Individual SIMULINK Blocks

In order to create the toolbox, we begin by creating individual constituent SIMULINK blocks implementing research work results. The complete process of individual block creation used can be broken down into two major processes: placing the S-function in S-Function block and masking the resulting block.

5.3.1 Placing the S-Function in S-Function Block

As mentioned before, this was done using *Level-2 MATLAB S-function*. An algorithm can be implemented in an S-function by following a set of simple rules; one can implement an algorithm in an S-function and use the S-Function block to add it to a SIMULINK model. In this way, the *Level-2 MATLAB S-function* references the instance of the *Level-2 MATLAB S-function* block taken from *user-defined Functions library* in the SIMULINK Library Browser, as illustrated in Figure 5.4.

The *Level-2 MATLAB S-function* comprises a set of callback methods that the SIMULINK engine invokes when updating or simulating the model. The callback methods perform the actual work of initializing and computing the outputs of the block defined by the S-function and they determine the block attributes and behaviour. They are therefore chosen according to specific requirements.

However a *Level-2 MATLAB S-function* must include the following callback methods:

© 2014 Tous droits réservés.

doc.univ-lille1.fr

Thèse de Coralie Escande, Lille 1, 2013

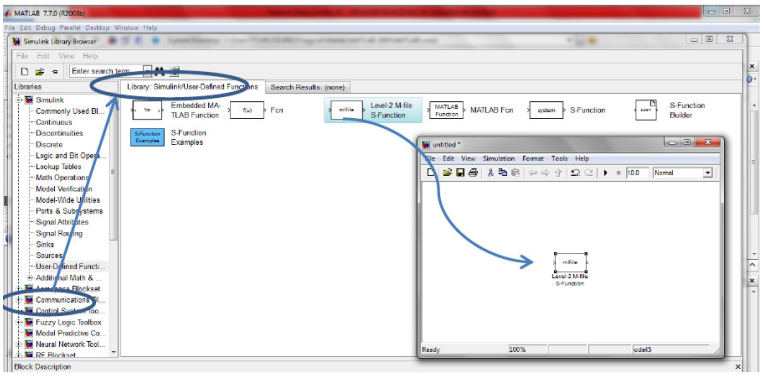

Figure 5.4: Inserting a Level-2 M-file S-Function block in a model

- A “Setup” function to initialize the basic S-function characteristics;
- An “Outputs” function to calculate the S-function outputs.

The S-function begins with the name of the function followed by an invocation of the setup methods. The setup method in turn contains a number of callback methods. In our case, we used the following callback methods to implement the models of the CBHA:

1. the run-time object “NumInputPorts” and “NumOutputPorts” properties in order to initialize one input port and one output port;
2. the run-time object “SetPreCompInpPortInfoToDynamic” and “SetPreCompOutPortInfoToDynamic” methods to indicate that the input and output ports inherit their compiled properties (dimensions, data type, complexity, and sampling mode) from the model;
3. the run-time object “NumDialogPrms” in order to initialize one S-function dialog parameter if necessary;
4. the run-time object “SampleTimes” property to specify the sampling time of the S-function;
5. the run-time object “RegBlockMethod” method to register callback methods used in the S-function.

In our case, we register the following callback functions:

- Outputs: This is the most important callback method. Through this method, we compute outputs and affect them to the output ports. This method gives

© 2014 Tous droits réservés.

doc.univ-lille1.fr

Thèse de Coralie Escande, Lille 1, 2013

us the possibility to type in the function that computes the value of the output or simply to reference an existing M-function. In our case we use the second alternative.

- Terminates: This method performs a set of actions, such as freeing of memory, that must be performed when the simulation is terminated or when a S-function block is destroyed.

Other important callback methods which could be used in the case for implementing the optimized inverse kinematics model include:

- PostPropagationSetup which is required whenever we need to initialize the number of DWork vectors and the attributes of each vector. A DWork vector should be used in an S-function instead of global or static memory to store instance-specific values of S-function variables;
- InitializeConditions which is required to set values for the DWork vector initiated in the PostPropagationSetup method;
- CheckParameters which verifies new parameter settings whenever parameters change or are re-evaluated during a simulation.

After typing the S-function, we insert it into the *Level-2 MATLAB S-function* block, as shown in Figure 5.5.

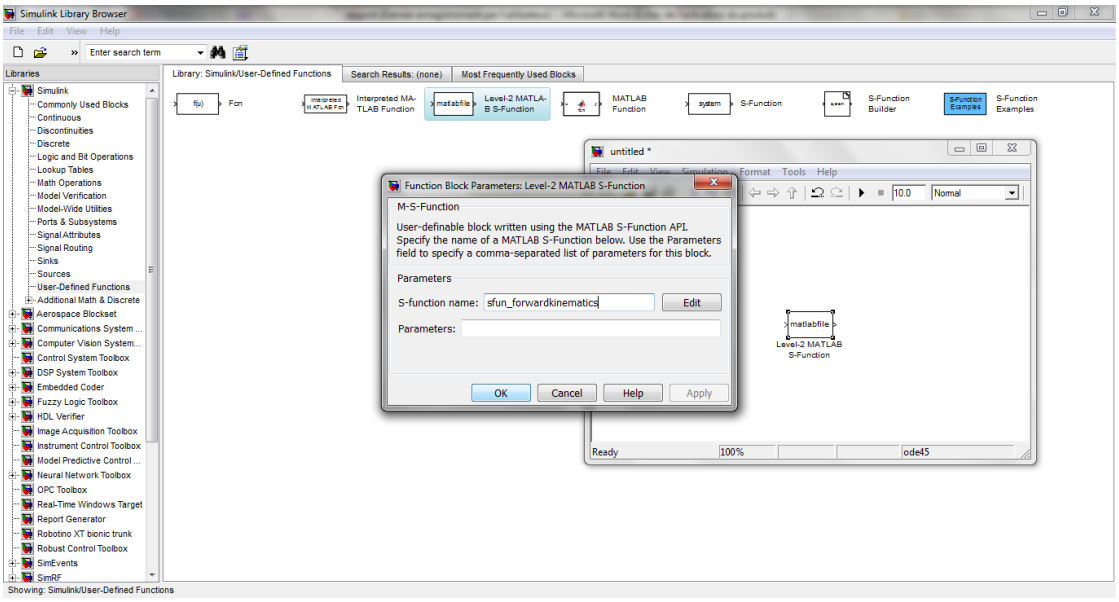

Figure 5.5: Putting the S-function into the Level-2 M-file S-function block

© 2014 Tous droits réservés.

doc.univ-lille1.fr

Thèse de Coralie Escande, Lille 1, 2013

Once this is done the block appearance is edited to have the number of inputs and output ports stipulated in the S-function and carry the same name, as illustrated in Figure 5.6.

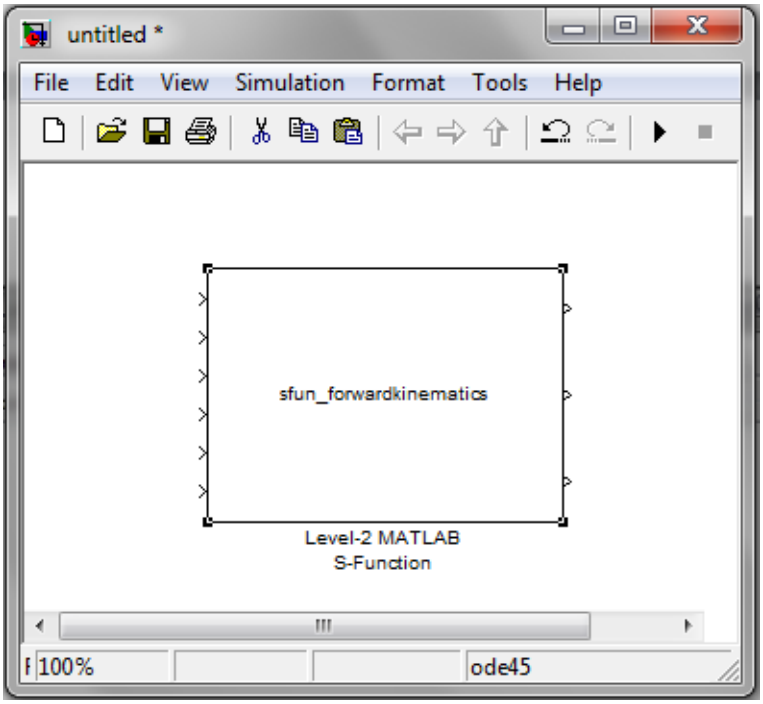

Figure 5.6: Appearance of the block after putting the S-function

At this stage of development, we can customize the user interface using masking, as pictured in Figure 5.7. This process enabled us to add an HTML help to each block.

Among existing tabbed panes offered by the Mask Editor, we only used, the Icon & Ports and Documentation panes during the masking: the first (Icon & Ports) was used to label the ports using the "*port_label*" function and to add an image to the block using the *image(imread('imagename.ext'))* function as shown in Figure 5.8.

Adding a help menu to each block represented a very important objective of this work as it was going to enable a new user to know about the blocks present in the toolbox. This was done using the Documentation pane of the Mask editor.

For the forward kinematics model of the CBHA, the Figure 5.9 gives an example of help block.

The option "helpbrowser" added to the web command in the *mask help* field imposes this HTML help file to be opened in the MATLAB help browser as intended (see Figure 5.10).

© 2014 Tous droits réservés.

doc.univ-lille1.fr

Thèse de Coralie Escande, Lille 1, 2013

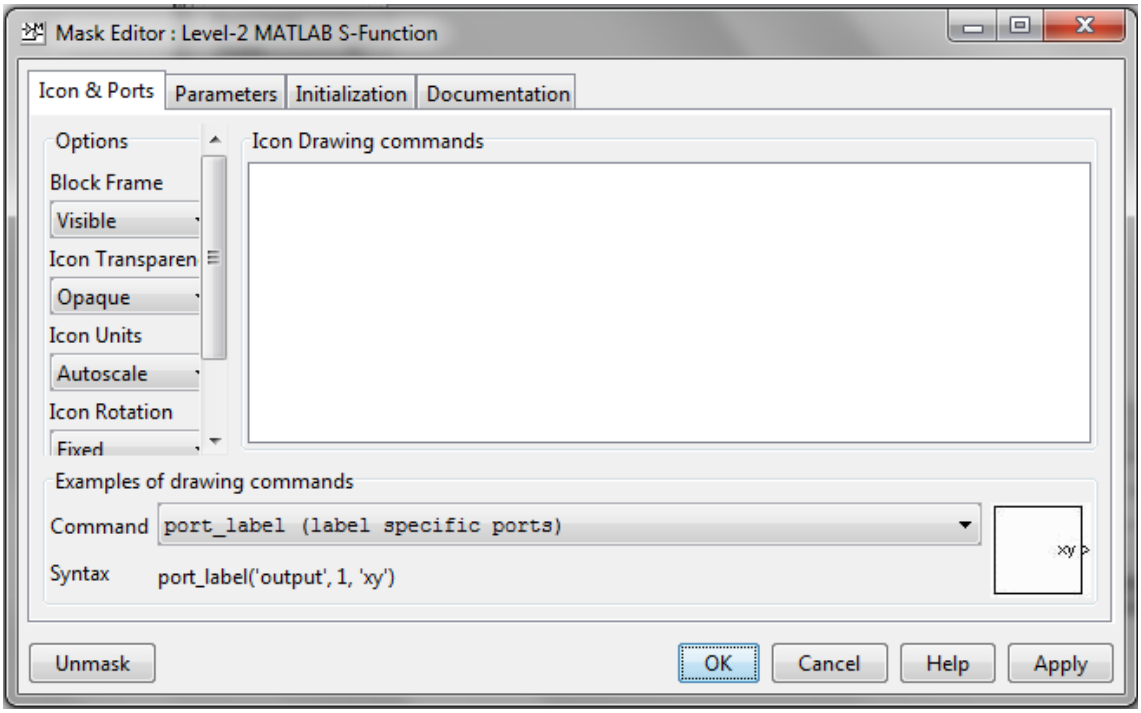

Figure 5.7: Dialogue box of mask editor

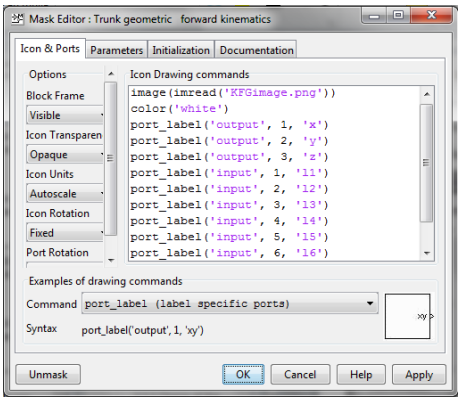

Figure 5.8: Masking dialogue box

© 2014 Tous droits réservés.

doc.univ-lille1.fr

Thèse de Coralie Escande, Lille 1, 2013

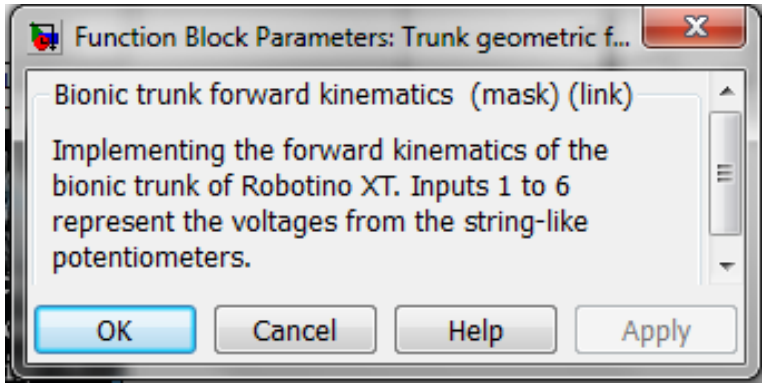

Figure 5.9: Example of help for the CBHA forward kinematic model

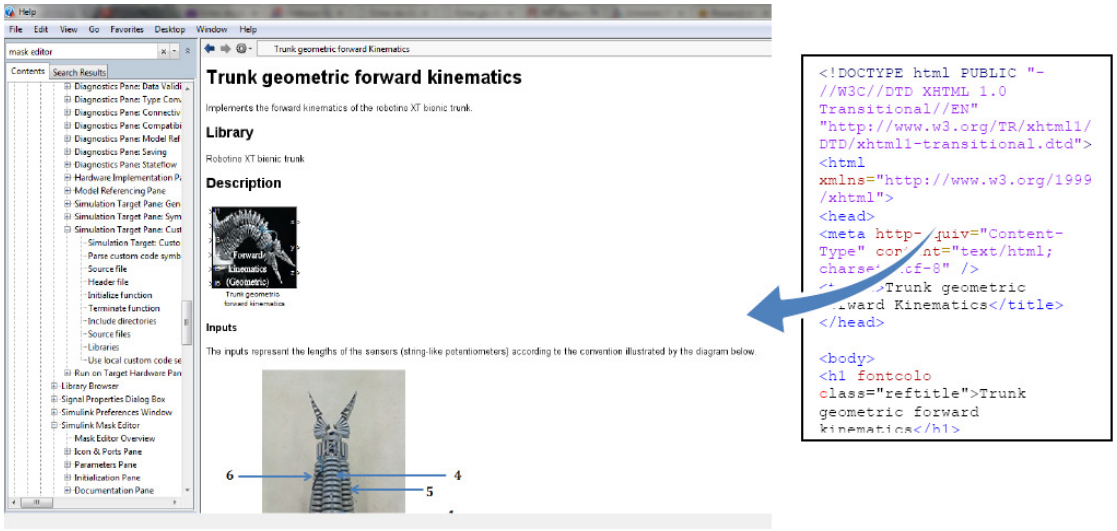

Figure 5.10: The opened help file

© 2014 Tous droits réservés.

Thèse de Coralie Escande, Lille 1, 2013

There is a generic structure adopted for each help file: it begins with the block name, the library to which it belongs, an image of it, the ranges of input and outputs values and ends with links towards help files of other blocks of the toolbox and examples. These help files also precise input value ranges to be guaranteed to satisfy inherent assumptions of kinematic models.

5.3.2 Putting Blocks in Library and Making Accessible from the SIMULINK Library Browser

The individual blocks had to be put together to constitute the toolbox. Five main blocks were created: the trunk geometric forward kinematics, the trunk neural network forward kinematics, the trunk neural network inverse kinematics, the "*volttometer*" block and the "*volttopressure*" blocks. The second and the third blocks were created, based on a research work on a qualitative approach for kinematic modeling of the CBHA. This is used to compare the developed quantitative approach of modeling presented in this PhD thesis. In order to do this, a library was created named "*RobotinoXTlibrary*", given by Figure 5.11.

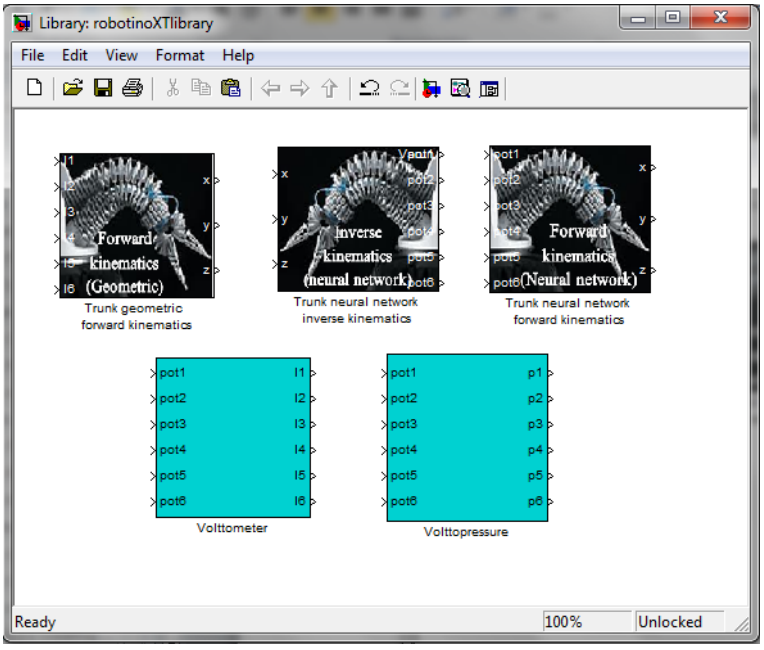

Figure 5.11: RobotinoXT library

The designed library had to be made to appear in the SIMULINK Library Browser. This was done using an "*slblock*" M-function script. This defines the block library for a specific Toolbox or Blockset and it returns information to

© 2014 Tous droits réservés.

doc.univ-lille1.fr

Thèse de Coralie Escande, Lille 1, 2013

SIMULINK in the form of a "*BlocksetStruct*". The SIMULINK Library Browser needs to know which libraries in your Blockset it should show, and what names to give them. To provide this information, define an array of Browser data structures with one array element for each library to display in the SIMULINK Library Browser. When this file is executed, we find the RobotinoXT toolbox appears in the SIMULINK Library Browser as Figure 5.12.

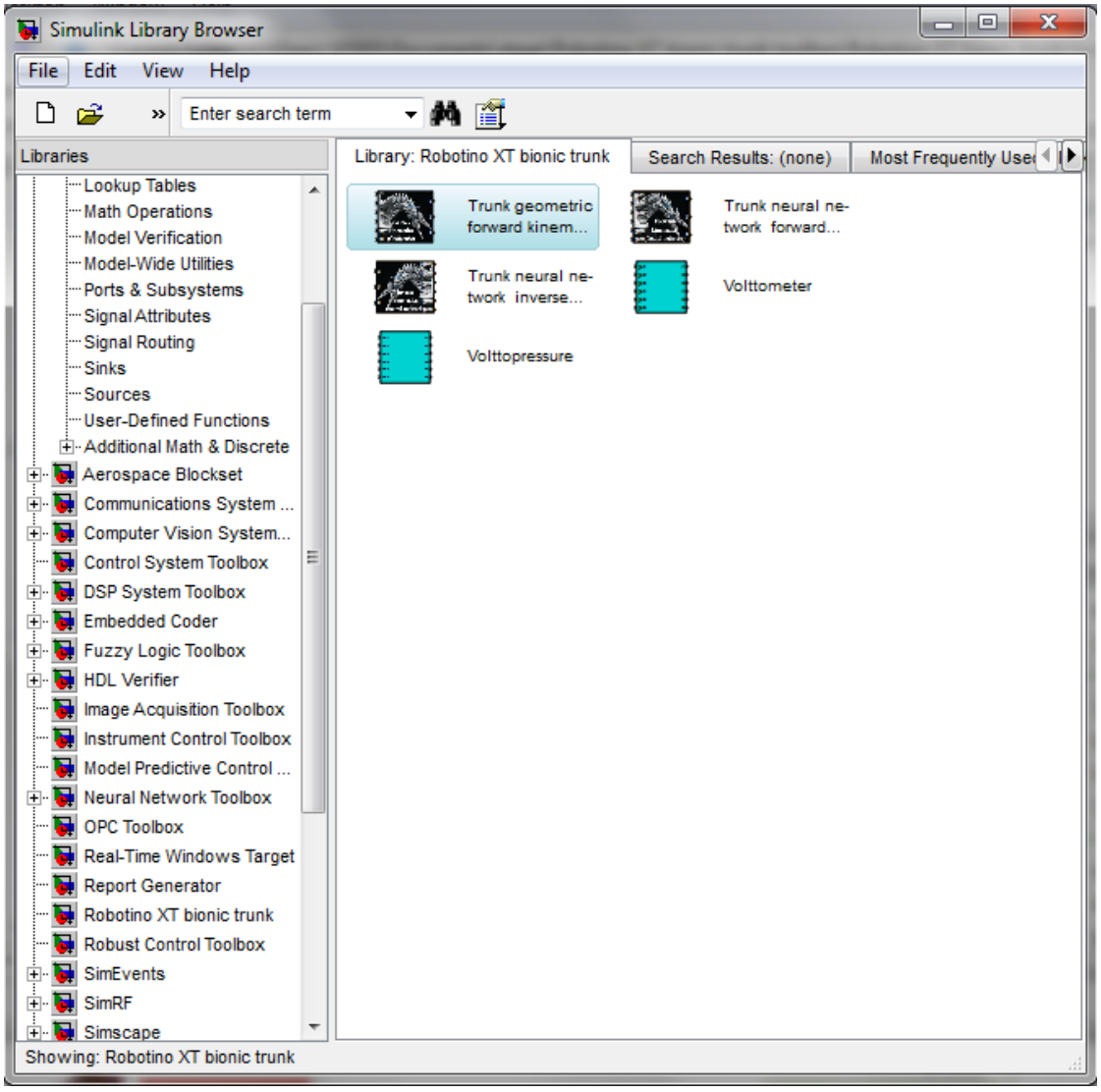

Figure 5.12: RobotinoXT bionic trunk toolbox in the SIMULINK Library Browser

In order to make this toolbox and all the elements it contains to always be accessible by the MATLAB engine, we add it to the MATLAB search path.

© 2014 Tous droits réservés.

doc.univ-lille1.fr

Thèse de Coralie Escande, Lille 1, 2013

5.4 Tests and Validation

After coming up with individual blocks, we started doing tests by sending inputs into an individual block implementing a given model, namely the forward kinematics model, and comparing the results with those obtained by running the m-file of the same model. We obtained that the results were exactly the same. Beyond, getting equal results, we tested the help menu and made sure all the hyper-links functioned properly. We then proceeded with integrated tests of various blocks, by interconnecting them together. These tests were conducted using sensor voltages obtained for a given trajectory of the CBHA. These examples are accessed from MATLAB by typing: *open_system('name_of_example')* in the command window or by opening it directly from the *@example* folder. Each example begins with a brief summary of what the example is about. We came up with two examples as presented below:

5.4.1 Geometric and Neural Network Forward Kinematic Models

The example of Figure 5.13 implements the forward kinematic model calculated with two different methods : the geometric method (quantitative approach) presented in the previous chapter and a neural network method (qualitative approach) developed by a PhD student of the same laboratory. It compares results from both models using databases collected from the test bench mentioned in the previous chapter. We don't have used the measured pose of the CBHA tip, because the entire purpose of this work is to estimate the pose from the tubes lengths. But good enough, we have two approaches that were used, so we can compare both. That might not prove them right but will go a long way to support their correctness. This example is named *FKtest* for Forward kinematics test and can be accessed from command window after installing the toolbox by typing *open_system('FKTest')* or directly from its folder, where the result is obtained as illustrated in Figure 5.13. This example implements the neural network and the forward kinematic model of the CBHA. The results from both models are then compared.

5.4.2 The "*Volttopressure*" Model

The robot is controlled based on pressure actuation system and the command signal is generally a voltage. Knowing what voltage corresponds to what pressure is inescapable for appropriate control of the robot. Here, the sensor voltages and corresponding pressures are obtained directly from the robot. So sensor voltages are used as inputs to the "*volttopressure*" block and pressures from this block are compared to initial pressures corresponding to these sensor voltages. Since this

© 2014 Tous droits réservés.

doc.univ-lille1.fr

Thèse de Coralie Escande, Lille 1, 2013

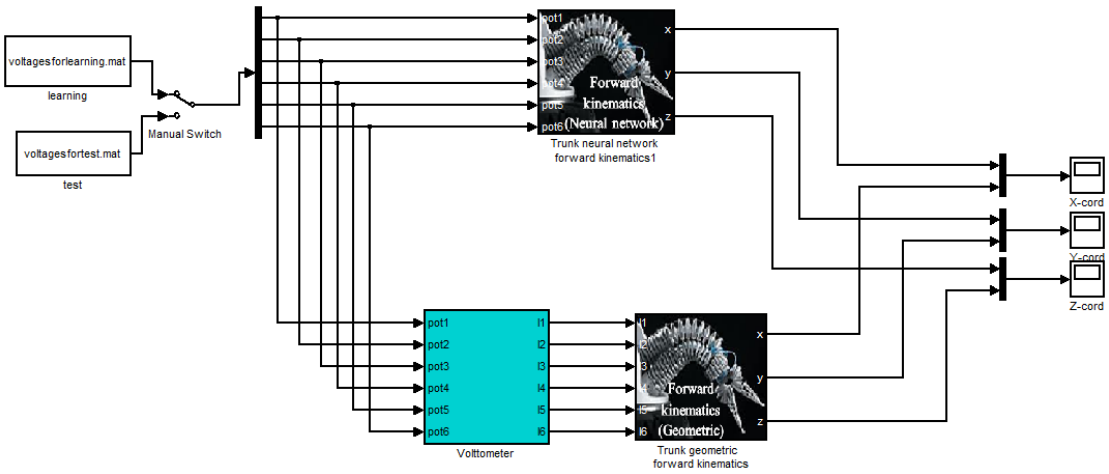

Figure 5.13: Setup of Forward Kinematic example

was based on a neural network approach, there was need for learning databases and validation databases (Melingui et al. 2014), collecting measured pressures and voltages. Finally, the databases are shown in Figure 5.14.

This example is named *voltopressure* and can be accessed from command window after installing the toolbox by typing *open_system('volttopressure')* or directly from the *@example* folder.

5.5 Conclusion of the Chapter

This chapter illustrated the detailed process of how the CBHA toolbox for kinematic modelling was implemented. The final purpose of this toolbox is to enable the migration of the actual manually controlled CBHA to a full autonomously controlled CBHA of the robot RobotinoXT. Besides the optimized inverse kinematic model of the CBHA is still under refinement and will soon be added as an update of the present toolbox.

© 2014 Tous droits réservés.

doc.univ-lille1.fr

Thèse de Coralie Escande, Lille 1, 2013

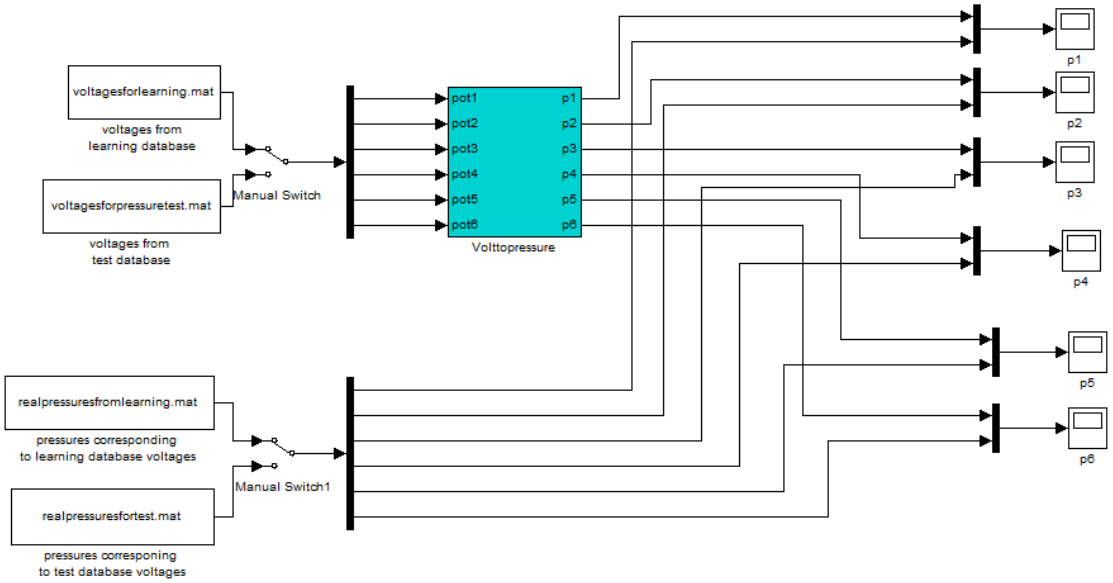

Figure 5.14: Setup of Conversion example

© 2014 Tous droits réservés.

doc.univ-lille1.fr

Thèse de Coralie Escande, Lille 1, 2013

© 2014 Tous droits réservés.

doc.univ-lille1.fr

Conclusion

In this thesis, we proposed a new kinematic calibration method for quantitative forward modeling of the CBHA. This was done through an "arc-geometry" model-based method, applied to two bending sections. This calibration used the experimental data corresponding to the cartesian coordinates of the CBHA tip, generated from external coupling-guidance from a rigid industrial manipulator robot. This experience showed that the model accuracy improved significantly in presence of parameter and modeling uncertainties. Due to the non-linearity of the kinematic parameters of the CBHA, namely the curvature radius, shape and the memory of the main constitutive material of the CBHA, some errors still exist.

The proposed test-bench for the calibration was very helpful to optimize the kinematic parameters identification of this complex bionic arm. The comparison between this test-bench and another one, based on the trilateration principle, showed its significant performances in terms of stability and accuracy. This calibration technique can be generalized to a long version of the CBHA or similar continuum and hyper-redundant robots.

The other contribution in this work was the synthesis of the inverse kinematic model of the CBHA. This was obtained after assimilating the succession of the constitutive vertebrae of the CBHA by a concatenation of rigid platforms, composed by parallel-serial robots. The inverse kinematic model of each platform can be deduced analytically, while their placement on the supported axis is obtained using an optimization algorithm. This optimization allowed the estimation of the inter-vertebra lengths, using only the cartesian coordinates of the CBHA tip. After obtaining these lengths, a reconstruction of the posture of the CBHA is deduced and compared to its experimental posture. The obtained results showed a convergence with maximum 4 % length error on the global posture, realized for specific trajectories.

Finally, a workspace of the whole bionic arm is obtained based on experimental and simulated data. The experimental data used for designing the workspace are collected from the external robot-guided system, while those of the simulation are obtained from the forward kinematic model. This workspace identification is now helpful to generate trajectories for robot control in the simulation environment

© 2014 Tous droits réservés.

doc.univ-lille1.fr

Thèse de Coralie Escande, Lille 1, 2013

before real implementation.

The CBHA is a complex non-linear system, where the elaboration of accurate models running in real-time becomes a real challenge.

With the actual advance of this Ph.D. work, the mobile platform of the RobotinoXT is not used in the determination of the whole robot kinematic model. Also, the control strategy elaboration of the RobotinoXT is not yet developed for the autonomous navigation.

Future Work

According to the obtained results of the kinematic modeling process of the CBHA, the following perspective contributions should be developed and compared:

1. Extension of the forward and kinematic models to the omni-drive mobile platform for the RobotinoXT. This is important for trajectory tracking and obstacle avoidance of the whole robot according to the center of the tool located at the arm gripper;

2. Development of qualitative methods for kinematic modeling of hyper-redundant robot of the CBHA. These data-learning approaches can be helpful for tracking control of well-known trajectories. The association of both qualitative and quantitative modeling methods can improve the control of the RobotinoXT in large covered workspace with high accuracy.

3. Dynamic modeling of the CBHA from two points of view:

   (a) firstly, energetic studies using Bond Graph based approach to perform the monitorability and the reconfigurability of the system in the case of faulty or disturbing situations, mainly from the existing pneumatic behavioral actuation;

   (b) secondly, for a real-time 3D simulation design based on finite-element method, which is an interesting new research topic started from a recent collaboration of SHACRA (Simulation in Healthcare using Computer Research Advances) from INRIA Nord Europe [27].

[27] http://www.inria.fr/en/teams/shacra

© 2014 Tous droits réservés.

doc.univ-lille1.fr

Bibliography

Aldebaran (Oct. 2013). *Website of the company Aldebaran*. visited on 15 October 2013. URL: http://www.aldebaran-robotics.com/fr/.

Allgower, E. E. L. and K. Georg (2003). *Introduction to numerical continuation methods*. Vol. 45. SIAM.

Anscombe, R., A. Bryant, R. Buckingham, G. Ferguson, A. Graham, M. Lichon, N. Parry, P. Brandrick, M. Redman, M. Summers, and B. Green (2006). "Snake-arm robots: a new approach to aircraft assembly". In: *AMAF*.

Anscombe, R., R. Buckingham, A. Graham, N. Parry, M. Lichon, and G. Ferguson (June 2006). "Snake-arm Robots Conduct Nuclear Maintenance". In: *IYNC*, pp. 246.1–246.9.

ASIMOV (June 2013a). *Landshark UGV Arm*. visited on 10 June 2013. URL: http://www.asimovrobotics.com/more.php?robot=landshark_arm.

— (Sept. 2013b). *Website of the company ASIMOV Robotics*. visited on 17 september 2013. URL: www.asimovrobotics.com.

Bai, S. and C. Xing (2012). "Shape modeling of a concentric-tube continuum robot". In: *Robotics and Biomimetics (ROBIO), 2012 IEEE International Conference on*. IEEE, pp. 116–121.

Bailly, Y., Y. Amirat, and G. Fried (2011). "Modeling and control of a continuum style microrobot for endovascular surgery". In: *Robotics, IEEE Transactions on* 27.5. Ed. by IEEE, pp. 1024–1030.

Barclay, A., P. E. Gill, and J. B. Rosen (1997). *SQP Methods and their application to numerical optimal control*. Report NA97-3. San Diego: Dep. of mathematics, University of California,

Bartow, A., A. Kapadia, and I. D. Walker (2013). "A Novel Continuum Trunk Robot Based on Contractor Muscles". In: *Int. Conf. on Signal Processing, Robotics, and Automation. Recent Advances in Circuits, Communications and Signal Processing*. Ed. by WSEAS, pp. 181–86. ISBN: 978-1-61804-164-7.

Batlle, J. A. and A. Barjau (2009). "Holonomy in mobile robots". In: *Robotics and Autonomous Systems* 57.4, pp. 433–440. ISSN: 0921-8890. DOI: 10.1016/j.robot.2008.06.001. URL: http://www.sciencedirect.com/science/article/pii/S0921889008000833.

© 2014 Tous droits réservés.

doc.univ-lille1.fr

Thèse de Coralie Escande, Lille 1, 2013

Behrens, R., M. Poggendorf, E. Schulenburg, and N. Elkmann (2012). "An Elephant's Trunk-Inspired Robotic Arm - Trajectory Determination and Control". In: *Robotics; Proceedings of ROBOTIK 2012; 7th German Conference on*, pp. 1–5.

BionicPower (June 2013). *Website of the company BionicPower*. visited on 10 June 2013. URL: http://www.bionic-power.com/app_military.html.

Bishop, R. L. (1975). "There is more than one way to frame a curve". In: *The American Mathematical Monthly* 82, pp. 246–251. URL: http://www.jstor.org/stable/2319846.

Buchberger, B. (1988). "Applications of Gröbner bases in non-linear computational geometry". In: *Trends in computer algebra*. Springer, pp. 52–80.

Chen, G., M. T. Pham, and T. Redarce (2009a). "Sensor-based guidance control of a continuum robot for a semi-autonomous colonoscopy". In: *Robotics and autonomous systems* 57.6. Ed. by Elsevier, pp. 712–722.

— (2009b). "Sensor-based guidance control of a continuum robot for a semi-autonomous colonoscopy". In: *Robotics and Autonomous Systems* 57, pp. 712–722.

Cheng, H. and K.C. Gupta (1991). "A study of robot inverse kinematics based upon the solution of differential equations". In: *Journal of Robotic Systems* 8.2. Ed. by Wiley Online Library, pp. 159–175.

Chibani, A., T. Chettibi, R. Merzouki, C. Mahfoudi, and A. Zaatri (2013). "Generating Optimal Reference kinematic configurations for hyper-redundant parallel robots".

Chibani, A., C. Mahfoudi, T. Chettibi, and R. Merzouki (2013). "Conceptual Study of a class of hybrid-redundant robot".

Chirikjian, G. S. and J. W. Burdick (1994). "A modal approach to hyper-redundant manipulator kinematics". In: *Robotics and Automation, IEEE Transactions on* 10.3, pp. 343–354. DOI: 10.1109/70.294209.

In-Chul, H. (2008). "Kinematic parameter calibration method for industrial robot manipulator using the relative position". English. In: *Journal of Mechanical Science and Technology* 22 (6), pp. 1084–1090. ISSN: 1738-494X. DOI: 10.1007/s12206-008-0305-0.

Cowan, L. S. and I. D. Walker (2012). "The Importance of Continuous and Discrete Elements in Continuum Robots". In: *International Journal of Advanced Robotic Systems* 10, pp. 165–2013. DOI: 10.5772/55270. URL: http://www.intechopen.com/journals/international_journal_of_advanced_robotic_systems/the-importance-of-continuous-and-discrete-elements-in-continuum-robots.

Dennis, J. J. E. and R. B. Schnabel (1983). *Numerical methods for unconstrained optimization and nonlinear equations*. Vol. 16. Siam.

© 2014 Tous droits réservés.

doc.univ-lille1.fr

Thèse de Coralie Escande, Lille 1, 2013

Durand, C. and C. M. Hoffmann (2000). "A systematic framework for solving geometric constraints analytically". In: *Journal of Symbolic Computation* 30.5. Ed. by Elsevier, pp. 493–519.

Eichhorn, M., C. Ament, and T. T. Nguyen (Dec. 2009). "Modelling of the 4-Axis Kinematic Manipulator AirArm Driven by Pneumatic Muscle Actuators". In: *IEEE International Conference on Control and Automation*, pp. 1301–1307.

EksoBionics (June 2013). *Website of the company Ekso Bionics*. visited on 10 June 2013. URL: http://www.eksobionics.com/.

Escande, C., R. Merzouki, P. M. Pathak, and V. Coelen (Dec. 2012). "Geometric Modelling of Multisection Bionic Manipulator: Experimental Validation on RobotinoXT". In: *IEEE International Conference on Robotics and Biomimetics (ROBIO)*.

Escande, C., P. M. Pathak, R. Merzouki, and V. Coelen (Dec. 2011). "Modelling of Multisection Bionic Manipulator: application to RobotinoXT". In: *IEEE International Conference on Robotics and Biomimetics (ROBIO)*, pp. 92–97.

Festo (May 2013a). *Bionic Learning Network*. visited on 28 May 2013. URL: http://www.festo.com/cms/en_corp/9785.htm.

— (May 2013b). *Bionic Projects of Festo*. visited on 28 May 2013. URL: http://www.festo.com/cms/en_corp/9617.htm.

— (2013c). *Brochure of BHA*. visited on 25 October 2013. URL: http://www.festo.com/net/SupportPortal/Files/42050/Brosch_FC_BHA_3_0_EN_lo.pdf.

— (2013d). *Brochure of RobotinoXT*. visited on 15 September 2013. URL: http://www.festo.com/net/SupportPortal/Files/46266/Brosch_robotinoXT_en_RZ_110311_lo_einzel.pdf.

— (2013e). *Brochure of the robot BionicOpter*. visited on 16 September 2013. URL: http://www.festo.com/net/SupportPortal/Files/248133/Festo_BionicOpter_en.pdf.

— (2013f). *Brochure of the robot SmartBird*. visited on 17 September 2013. URL: http://www.festo.com/net/SupportPortal/Files/46270/Brosch_SmartBird_en_8s_RZ_300311_lo.pdf.

— (May 2013g). *Website of the company Festo*. visited on 28 May 2013. URL: www.festo.com.

— (May 2013h). *Website of the Festo subsidiary : Festo-Didactic*. visited on 28 May 2013. URL: www.Festo-didactic.com.

Fletcher, R. (1987). *Practical methods of optimization*. Wiley Interscience Publication.

Gelareh, S., R. Merzouki, K. McGinley, and R. Murray (2013). "Scheduling of Intelligent and Autonomous Vehicles under pairing/unpairing collaboration strategy

© 2014 Tous droits réservés.

doc.univ-lille1.fr

Thèse de Coralie Escande, Lille 1, 2013

in container terminals". In: *Transportation Research Part C: Emerging Technologies* 33. Ed. by Elsevier, pp. 1–21.

Giri, N. and I. D. Walker (2010). "Continuum robots and underactuated grasping". In: *Mechanical Sciences* 2, pp. 51–58.

Godage, I. S., E. Guglielmino, D. T. Branson, G. A. Medrano-Cerda, and D. G. Caldwell (Sept. 2011). "Novel Modal Approach for Kinematics of Multisection Continuum Arms". In: *IEEE/RSJ International Conference on Intelligent Robots and Systems*, pp. 1093–1098.

Goldenberg, A., B. Benhabib, and R. Fenton (1985). "A complete generalized solution to the inverse kinematics of robots". In: *Robotics and Automation, IEEE Journal of* 1.1. Ed. by IEEE, pp. 14–20.

Gu, Z., I. Yamamoto, and T. Hiratsuka (2013). "Research on Bio-mechanism Robotics by Robotic Fish Fin Technology". In: *Intelligent Autonomous Systems 12*. Springer, pp. 577–584.

Guillot, A. and J.-A. Meyer (2008). *La bionique, quand la science imite la nature*. Dunod. DOI: ISBN978-2-10-050635-4.

Haga, Y., T. Mineta, W. Makishi, T. Matsunaga, and M. Esashi (2010). "Active Bending Catheter and Endoscope Using Shape Memory Alloy Actuators". In: *InTech*. Ed. by Corneliu Cismasiu. URL: http://www.intechopen.com/books/shapememory-alloys/active-bending-catheter-and-electric-endoscope-using-shape-memory-alloy.

Hannan, M. H. and I. D. Walker (2003). "Kinematics and the implementation of an elephant's trunk manipulator and other continuum style robots". In: *Journal of Robotics Systems* 20.2, pp. 45–63. DOI: 10.002/rob.10070.

Hannan, M. H. and I.D. Walker (July 2001). "The 'Elephant Trunk' Manipulator, Design and Implementation". In: *IEEE/ASME International Conference on Advanced Intelligent Mechatronics Proceedings*, pp. 14–19.

Hanson, A. J. (1998). *Quaternion Gauss Maps and Optimal Framings of Curves and Surfaces*.

Hanson, A. J. and H. Ma (1995). "Parallel transport approach to curve framing". In: *Indiana University, Techreports-TR425* 11, pp. 3–7.

Hartenberg, R. S. and J. A. Denavit (1955). "A kinematic notation for lower pair mechanisms based on matrices". In: *Journal of Applied Mechanics* 77, pp. 215–221.

Hernandez-Martinez, E. E., C. S. Lopez-Cajun, and J. C. Jauregui-Correa (2010). "Calibration of Parallel Manipulators and their Application to Machine Tools. A State of the Art Survey". In: *Ingenieria Investigacion y Tecnologia* 11.2, pp. 141–154. DOI: ISSN1405-7743FI-UNAM.

HiBot (June 2013). *Website of the company HiBot*. visited on 10 June 2013. URL: http://hibot.co.jp/HiBotCorpProfileL.pdf.

© 2014 Tous droits réservés.

doc.univ-lille1.fr

Thèse de Coralie Escande, Lille 1, 2013

Hollerbach, J. and C. Wampler (1996). "The calibration index and taxonomy for robot kinematic calibration methods". In: *The International Journal of Robotics Research* 15, pp. 573–591.

Ibrahim, O. and W. Khalil (2007). "Kinematic and dynamic modeling of the 3-RPS parallel manipulator". In: *Proc. 12th IFToMM World Congress*.

Iida, F. and C. Laschi (2011). "Soft Robotics: Challenges and Perspectives". In: *Procedia Computer Science* 7. Ed. by Elsevier, pp. 99–102.

Iqbal, S., S. Mohammed, and Y. Amirat (Dec. 2009). "A guaranteed approach for kinematic analysis of continuum robot based catheter". In: *International Conference on Robotics and Biomimetics (IEEE ROBIO)*, pp. 1573–1578.

Jones, B. A., W. McMahan, and I. D. Walker (2004). "Design and analysis of a novel pneumatic manipulator". In: *IFAC*.

Jones, B. A. and I. D. Walker (2005). "A new approach to Jacobian formulation for a class of multi-section continuum robots". In: *Robotics and Automation, 2005. ICRA 2005. Proceedings of the 2005 IEEE International Conference on*. IEEE, pp. 3268–3273.

— (Feb. 2006a). "Kinematics for Multisection Continuum Robots". In: *IEEE Transactions on Robotics* 22.1, pp. 43–55.

— (Dec. 2006b). "Practical Kinematics for Real-Time Implementation of Continuum Robots". In: *IEEE Transactions on Robotics* 22.6, pp. 1087–1099. DOI: 10.1109/TRO.2006.886268.

— (Oct. 2006c). "Three-Dimensional Modeling and Display of Continuum Robots". In: *IEEE/RSJ International Conference on Intelligent Robots and Systems*.

— (Apr. 2007). "Limiting-case Analysis of Continuum Trunk Kinematics". In: *IEEE International Conference on Robotics and Automation*, pp. 1363–1368.

Karacan, M. K. and B. Bükcü (2010). "On Natural ccurvature of Bishop Frame". In: *Journal of vectorial relativity JVR* 5, pp. 34–41.

Kesner, S. B. and R. D. Howe (2011). "Force control of flexible catheter robots for beating heart surgery". In: *Robotics and Automation (ICRA), 2011 IEEE International Conference on*. IEEE, pp. 1589–1594.

Khalil, W. and E. Dombre (1999). *Modélisation identification et commande des robots*. Ed. by Hermès Science Publications. Hermès Science Publications.

Khalil, W., R. Merzouki, B. Ould-Bouamama, and H. Haffaf (2012). "Hypergraph Models for System of Systems Supervision Design". In: *IEEE Transactions on Systems, Man, and Cybernetics, Part A* 42.4. Ed. by IEEE, pp. 1005–1012.

Kim, S., C. Laschi, and B. Trimmer (2013). "Soft robotics: a bioinspired evolution in robotics". In: *Trends in biotechnology* 31.5. Ed. by Elsevier, pp. 287–294. URL: http://dx.doi.org/10.1016/j.tibtech.2013.03.002.

© 2014 Tous droits réservés.

doc.univ-lille1.fr

Thèse de Coralie Escande, Lille 1, 2013

Krajník, T., V. Vonásek, D. Fišer, and J. Faigl (2011). "AR-drone as a platform for robotic research and education". In: *Research and Education in Robotics-EUROBOT 2011*. Springer, pp. 172–186.

K-Team (2002). *Khepera^2 user manual*. URL: http://ftp.k-team.com/khepera/documentation/Kh2UserManual.pdf.

— (July 2013). *Website of the company K-Team Mobile Robotic*. visited on 17 July 2013. URL: http://www.k-team.com/mobile-robotics-products/khepera-iii.

Kuka (2013). *Website of the Kuka youBot store*. visited on 18 July 2013. URL: http://www.youbot-store.com/.

Kumar, P., R. Merzouki, B. O. Bouamama, and H. Haffaf (2013). "Microscopic Traffic Dynamics and Platoon Control Based on Bond Graph Modeling". In: *16th international IEEE conference on intelligent transport systems (ieee-itsc13)*.

LAGIS (June 2013). *Website of the research laboratory LAGIS - UMR CNRS 8219*. visited on 30 June 2013. URL: http://lagis.cnrs.fr/Presentation-du-LAGIS.

Laschi, C., B. Mazzolai, V. Mattoli, M. Cianchetti, and P. Dario (2009). "Design of a biomimetic robotic octopus arm". In: *Bioinspiration & Biomimetics* 4.1. Ed. by IOP Publishing, p. 015006. DOI: 10.1088/1748-3182/4/1/015006.

Lauwers, T. B., G. A. Kantor, and R. L. Hollis (2006). "A dynamically stable single-wheeled mobile robot with inverse mouse-ball drive". In: *Robotics and Automation, 2006. ICRA 2006. Proceedings 2006 IEEE International Conference on*, pp. 2884–2889. DOI: 10.1109/ROBOT.2006.1642139.

Lauwers, T., G. Kantor, and R. Hollis (Oct. 2005). "One is Enough !" In: *Proc. Int'l. Symp. for Robotics Research*. San Francisco.

Lee, C. S. G. and M. Ziegler (1984). "Geometric approach in solving inverse kinematics of PUMA robots". In: *Aerospace and Electronic Systems, IEEE Transactions on* 6. Ed. by IEEE, pp. 695–706.

Li, C. and C. D. Rahn (2002). "Design of continuous backbone, cable-driven robots". In: *Journal of Mechanical Design* 124. Ed. by ASME, pp. 265–271. DOI: 10.1115/1.1447546.

Li, Z. and R. Du (2013). "Design and Analysis of a Bio-Inspired Wire-Driven Multi-Section Flexible Robot". In: *Int J Adv Robotic Sy* 10.209.

Liljebäck, P., K. Y. Pettersen, Ø. Stavdahl, and J. T. Gravdahl (2012). "A review on modelling, implementation, and control of snake robots". In: *Robotics and Autonomous Systems* 60.1. Ed. by Elsevier, pp. 29–40.

Ma, C., D. Liu, Z. Shi, and Z. Zhang (2012). "A flexible new method to improve the accuracy of SMA self-sensing control". In: *Mechatronics and Automation (ICMA), 2012 International Conference on*. Ed. by IEEE, pp. 1490–1495. DOI: 10.1109/ICMA.2012.6284357.

© 2014 Tous droits réservés.

doc.univ-lille1.fr

Thèse de Coralie Escande, Lille 1, 2013

Mahl, T., A. Hildebrandt, and O. Sawodny (2012). "Forward Kinematics of a compliant pneumatically actuated redundant manipulator". In: *Industrial Electronics and Applications (ICIEA), 2012 7th IEEE Conference on*. Ed. by IEEE, pp. 1267–1273. DOI: 10.1109/ICIEA.2012.6360917.

Mahl, T., A. E. Mayer, A. Hildebrandt, and O. Sawodny (2013). "A variable curvature modeling approach for kinematic control of continuum manipulators". In: *American Control Conference (ACC), 2013*. IEEE, pp. 4945–4950.

Majarena, A. C., J. Santolaria, D. Samper, and J. J. Aguilar (2010). "An Overview of Kinematic and Calibration Models Using Internal/External Sensors or Constraints to Improve the Behavior of Spatial Parallel Mechanisms". In: *Sensors* 10.11, pp. 10256–10297.

Mämpel, J., R. Eisold, W. Kempf, C. Schilling, and H. Witte (2009). "Lecture Notes in Control and Information Sciences". In: ed. by Krzysztof R. Kozlowski. Vol. 396. Springer London. Chap. A Modular Concept for a Biologically Inspired Robot, pp. 391–400. DOI: 10.1007/978-1-84882-985-5_36.

Manocha, D. and J. F. Canny (1992). "Real time inverse kinematics for general 6R manipulators". In: *Robotics and Automation, 1992. Proceedings., 1992 IEEE International Conference on*. IEEE, pp. 383–389.

Mao, S., E. Dong, S. Zhang, M. Xu, and J. Yang (2013). "A new soft bionic starfish robot with multi-gaits". In: *Advanced Intelligent Mechatronics (AIM), 2013 IEEE/ASME International Conference on*. IEEE, pp. 1312–1317.

Martinez, J. L., A. Mandow, J. Morales, S. Pedraza, and A. García-Cerezo (2005). "Approximating Kinematics for Tracked Mobile Robots". In: *The International Journal of Robotics Research* 24.10, pp. 867–878. DOI: 10.1177/0278364905058239. URL: http://ijr.sagepub.com/content/24/10/867.abstract.

Martinez, R. V., J. L. Branch, C. R. Fish, L. Jin, R. F. Shepherd, R. Nunes, Z. Suo, and G. M. Whitesides (2013). "Robotic Tentacles with Three-Dimensional Mobility Based on Flexible Elastomers". In: *Advanced Materials* 25.2. Ed. by Wiley Online Library, pp. 205–212.

MathsWorks (June 2013). *Comparison of Custom Block Functionality*. visited on 1 June 2013. URL: http://www.mathworks.fr/fr/help/simulink/ug/comparison-of-custom-block-functionality.html.

Mattar, E. (2013). "A survey of bio-inspired robotics hands implementation : New directions in dexterous manipulation". In: *Robotics and Autonomous Systems* 61. Ed. by Elsevier, pp. 517–544. DOI: 10.1016/j.robot.2012.12.005.

Meggiolaro, M., G. Scriffignano, and S. Dubowsky (2002). "Analysis and Optimization of Closed-Loop Manipulator Calibration with Fixed Endpoint". In: *Proceedings of the CONEM 2002 - National Mechanical Engineering Congress, ABCM*.

© 2014 Tous droits réservés.

doc.univ-lille1.fr

Thèse de Coralie Escande, Lille 1, 2013

Melingui, A., N. Benoudjit, B. Daachi, R. Merzouki, C. Escande, and J. B. Mbede (2014). "Qualitative approach for inverse kinematic modeling of a Compact Bionic Handling Assistant trunk". In: *In press : submitted paper to ICRA14 conference*.

Merzouki, R., B. Conrard, P. Kumar, and V. Coelen (2013). "Model based tracking control using Jerky behavior in platoon of vehicles". In: *European Control Conference (ECC)*, pp. 3488–3493.

Merzouki, R., A. K. Samantaray, P. M. Pathak, and B. O. Bouamama (2013). "Intelligent Transportation Systems". In: *Intelligent Mechatronic Systems*. Springer, pp. 769–867.

Microepsilon (2013). *Website of Microepsilon*. visited on 08 september 2013. URL: `http://www.micro-epsilon.com`.

Miller, G. (1999). *S5 Snake Robot Prototype*. visited on 18 September 2013. URL: `http://www.snakerobots.com/S5.html`.

Mintenbeck, J. and R. Estana (2010). "Design, modelling and control of a hyper-redundant 3-RPS parallel mechanism". In: *Robotics and Biomimetics (ROBIO), 2010 IEEE International Conference on*. IEEE, pp. 591–596.

Mooring, B. W., Z. S. Roth, and M. R. Driels (1991). *Fundamentals of manipulator calibration*. Ed. by Inc. John Wiley & Sons. A Wiley-Interscience Publication.

Mori, M., K. Suzumori, S. Wakimoto, T. Kanda, M. Takahashi, T. Hosoya, and E. Takematu (2010). "Development of power robot hand with shape adaptability using hydraulic McKibben muscles". In: *Robotics and Automation (ICRA), 2010 IEEE International Conference on*. Ed. by IEEE, pp. 1162–1168.

Neppalli, S., M. A. Csencsits, B. A. Jones, and I. D. Walker (2009). "Closed-Form Inverse Kinematics for Continuum Manipulators". In: *Advanced Robotics* 23, pp. 2077–2091.

Neumann, D., D. Bechert, et al. (1993). "Technologieanalyse bionik". In: *Analyse und Bewertung zukünftiger Technologien*. Ed. by V.-T. im Auftrag des BMBFT, p. 123.

Nocedal, J. and S. J. Wright (2006). *Numerical Optimization*. Ed. by Peter Glynn and Stephen M. Robinson. Springer Series in Operations Research.

OCRobotics (June 2013). *Website of the company OCRobotics*. visited on 10 June 2013. URL: `http://www.ocrobotics.com`.

Otake, M., Y. Kagami, M. Inaba, and H. Inoue (2000). "Behavior of a Mollusk-Type Robot Made of Electro-Active Polymer Gel under Spatially Varying Electric Fields". In: *Intelligent Autonomous Systems* 6, pp. 686–691.

Ottobock (June 2013). *Website of the company Ottobock*. visited on 10 June 2013. URL: `http://www.ottobock.fr/`.

© 2014 Tous droits réservés.

doc.univ-lille1.fr

Thèse de Coralie Escande, Lille 1, 2013

Paul, R. P. (1981). *Robot manipulators: mathematics, programming, and control: the computer control of robot manipulators*. The MIT Press series in artificial intelligence.

Pfeifer, R., M. Lungarella, and F. Iida (2012). "The challenges ahead for bio-inspired 'soft' robotics". In: *Communications of the ACM* 55.11. Ed. by ACM, pp. 76–87.

Pieper, D. L. (1968). "The kinematics of manipulators under computer control". PhD thesis. DTIC Document, Stanford University.

Powell, M. J. (1984). "Algorithm for non-linear constraints that use Lagrangian functions". In: *Mathematical programming* 14, pp. 224–248.

Quinet, J.-F. and P. Maurine (2012). "Etalonnage des robots industriels". In: *Techniques de l'ingénieur Robotique* base documentaire : TIB398DUO.ref. article : s7733. URL: `http://www.techniques-ingenieur.fr/base-documentaire/mesures-analyses-th1/robotique-42398210/etalonnage-des-robots-industriels-s7733/`.

Raghavan, M. and B. Roth (1990). "Kinematic analysis of the 6R manipulator of general geometry". In: *Proc. Fifth Int. Symposium on Robotics Research, MIT Press, Cambridge*.

Rao, R. S., A. Asaithambi, and S. K. Agrawal (1998). "Inverse kinematic solution of robot manipulators using interval analysis". In: *Journal of Mechanical Design* 120, p. 147.

Ritt, J. F. (1966). *Differential algebra*. Vol. 33. AMS Bookstore.

Robinson, G. and J. B. C. Davies (1999). "Continuum Robots - A State of the Art". In: *International Conference on Robotics and Automation (ICRA)* 4, pp. 2849–2854. DOI: `10.1109/ROBOT.1999.774029`.

Rolf, M. (2012). "Goal Babbling for an Efficient Bootstrapping of Inverse Models in High Dimensions". PhD thesis. Bielefeld University. URL: `http://pub.uni-bielefeld.de/publication/2551092`.

Rolf, M. and J. J. Steil (2012). "Constant curvature continuum kinematics as fast approximate model for the Bionic Handling Assistant". In: *Intelligent Robots and Systems (IROS), 2012 IEEE/RSJ International Conference on*. IEEE, pp. 3440–3446.

Roper, D.T., S. Sharma, R. Sutton, and P. Culverhouse (2011). "A review of developments towards biologically inspired propulsion systems for autonomous underwater vehicles". In: *Proceedings of the Institution of Mechanical Engineers, Part M: Journal of Engineering for the Maritime Environment* 225.2. Ed. by SAGE Publications, pp. 77–96.

Roth, Z. S., B. W. Mooring, and B. Ravani (1987). "An Overview of Robot Calibration". In: *IEEE Journal of Robotics and Automation* 3, pp. 377–385.

© 2014 Tous droits réservés.

doc.univ-lille1.fr

Thèse de Coralie Escande, Lille 1, 2013

Rucker, D. C. (2011). "The mechanics of continuum robots: Model-based sensing and control". PhD thesis. Faculty of the Graduate School of Vanderbilt University. URL: http://etd.library.vanderbilt.edu/available/etd-10042011-115347/unrestricted/dissertation.pdf.

Rucker, D. C., B. A. Jones, and R. J. Webster (Oct. 2010). "A Geometrically Exact Model for Externally Loaded Concentric-Tube Continuum Robots". In: *IEEE Transactions on Robotics* 26.5, pp. 769–780.

Sabetian, P., A. Feizollahi, F. Cheraghpour, and S. A. A. Moosavian (2011). "A compound robotic hand with two underactuated fingers and a continuous finger". In: *Safety, Security, and Rescue Robotics (SSRR), 2011 IEEE International Symposium on*. IEEE, pp. 238–244.

Salmon, G. (1885). *Lessons introductory to the modern higher algebra*. fourth edition. Hodges, Figgis, and Co.

Salomon, O. and A. Wolf (2012). "Inclined Links Hyper-Redundant Elephant Trunk-Like Robot". In: *Journal of Mechanics and Robotics* 4. Ed. by ASME.

Sanan, S. and C. G. Atkeson (2011). "A continuum approach to safe robots for physical human interaction". In: *Symposium on Quality of Life Technology*.

Schittkowski, K. (1980). *Nonlinear Programming Codes (Lecture Notes in Economics and Mathematical Systems)*. Vol. 183. Springer.

— (2002). *Numerical Data Fitting in Dynamical Systems*. Kluwer Academic Publishers.

— (2003). *DFNLP : A Fortran implementation of an SQP-Gauss-Newton algorithm - user's guide*. Report. Department of Mathematics, University of Bayreuth.

Sciavicco, L. and B. Siciliano (2000). "Modelling and Control of Robot Manipulators". In: *Measurement Science and Technology* 11.12. Ed. by IOP Publishin, p. 1828.

Sfakiotakis, M., A. Kazakidi, N. Pateromichelakis, and D. P. Tsakiris (2013). "Octopus-inspired Eight-arm Robotic Swimming by Sculling Movements". In: *IEEE International Conference on Robotics and Automation (ICRA 2013)*, pp. 5135–5141.

Siciliano, B. and W. Khatib (2009). *Handbook of Robotics*. Springer. DOI: ISBN978-3-540-23957-4.

Siegwart, R. and I. R. Nourbakhsh (2004). *Introduction to Autonomous Mobile Robots*. Ed. by A Bradford Book. The MIT Press.

Simaan, N. (Apr. 2005). "Snake-Like Units Using Flexible Backbones and Actuation Redundancy for Enhanced Miniaturization". In: *IEEE International Conference on Robotics and Automation*, pp. 3012–3017.

Spong, M. W., S. Hutchinson, and M. Vidyasagar (2006). *Robot modeling and control*. Wiley. DOI: ISBN978-0-471-64990-8.

© 2014 Tous droits réservés.

doc.univ-lille1.fr

Thèse de Coralie Escande, Lille 1, 2013

Sreenath, K., H.-W. Park, I. Poulakakis, and J. W. Grizzle (2013). "Embedding active force control within the compliant hybrid zero dynamics to achieve stable, fast running on MABEL". In: *The International Journal of Robotics Research* 32.3. Ed. by SAGE Publications, pp. 324–345.

Stokes, A. A., R. F. Shepherd, S. A. Morin, F. Ilievski, and G. M. Whitesides (2013). "A Hybrid Combining Hard and Soft Robots". In: *Soft Robotics* 1.1. Ed. by Inc. Mary Ann Liebert, pp. 70–74. DOI: 10.1089/soro.2013.0002.

Takuma, T., S. Hayashi, and K. Hosoda (Sept. 2008). "3D Bipedal Robot with Tunable Leg Compliance Mechanism for Multi-modal Locomotion". In: *IEEE/RSJ International Conference on Intelligent Robots and Systems*, pp. 1097–1102.

Tcheussi, B. (2013). *Robotino XT Bionic Trunk Toolbox*. 4th year internship report. Electrical and computer engineering Department, Polytech'Lille.

TouchBionics (June 2013). *Website of the company Touch Bionics*. visited on 10 June 2013. URL: http://www.touchbionics.com/about/.

Trivedi, D., C. D. Rahn, W. M. Kier, and I. D. Walker (Sept. 2008). "Soft robotics: Biological inspiration, state of the art, and future research". In: *Applied Bionics and Biomechanics* 5, pp. 99–117.

Vavourakis, V., D. Bampasakis, A. Kazakidi, N. Pateromichelakis, J. A. Ekaterinaris, and D. P. Tsakiris (2012). "Generation of primitive behaviors for nonlinear hyperelastic octopus-inspired robotic arm". In: *Biomedical Robotics and Biomechatronics (BioRob), 2012 4th IEEE RAS & EMBS International Conference on*. IEEE, pp. 725–730.

Wada, M. and S. Mori (1996). "Holonomic and omnidirectional vehicle with conventional tires". In: *Robotics and Automation, 1996. Proceedings., 1996 IEEE International Conference on*. Vol. 4, pp. 3671–3676. DOI: 10.1109/ROBOT.1996.509272.

Walker, I. D. (2013a). "Robot strings: Long, thin continuum robots". In: *Aerospace Conference, 2013 IEEE*. IEEE, pp. 1–12.

— (June 2013b). *Videos proceeding*. visited on 10 June 2013. URL: http://www.ces.clemson.edu/~iwalker/videos.html.

Walker, I. D., C. Carrerras, R. McDonnell, and G. Grimes (2006). "Extension versus Bending for Continuum Robots". In: *International Journal of Advanced Robotic Systems* 3.2, pp. 171–178.

Wampler, C. W. (1986). "Manipulator inverse kinematic solutions based on vector formulations and damped least-squares methods". In: *Systems, Man and Cybernetics, IEEE Transactions on* 16.1. Ed. by IEEE, pp. 93–101.

Weber, R.-C. and M. Bellenberg (2010). *Robotino Manual*. Ed. by Festo Didactic GmbH & Co. Denkendorf, Germany. URL: http://www.festo-didactic.com/ov3/media/customers/1100/544305_robotino_deen2.pdf.

© 2014 Tous droits réservés.

doc.univ-lille1.fr

Thèse de Coralie Escande, Lille 1, 2013

Webster, R. J. and B. A. Jones (June 2010). "Design and Kinematic Modeling of Constant Curvature Continuum Robots: A Review". In: *The International Journal of Robotics Research* 29.13, pp. 1661–1683. DOI: 10.1177/0278364910368147. URL: http://ijr.sagepub.com/content/29/13/1661.

Whitney, D. E. (1969). "Resolved motion rate control of manipulators and human prostheses". In: *Man-Machine Systems, IEEE Transactions on* 10.2. Ed. by IEEE, pp. 47–53.

Wikipedia (June 2013a). *V-Model (software development)*. visited on 1 June 2013. URL: http://en.wikipedia.org/wiki/V-Model_(software_development).

— (May 2013b). *Wikipedia, Robotics Rules*. visited on 28 May 2013. URL: http://en.wikipedia.org/wiki/Three_Laws_of_Robotics.

Ye, C., G. Lv, S. Ma, and H. Ni (2012). "Development of a variable parallelogram tracked mobile robot". In: *Robotics and Biomimetics (ROBIO), 2012 IEEE International Conference on*. IEEE, pp. 2156–2160.

Yu, L., L. Zhang, N. Zhang, S. Yang, and D. Wang (2010). "Kinematics Simulation and Analysis of 3-RPS parallel robot on SimMechanics". In: *Information and Automation (ICIA), 2010 IEEE International Conference on*. IEEE, pp. 2363–2367.

Zhao, Q. and F. Gao (2010). "Design and analysis of a kind of biomimetic continuum robot". In: *Robotics and Biomimetics (ROBIO), 2010 IEEE International Conference on*. Ed. by IEEE, pp. 1316–1320.

Zhong, J., J. Fan, J. Zhao, and W. Zhang (2012). "Kinematic analysis of jumping leg driven by artificial muscles". In: *Mechatronics and Automation (ICMA), 2012 International Conference on*. IEEE, pp. 1004–1008.

Zhuang, H. (1997). "Self-calibration of parallel mechanisms with a case study on Stewart platforms". In: *IEEE Transactions on Robotics and Automation* 13.3, pp. 387–397. DOI: 10.1109/70.585901.

Zhuang, H. and Z. S. Roth (1995). *Camera Aided Robot Calibration*. CRC Press, Inc.

© 2014 Tous droits réservés.

doc.univ-lille1.fr

Thèse de Coralie Escande, Lille 1, 2013

Appendix A

Mobile Bionic Manipulator Robots

This appendix presents a technical literature review of mobile bionic manipulator robots. Since 1993, the bionic engineering started growing (Neumann et al. 1993), by finding the best correlation between biological and mechanical motions. During this last decade, modern mobile-manipulator platforms have been developed in different robotics fields (Figure A.1).

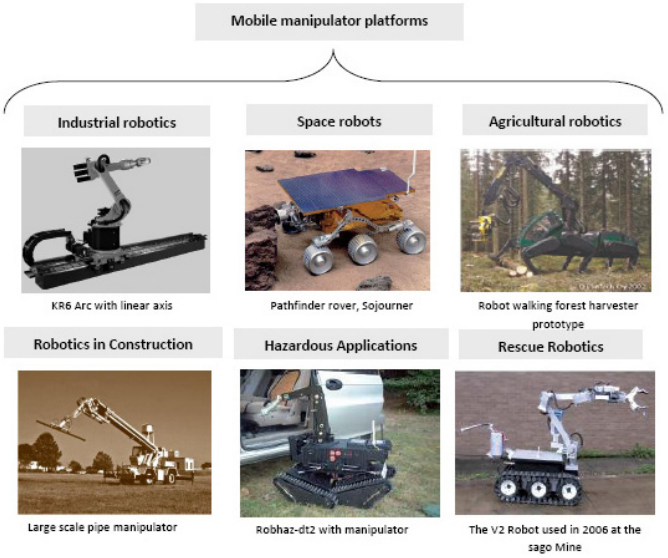

Figure A.1: Mobile-manipulator platforms in robotics fields

Almost all of them are biologically inspired, where their main aim is to reproduce with the best accuracy the inspired motion, according to the considered missions (Siciliano et al. 2009). We can notice that these developments are reserved for experienced users, who need a substantial background in technology

© 2014 Tous droits réservés.

doc.univ-lille1.fr

Thèse de Coralie Escande, Lille 1, 2013

and in some cases, in theory. The weight of the existing platforms is in general important and depends on the robot application (e.g. construction, agriculture and industry). The accuracy is also important in major existing applications, according to the importance of the tasks (e.g. robots for space, surgery systems and hazardous applications). The safety of human-robot interaction is also a substantial aspect because some of them are prototypes, which might find their way into the market, should they (prototypes) be developed into successful innovations. Also, the global costs of these systems are high, because they are considered as prototypes and not market products, thus not mass produced. In general, the structure of these systems and their various servo drives are the most expensive parts in the implementation phase. Moreover, for ecological reasons, reducing the whole costs, the energy consumption of mobile manipulator robots is also an open innovation challenge.

Thus, to do a synthesis on the progress beyond the design of mobile-manipulator platforms, table A.1 makes important comparisons.

Table A.1: Progress comparison

Existing mobile manipulator platforms	**Actual progress in designing mobile manipulator platforms**
Lightweight robot structures with high performance servo drives and carbon fibre structures	Lightweight robot structures by bionic design, bone like structures and compliant grippers, made by rapid manufacturing
Dangerous human-robot interactions	Safer human-robot interactions
Expensive high performance servo drives	Low cost polymer harmonic drive gear boxes, DC-motors, potentiometer feedback
Different programming systems for mobile robots and robot arms	One system for combined mobile manipulators
Programming system for expert users	Programming system for inexperienced users
High costs	Low costs
High energy consumption	Low energy consumption

For mobile bionic manipulator robots, the flexibility of the bionic arm eliminates some singularities, present in the case of rigid manipulator robots and yields to reach better the workspace targets.

© 2014 Tous droits réservés.

doc.univ-lille1.fr

Thèse de Coralie Escande, Lille 1, 2013

A.1 Mobility of the Bionic Mobile Manipulator Robots

It is the mobility of the basis platform of the bionic mobile manipulator robots which defines the planar workspace. The traction and orientation systems of the wheels for such robots allow the target's reachability inside the workspace. The mobility is associated with the possible motions which combine the passive and active steering and traction systems of the mobile platform. The mobility can be defined not only by the DoF [28] but also by the degrees of mobility, steerability and maneuverability (Siegwart et al. 2004). All of these properties depend on the characteristics of the mechanical structure in terms of holonomy, omnidirectionality and redundancy (Batlle et al. 2009).

A.1.1 Degree of Mobility

The degree of mobility is not directly dependent on the number of wheels but on their classes (conventional or omnidirectional, steerable or not) and their placement on the basis platform. There exists a classification of the different types of wheels (Siciliano et al. 2009):

Fixed Standard Wheel: Such wheel is also sometimes named conventional or non-steerable wheels. Its orientation angle is not varying and so, it has no steering rotation axis;

Steered Standard Wheel: Such wheel is steerable, that means that its orientation angle is varying and its steering rotation axis is defined by two points: the center of the wheel and the ground contact. The steering of such robot is driven by a dedicated motor;

Castor Wheel: Such wheel is also steerable, but its steering rotation axis does not pass through the ground contact point. Moreover, the steering of such robot is not driven by any motor, its motion is totally free;

Swedish Wheel: Such wheel is composed of one fixed standard wheel and a series of small rollers attached to its circumference. The axis of the small rollers are not parallel to those of the fixed standard wheel and their orientation

[28] Degree of Freedom (DoF) is associated to different aspects : in the robot design field, it is defined as the joint number, e.g. a rigid-link manipulator with 7 or 8 joints is said to be 7 or 8 DoF robot. In mechanics, the Degree of Freedom is defined as a possible motions according to a frame, where the maximum number of DoF is then equal to 6 describing 3 rotations and 3 translations.

© 2014 Tous droits réservés.

doc.univ-lille1.fr

Thèse de Coralie Escande, Lille 1, 2013

angles are typically about 45 *degrees* or 90 *degrees*. Thus, such wheel has no steering rotation axis but it has the ability to move omnidirectionally;

Spherical Wheel: Such wheels are in the form of a ball and they are omnidirectional. So they don't have any steering rotation axis.

Thus, the degree of mobility is defined as the number of directions that the robot can directly execute in changing the velocity of the wheels without driving their steering, or in other words, it is the number of DoF [29] that can be controlled without maneuvering. With this definition, the degree of mobility is equal to the Differential Degree of Freedom (DDoF), which is an integer between 0 and 3 for terrestrial robots. There are two approaches to calculate the degree of mobility: geometrical or mathematical (Siegwart et al. 2004).

In the *geometrical approach*, the degree of mobility is calculated in terms of independent kinematic constraints imposed to the robot's motion by each wheel of the robot and in terms of each wheel placement. The kinematic constraints are basically defined as the limiting mobility of the wheels which can not have a sliding motion. Thus, the kinematic constraints arising from all of the wheels have to be appropriately combined with the placement of these wheels, in order to have a possible motion.

By definition, the castor wheels as well as the swedish wheels and the spherical wheels can have a sliding motion, so that such wheels are not imposing any kinematic constraints. For the case of the fixed standard wheel, there is a "zero motion line" because of the kinematic constraint of non-sliding motion. This "zero motion line" is perpendicular to the direction of the wheel and constitutes the rotation axis of the wheel, where the rotational velocity is null. Finally, the case of the steered standard wheels, it is similar to the case of the fixed standard wheels, except the fact that the orientation of the "zero motion line" is varying in the same way as the steering orientation is driven.

The intersection of all "zero motion line" is called the Instantaneous Center of Rotation (ICR) [30], which depends on the number of kinematic constraints on the robot's motion. So the degree of mobility δ_{m} is defined as in equation (A.1), where $N_{\mathrm{independent}}$ is the number of independent kinematic constraints on the robot's motion.

[29] For terrestrial robots, the maximum value of DoF is equal to 3: 2 translations and 1 rotation; with the assumption that the ground is a plane without any relief.

[30] ICR is defined in mechanics for a rigid body as the center point of a global rotation of the robot at a particular instant of the trajectory. Thus, for a translation motion, the ICR is defined at the infinite, while for a rotation motion, it is the point where the velocity is null and all other points of the rigid body are rotating around this ICR. It has to be noticed that the ICR is not necessarily a point belonging to the rigid body. It is noticed that the ICR doesn't depend on the number of wheels.

© 2014 Tous droits réservés.

doc.univ-lille1.fr

Thèse de Coralie Escande, Lille 1, 2013

$$\delta_{\mathrm{m}} = 3 - N_{\mathrm{independent}} \tag{A.1}$$

In the *mathematical approach*, the degree of mobility is also defined using the kinematic constraint equations which impose the enabled movement. These constraints can be divided into two parts: one equation for the fixed standard wheels and another for the steered standard wheels. As in the geometrical approach, the number of independent kinematic constraints has to be determined, by calculating the rank [31] of the matrix of the kinematic constraint equations. The rank is always between 0 and 3. The degree of mobility δ_{m} is thus calculated using equation (A.2), where N_{rank} is the rank of the matrix of constraint equations.

$$\delta_{\mathrm{m}} = 3 - N_{\mathrm{rank}} \tag{A.2}$$

Finally the following cases can be distinguished:

- $\delta_{\mathrm{m}} = 0$ implies that the robot is completely constrained: no motion is possible.
- $\delta_{\mathrm{m}} = 3$ implies that there is neither fixed standard wheels nor steerable standard wheels.

A.1.2 Degree of Steerability

To determine *the degree of steerability*, only the kinematic constraint induced by the steered standard wheels are considered, because changing the steering orientation has an impact on the robot pose. Thus, the degree of steerability represents the number of independent kinematic constraints provided by steered standard wheels and it is an integer δ_{s} between 0 and 2 (Siegwart et al. 2004). The following cases can be distinguished:

- $\delta_{\mathrm{s}} = 0$ implies that there is no steered standard wheels.
- $\delta_{\mathrm{s}} = 1$ implies that there is one or more steered standard wheels.
- $\delta_{\mathrm{s}} = 2$ implies that there is no fixed standard wheels.

In fact, a standard steerable wheel decreases the degree of mobility because it adds a constraint equation, but this wheel increases the degree of steerability because the orientation of the wheel can be changed, offering new possible trajectories.

[31] Rank of independent rows or columns of the matrix of constraint equations

© 2014 Tous droits réservés.

doc.univ-lille1.fr

Thèse de Coralie Escande, Lille 1, 2013

A.1.3 Degree of Maneuverability

The global maneuverability of a mobile robot depends on the kinematic constraints due to the different types and placements of wheels, and on the additional DoF provided by the steering of the steered standard wheels or by the castor, swedish, or spherical wheels. Thus, the *degree of manoeuvrability* δ_M depends on the degree of mobility δ_m [32] and on the degree of steerability δ_s [33] as calculated in equation (A.3), where $0 \leq DDoF = \delta_m \leq \delta_M \leq DoF \leq 3$ (Siegwart et al. 2004). The following cases can be distinguished:

- $\delta_M = 2$ implies that the ICR takes place on the "zero motion line" of the robot;
- $\delta_M = 3$ implies that the ICR takes place on any point of the ground plane by appropriately changing the wheel velocities or by driving the wheels steering.

$$\delta_M = \delta_m + \delta_s \tag{A.3}$$

A.1.4 Holonomy and Omnidirectionality

The holonomy is a property, considered when the robot's mobility is studied, because it correlates with the maneuverability. The motion of non-holonomic vehicles is quite restricted, particularly inside small spaces, due to the limited degree of maneuverability. The DDoF and the DoF are used to determine the robot holonomy: a robot is holonomic if and only if $DDoF = DoF$ (Siegwart et al. 2004). A holonomic robot doesn't have any non-holonomic kinematic constraint and has only holonomic kinematic constraints [34].

Robots having neither fixed standard wheels nor steered standard wheels are always holonomic because they don't have any kinematic constraints and $\delta_M = 3$. An example of this case is an office chair having only castor wheels.

An omnidirectional robot is a holonomic robot which can drive in any direction, with $DDoF = DoF = 3$. This means that it can go directly at any target pose from any initial pose[35] without singularity in the plane. For example, it can execute a sideways movement (or "crab motion") without maneuvering. Robots with omnidirectional wheel's examples: *Robotino* (Festo 2013h) or the spherical wheels like the robot ballbot (T. B. Lauwers et al. 2006; T. Lauwers et al. 2005),

[32] $0 \leq \delta_m \leq 3$

[33] $0 \leq \delta_s \leq 2$

[34] A holonomic kinematic constraint is a relationship only in terms of positions and orientations, and not in terms of linear and angular velocities (Siegwart et al. 2004)

[35] pose = position + orientation

© 2014 Tous droits réservés.

doc.univ-lille1.fr

Thèse de Coralie Escande, Lille 1, 2013

represent omnidirectional and holonomic robots. However, a holonomic robot is not necessarily an omnidirectional robot and has not necessarily omnidirectional wheels; it can have only combined standard wheels. It is the case for the 2-wheels robot Khepera (K-Team 2002) or for a tracked tank robot (J. L. Martinez et al. 2005)). Moreover, an omnidirectional robot has not necessarily omnidirectional wheels and is not necessarily holonomic, for example: the *Robutainer* (Khalil, Merzouki, et al. 2012).

In conclusion, the omnidirectionality is defined by the DoF[36], while the holonomy is defined by the DoF[36] and the DDoF[37].

Several examples of robots are compared in Table A.2 according to their mobility, steerability and maneuverability.

For the cases of the robot *Robotino* and *Kuka-Youbot*, the swedish wheels imply that these robots are omnidirectional and holonomic.

For the robot *Khepera*^{2}, there is a unique "zero motion line" on which the ICR can be placed. This "zero motion line" is defined by the independent kinematic constraint of one of the two fixed standard wheels. The "zero motion line" of the second wheel is the same as those of the first wheel, so that the second wheel does not provide additional information on the robot kinematics: this robot has only one independent kinematic constraint.

In the case of the vehicle *Robutainer*, only two steered standard wheels can define the ICR because each steered standard wheel constrains the ICR to lie on its wheel axis. The two other steered standard wheels are then dependent on the two first steered standard wheels. Thus, there are two independent kinematic constraints. Moreover, when the steering is frozen, only one DoF can be manipulated. However, the wheels can be steered so that the robot can move laterally or diagonally and rotate around itself.

The robot *Robucar* seems similar to the vehicle *Robutainer* because it has also 4 steered standard wheels. But nevertheless, the way they are moving is different for two reasons: firstly the steering is limited[38], and secondly the steering of the rear wheels is locked as well as those of the front wheels.

[36]The DoF is the number of directions that the robot can drive by changing wheel velocities or by steering the wheels

[37]The DDoF is the number of directions that the robot can drive by changing wheel velocities, but without any maneuvers or wheel steering

[38]The wheels can not be steered with an angle superior to 45°.

© 2014 Tous droits réservés.

doc.univ-lille1.fr

Thèse de Coralie Escande, Lille 1, 2013

Table A.2: Comparison of several terrestrial mobile robots

Robot	**Type**	**Image**	Degrees **DoF**	**DDoF/δ_m**	δ_s	δ_M	**Properties**
Khepera[2] (K-Team 2002)	2 independent fixed standard wheels	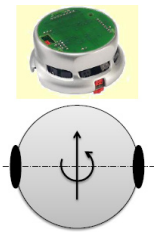	2	2	0	2	holonomic
Robotino (Weber et al. 2010)	3 independant swedish wheels (90°)	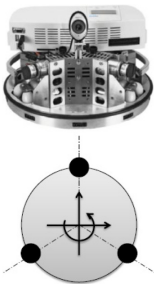	3	3	0	3	omni-directional and holonomic
Robucar (Merzouki, Samantaray, et al. 2013)	4 steerable wheels [39]	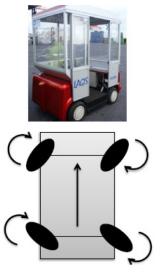	1	1	2	3	holonomic
Robutainer (Khalil, Merzouki, et al. 2012)	4 independent steerable wheels	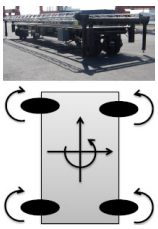	3	1	2	3	omni directional

Continued on next page

[39]The rear wheels have a common steering axle and the front wheels have also a common steering axle

© 2014 Tous droits réservés.

doc.univ-lille1.fr

Thèse de Coralie Escande, Lille 1, 2013

Table A.2 – continued from previous page

Robot	Type	Image	Degrees DoF	DDoF/δ_m	δ_s	δ_M	Properties
Kuka-Youbot (Kuka 2013)	4 independent swedish wheels (45°)		3	3	0	3	omni-directional and holonomic

Finally, terrestrial robots represent a class of road-mobile robots, and can be classified as shown in Table A.3. In this Table[40], a list of most known mobile-manipulator robots is presented, where they are compared to their locomotion and mobility.

[40]The MABEL robot is a fast running biped robot and VPTMR is the acronym for Variable Parallelogram Tracked Mobile Robot.

© 2014 Tous droits réservés.

doc.univ-lille1.fr

Thèse de Coralie Escande, Lille 1, 2013

Table A.3: Classification of the terrestrial mobile robots

Terrestrial mobile robots						
Terrain Based Classification	Continuum Robots	Legged Robots			Wheeled Robots	
Functionality	Snake-Like Undulation	Walking	Running	Jumping	Rolling	Tracking
Type of Robots	Snake	Humanoid	Biped		Mobile	Tracked
Examples of Robots	S5 Snake Prototype	NAO robot	MABEL robot	Jumping biped leg robot	Robotino	VPTMR robot
	(Miller 1999)	(Aldebaran 2013)	(Sreenath et al. 2013)	(Miller 1999)	(Weber et al. 2010)	(Ye et al. 2012)

Thèse de Coralie Escande, Lille 1, 2013

A.2 Conclusion of the Appendix

In this appendix, different types of mobile platforms, used for the design of mobile-manipulator robots, have been highlighted. These platforms can be distinguished according to their properties of mobility, steerability, maneuverability, omnidirectionality and holonomy.

© 2014 Tous droits réservés.

doc.univ-lille1.fr

Thèse de Coralie Escande, Lille 1, 2013

© 2014 Tous droits réservés.

doc.univ-lille1.fr

© 2014 Tous droits réservés.

doc.univ-lille1.fr

Thèse de Coralie Escande, Lille 1, 2013

Towards Modeling of a Class of Bionic Manipulator Robots

Abstract

This work deals with a particular class of bionic manipulator robot namely Compact Bionic Handling Assistant (CBHA), which is mounted over a mobile omnidirectional robot namely *Robotino*. The whole robot (CBHA + *Robotino*) is named RobotinoXT. We first proposed a forward kinematic model of the CBHA by using an "arc geometry" method which was validated through a test bench using a trilateration technique. To achieve this purpose, the sensors were calibrated. For the model's constant parameters calibration problem, this latter was resolved by developing an optimization algorithm which incorporates a SQP method, validated via an industrial rigid manipulator. Then, we proposed an inverse kinematic model of the CBHA by assuming that each vertebra of it is assimilated to a parallel robot. This model was validated by real measurements obtained with the industrial manipulator, allowing defining the robot workspace. Finally, we implemented a toolbox which encompasses the models developed in this work.

Keywords: Bionic Robotics, Kinematic Modeling, Kinematic Calibration

Vers la modélisation d'une classe de robots manipulateurs bioniques

Résumé

Ce travail concerne une catégorie de robot manipulateur bionique, en l'occurrence le CBHA monté sur un robot mobile omnidirectionel, nommé *Robotino*. Le robot complet (CBHA + *Robotino*) est nommé RobotinoXT. D'abord, nous avons proposé un modèle cinématique direct du CBHA en utilisant une méthode nommée « arc geometry ». Celle-ci a été validée grâce à un banc d'expérimentation en ayant recours à une technique de trilatération. Pour atteindre cet objectif, les capteurs ont été calibrés. Concernant le problème de calibration des paramètres constants du modèle, il a été résolu en développant un algorithme d'optimisation incluant une méthode nommée SQP, validée via un manipulateur industriel rigide. Puis, nous avons proposé un modèle cinématique inverse du CBHA en supposant que chaque vertèbre de celui-ci est assimilée à un robot parallèle. Ce modèle a été validé par les mesures réelles obtenues avec le manipulateur industriel, permettant la définition de l'espace de travail du robot. Enfin, nous avons implémenté une boîte à outils qui englobe les modèles développés dans ce travail.

Mots clés : Robotique Bionique, Modélisation Cinématique, Calibration Cinématique

Laboratoire d'Automatique, Génie Informatique et Signal
UMR CNRS 8219 – Université Lille 1 - Cité Scientifique – Bât Polytech'Lille – 59655 Villeneuve d'Ascq – France

© 2014 Tous droits réservés.

doc.univ-lille1.fr